WISC

UNIVERSITY OF WISCONSIN • MADISON, WISCONSIN

PLASMA PHYSICS

FLUCTUATION REDUCTION AND ENHANCED CONFINEMENT IN THE MST REVERSED-FIELD PINCH

B.E. Chapman

DOE/ER/54345-296

October 1997

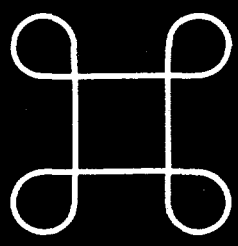

ONSIN

NOTICE

Printed in the United States of America
Available from
National Technical Information Service
U.S. Department of Commerce
5285 Port Royal Road
Springfield, VA 22161

NTIS Price codes
Printed copy: A09
Microfiche copy: A01

FLUCTUATION REDUCTION AND ENHANCED CONFINEMENT IN THE MST REVERSED-FIELD PINCH

by

Brett Edward Chapman

A dissertation submitted in partial fulfillment
of the requirements for the degree of

Doctor of Philosophy
(Physics)

at the

UNIVERSITY OF WISCONSIN-MADISON

1997

FLUCTUATION REDUCTION AND ENHANCED CONFINEMENT IN THE MST REVERSED-FIELD PINCH

Brett Edward Chapman
Under the supervision of Professor Stewart C. Prager
At the University of Wisconsin–Madison

Plasmas with a factor of ≥ 3 improvement in energy confinement have been achieved in the MST reversed-field pinch (RFP). These plasmas occur spontaneously, following sawtooth crashes, subject to constraints on, e.g., toroidal magnetic field reversal and wall conditioning. Possible contributors to the improved confinement include a reduction of core-resonant, global magnetic fluctuations and a reduction of electrostatic fluctuations over the entire plasma edge.

One feature of these plasmas is a region of strong $\mathbf{E} \times \mathbf{B}$ flow shear in the edge. Never before observed in conjunction with enhanced confinement in the RFP, such shear is common in enhanced confinement discharges in tokamaks and stellarators. Another feature of these plasmas is a new type of discrete dynamo event. Like sawtooth crashes, a common form of discrete dynamo, these events correspond to bursts of edge parallel current. However, these events originate in edge-resonant modes, while sawtooth crashes originate in core-resonant modes.

The reduction of electrostatic fluctuations in these plasmas occurs within and beyond the region of strong $\mathbf{E} \times \mathbf{B}$ flow shear, similar to what is observed in tokamaks and stellarators. However, the reductions in the MST include fluctuations whose correlation lengths are larger than the width of the shear region. The reduction of the global magnetic fluctuations is most likely due to flattening of the $\mu = \mu_o \mathbf{J}\cdot\mathbf{B}/B^2$ profile. Flattening can occur, e.g., due to the new type of discrete dynamo event and reduced edge resistivity.

Enhanced confinement plasmas are also achieved in the MST when auxiliary current is applied to flatten the μ profile and reduce magnetic fluctuations. Unexpectedly, these plasmas also exhibit a region (broader than in the case above) of strong $\mathbf{E} \times \mathbf{B}$ flow shear in the edge, an edge-wide reduction of electrostatic fluctuations, and the new type of discrete dynamo event. Auxiliary current drive has historically been viewed as the principal route to fusion reactor viability for the RFP. However, if $\mathbf{E} \times \mathbf{B}$ flow shear plays a role in improved RFP confinement, then the RFP might also benefit from auxiliary heating, which is used to trigger such shear in other devices.

DISCLAIMER

Acknowledgments

First, I'd like to thank my most recent advisor, Stewart Prager, for allowing me (1) to switch thesis topics and (2) the freedom to pursue my own ideas. I also greatly appreciate his regular availability for discussion, particularly given his often hectic schedule. I'd also like to thank Ray Fonck and Daniel Den Hartog for co-advising me during much of the time I spent on my first thesis topic. I want to thank my thesis defense committee members, Cary Forest and Clint Sprott, and in particular, Jim Callen and Paul Terry, for agreeing to carefully review my dissertation.

This thesis would not have been possible without the diagnostic support and experimental/theoretical insight of a number of faculty, scientists, and postdocs. These include Paul Terry, Abdulgader Almagri, Gennady Fiksel, John Sarff, Don Holly, Miodrag Cekić, Hantao Ji, and Matt Stoneking. There were also countless contributions, not the least of which was operation of the MST, from my fellow experimentalist grad students: Jay Anderson, Ted Biewer, (cousin) Jim Chapman, Ching-Shih Chiang, Darren Craig, Neal Crocker, Paul Fontana, Alex Hansen, Jon Henry, (big) Nick Lanier, Kevin Mirus, and Dimitry Sinitsyn. I would like to further acknowledge Ching-Shih Chiang for his continuous and sometimes beyond-the-call-of-duty assistance in gathering the probe data for this thesis.

I want to thank Carl Sovinec and Eduardo Fernandez for many helpful discussions of MHD and turbulence theory. I'd also like to acknowledge other grad students, past and present, with whom I've

shared an office. The original Inertial Rangers include Jim Hollenberg, David Newman, Gene Riggs, Earl Scime, Matt Stoneking, and Chris Watts. Those carrying on the Ranger tradition in fine style include some of the students listed above, as well as Derek Baver and Chuang Ren.

This thesis was also made possible through the efforts of the MST technical staff. I want to acknowledge John Laufenberg for his untiring assault on the (sometimes explosive) gremlins that plague the MST. I want to thank Roch Kendrick for his many creative designs. I also want to thank Tom Lovell and Mark Thomas for technical advice of all sorts. Larry Smith and Paul Wilhite deserve special recognition for holding together the MST's antiquated computer system. Of course, I also want to acknowledge Kay Shatrawka for her work, friendliness, and wit.

Thanks to my parents, Larry and Betty, for being there for me through more years of school than I care to remember. Thanks to the Dude, for keeping me company those long nights spent writing my thesis. Most of all, I want to thank my wife, Jen, for continuously believing in me. Meeting and marrying her was, by far, my most important accomplishment as a grad student.

I was supported for three years by the Magnetic Fusion Science Fellowship Program, administered by the Oak Ridge Institute for Science and Education for the U.S.D.O.E. (living above the poverty line was nice while it lasted). My remaining years of work were also supported by the U.S.D.O.E.

Table of contents

1. Introduction

The reversed field pinch (RFP) is a magnetically confined toroidal plasma configuration characterized by a relatively weak toroidal magnetic field whose direction in the plasma edge is opposite that in the core [1,2]. There is also a poloidal magnetic field whose strength is comparable to that of the toroidal field. In the Madison Symmetric Torus (MST) [3] RFP, fluctuations in the magnetic field have been measured to drive particle [4] and energy [5] transport in the plasma core. Fluctuations in the electric field, induced by charge buildup in the plasma, have been measured to drive particle transport in the plasma edge [6], but the mechanism underlying energy transport in the edge has not been established. In general, magnetic fluctuations are believed to play a larger role than electrostatic fluctuations in determining RFP global transport.

1.0 Fluctuation reduction and enhanced confinement

The primary goal of the MST RFP program is the reduction of fluctuation driven transport. The dominant magnetic fluctuations in the RFP are core-resonant, global tearing modes [7], driven by gradients in the $\mu = \mu_o \mathbf{J}\cdot\mathbf{B}/B^2$ profile, where $\mathbf{J}$ is the current density, and $\mathbf{B}$ is the magnetic field. Neither the identity nor the source of the electrostatic fluctuations has been firmly established, but these fluctuations may be driven, e.g., by edge gradients in the pressure and/or resistivity profiles [2,7,8]. Because magnetic fluctuations are believed to dominate anomalous transport in the RFP, and because their origin is better

understood than that of electrostatic fluctuations, their reduction has been a major focus of experimental and theoretical work.

A gradient develops in the μ profile because it evolves to a centrally peaked state. This occurs due to resistive diffusion and the peaked parallel equilibrium inductive electric field. Due in part to the presence of a material boundary (the plasma-facing wall), the plasma resistivity is largest in the edge, while it is relatively low on axis. Thus, plasma current tends to diffuse inward. Since the toroidal magnetic field in the edge is reversed relative to its direction in the core, the (toroidal) inductive electric field, which drives the toroidal plasma current, drives parallel ($\mu > 0$) current in the core and antiparallel current ($\mu < 0$) in the edge. This further contributes to the gradient in $\mu(r)$.

The gradient in $\mu(r)$ is periodically removed by a sawtooth crash, which comprises part of the sawtooth oscillation [9,10,11]. Sawtooth oscillations occur throughout most MST discharges. At the crash, current parallel to $\mathbf{B}$ is rapidly redistributed, and $\mu(r)$ is flattened. Between crashes is the sawtooth rise phase, during which (over several milliseconds) $\mu(r)$ evolves to a peaked state. The sawtooth crash is referred to as a discrete dynamo event, because its redistribution of current produces (toroidal) magnetic flux.

The amplitudes of the dominant magnetic fluctuations are governed by the sawtooth cycle and evolution of $\mu(r)$. These fluctuations are relatively small just following a sawtooth crash, but they slowly increase, on average, as $\mu(r)$ becomes centrally peaked. At the sawtooth crash, all of the dominant mode amplitudes, including

those modes with m = 1 and m = 0, increase dramatically. These magnetic fluctuations, coupled with velocity fluctuations, comprise a parallel electric field that is believed to account for the redistribution of parallel current. Fluctuation-driven current is also present at a lower level between crashes [12,13].

Magnetohydrodynamic modeling by Ho [12] and Sovinec [14] has suggested that auxiliary parallel current driven in the plasma edge can achieve a flattened μ profile (reduce $\nabla\mu$) and reduce the dominant magnetic fluctuations. It has also been suggested that the necessary current could be driven inductively [12]. Sarff *et al.* [15,16] applied a poloidal (~ parallel) inductive electric field, and this resulted in a significant reduction of magnetic fluctuations, an improvement in particle confinement time, and a factor of 4 – 5 improvement in energy confinement time.

More recently, reduction of magnetic fluctuations was also achieved by Chapman *et al.* [17] in discharges which do not utilize auxiliary current drive but are characterized by periods of improved particle confinement and a factor of ≥ 3 improvement in energy confinement time (study of these discharges comprises the bulk of this thesis). Further, the magnetic fluctuation reduction in these discharges occurs with a phenomonology similar to that in discharges with auxiliary current drive. This and other similarities between these two types of discharge suggest that while auxiliary current drive may work as predicted by the modeling, it is apparently not acting alone. Thus, one is encouraged to search for features common to both discharges that could contribute to the reduction of magnetic fluctuations.

One striking feature common to both types of enhanced confinement discharge is a large radial electric field (E_r) gradient, leading to sheared $\mathbf{E} \times \mathbf{B}$ rotation, in the plasma edge [17]. Such a gradient in E_r has never before been observed in conjunction with enhanced confinement in the RFP but is similar in some respects to that which characterizes one variety of enhanced confinement discharge in tokamaks and other devices [18,19]. In these devices, a ~ 1 cm wide region of $\mathbf{E} \times \mathbf{B}$ flow shear in the plasma edge corresponds to a local reduction of electrostatic fluctuations and transport, qualitatively consistent with theoretical predictions [20]. Fluctuations are also reduced beyond this region in the plasma edge. Such flow shear has also led to substantial improvements in core confinement in some devices [21,22]. Thus, $\mathbf{E} \times \mathbf{B}$ flow shear is emerging as a virtually universal means of fluctuation reduction and confinement improvement.

Similar to other devices with $\mathbf{E} \times \mathbf{B}$ flow shear in the edge, the two types of enhanced confinement discharge in the MST exhibit a reduction of electrostatic fluctuations in the shear region and over the entire plasma edge. These reductions are broadband, including both low and high frequency fluctuations. Reduction of short wavelength (high frequency) fluctuations lying entirely within the shear region can reasonably be expected, based on the $\mathbf{E} \times \mathbf{B}$ flow shear paradigm [20]. Flow shear reduction of the longer wavelength (lower frequency) fluctuations overlapping the shear region is also possible, but such an interaction has not yet been dealt with analytically. The $\mathbf{E} \times \mathbf{B}$ flow shear is unable to directly affect those fluctuations lying entirely

outside the shear region, and other mechanisms, such as a stabilizing change in the edge profiles, must be invoked to account for these reductions.

It is also possible that the edge-localized $\mathbf{E} \times \mathbf{B}$ flow shear affects the (global) magnetic fluctuations in the MST, but there are other explanations suited to both types of enhanced confinement discharge. One possibility lies in the fact that these discharges exhibit a type of discrete dynamo event distinct from sawtooth crashes [11,17]. Like crashes, this new type of dynamo event corresponds to a burst of edge parallel current, which can help to reduce $\nabla\mu$ and the dominant magnetic fluctuations. However, while crashes originate in the core-resonant modes, these new dynamo events originate in modes resonant in the plasma edge. In addition to these events, reduction of edge resistivity, which affects the shape of the μ profile and can affect the magnetic fluctuations, is also common to both types of enhanced confinement discharge.

There is as yet no data to quantify the relative contribution to improved confinement made by each fluctuation reduction (electrostatic and magnetic) in the MST. Normally, the reduction of magnetic fluctuations would be considered to be the dominant contributor, but electrostatic fluctuations could be important as well, implying the significance of the $\mathbf{E} \times \mathbf{B}$ flow shear.

Given the possible significance of the sheared $\mathbf{E} \times \mathbf{B}$ flow, we can reasonably draw on the vast experience with similar discharges in other devices in order to try to understand the physics occurring in the MST. For example, it is well known that local $\mathbf{E} \times \mathbf{B}$ flow shear in tokamaks

and stellarators can be reliably triggered by heat flux through the plasma edge, where the shear develops [23]. It can be triggered spontaneously by the heat flux associated with sawtooth crashes, and it can be triggered more controllably with neutral beam or radio frequency (RF) heating [18,24].

In the MST, periods of enhanced confinement without auxiliary current drive always follow sawtooth crashes, which increase the heat flux through the plasma edge [5]. Further, the auxiliary edge current associated with the other type of enhanced confinement discharge must provide some level of Ohmic heating. Thus, edge heating may be the means by which the sheared $\mathbf{E} \times \mathbf{B}$ flow is triggered in both types of discharge. Verification of this hypothesis awaits measurement of the electron and majority ion temperature in these discharges.

Until recently, the only viable route to magnetic fluctuation reduction and improved confinement in the RFP was thought to be through the implementation of auxiliary current drive, ultimately requiring noninductive techniques such as RF current drive. However, the possibility exists that improved confinement can be achieved with auxiliary heating, which could be significantly simpler to implement than RF current drive.

To summarize, discharges with improved confinement in the MST share several features in common, including (1) a region of $\mathbf{E} \times \mathbf{B}$ flow shear in the plasma edge, (2) reduction of electrostatic fluctuations within and beyond the shear region, (3) reduction of global magnetic fluctuations, and (4) changes to the current profile due, e.g., to a new type of discrete dynamo event and reduction of plasma resistivity. The

reduction of the electrostatic fluctuations in the shear region can be understood in terms of the $\mathbf{E} \times \mathbf{B}$ flow shear paradigm, while the reductions outside this region require other explanations. If the magnetic fluctuations, believed to be affected by gradients (and the absence thereof) in the parallel current profile, are also affected by the local $\mathbf{E} \times \mathbf{B}$ flow shear, this would represent an extension of the $\mathbf{E} \times \mathbf{B}$ flow shear paradigm. There is a finite probability that the flow shear in the MST can be triggered by auxiliary heating. If so, and if the shear does play a role in the improved confinement, then the prospects for the RFP as a viable fusion reactor concept will have improved substantially.

1.1 Outline

For convenience throughout this thesis, I will commonly use three acronyms: EC (enhanced confinement) refers to those discharges with improved confinement without auxiliary current drive; PPCD (pulsed poloidal current drive) refers to discharges in which the improved confinement is accompanied by auxiliary poloidal current drive; and SDE (small dynamo event) refers to the new variety of discrete dynamo observed in EC and PPCD discharges.

While I have studied both EC and PPCD discharges in the course of this work, EC discharges have been my primary focus. Thus, a large fraction of the data in the following chapters will be from EC discharges. However, since both types of discharge have many features in common, such as operational requirements, fluctuation reduction, and $\mathbf{E} \times \mathbf{B}$ flow shear, I will show and discuss relevant PPCD data in parallel with EC

data.

In Chapter 2, I review the physics of improved confinement discharges associated with $\mathbf{E} \times \mathbf{B}$ flow shear in other devices. This may help us to understand some aspects of EC and PPCD discharges. In part because such physics is not usually discussed in the context of the RFP, I spend more time on this topic than I do, e.g., on the physics of magnetic fluctuations and magnetic fluctuation induced transport, which dominates discussions of RFP physics. Chapter 3 contains a quantitative discussion of the improved confinement in EC discharges with comparisons to the confinement of standard and PPCD discharges. In this chapter, I also discuss in detail the operational requirements for EC and PPCD discharges. In Chapter 4, I present the EC and PPCD radial electric field profiles. In addition, I show data suggesting a reduction of edge transport in these discharges, and I discuss the role that heating may play in triggering the $\mathbf{E} \times \mathbf{B}$ flow shear. Small dynamo events are the subject of Chapter 5, and in addition to discussing their characteristics, I describe the impact of these events on MST confinement and their controllability. In Chapter 6, I discuss the causes and effects of electrostatic and magnetic fluctuations. I also discuss their reduction in EC and PPCD discharges, and the possible mechanisms underlying these reductions. In Chapter 7 is a brief thesis summary, suggestions for future work, and some concluding remarks.

1.2 Experimental apparatus

The MST is a relatively large Ohmically heated device whose features are discussed in detail in Ref. 3. Some of the basic design and

Table 1. MST parameters.

Major radius	150 cm
Minor radius	52 cm
Wall thickness	5 cm
Plasma current	> 600 kA
Loop voltage	≤ 10 V
Electron temperature	> 600 eV
Line-averaged density	$> 2 \times 10^{13}$ cm^{-3}
Energy confinement time	~ 5 ms
Poloidal beta	~ 9 %

operational parameters of the MST are given in Table 1. Graphite tiles cover roughly 10% of the aluminum plasma-facing wall (the inner surface of the vacuum vessel), which is otherwise bare. The vacuum vessel serves both as a conducting (stabilizing) shell and as the single-turn toroidal field winding. The lack of discrete toroidal field coils minimizes toroidal field ripple. Further, instead of relying on a few large portholes for vaccum pumping, the MST has ~ 200 smaller holes. This minimizes the (radial) field errors associated with portholes. Field errors remain a problem at the poloidal gap (insulated vertical cut in the conducting shell). However, various sets of passive and active field error correction coils have been installed at this gap [25], and they can maintain the field errors at a level where they do not seriously affect MST discharges.

Careful control of field errors, which minimizes plasma-wall interaction, is one ingredient necessary for the achievement of enhanced confinement discharges in the MST. Another necessity is careful conditioning of the plasma-facing wall. This is accomplished in part by an automated pulsed-discharge cleaning system. This system runs unattended overnight and at other times when the machine is not in use for RFP experiments. Control of field errors and wall conditioning are discussed further in Chapter 3.

Many of the diagnostics used in this work were designed and/or operated by others in the MST group, and I will give only brief descriptions of these diagnostics, including references in some cases. A Thomson scattering diagnostic [26] was used to measure the central electron temperature at a single point in time during each discharge. The central line-averaged electron density was measured with a single-chord interferometer, while an 11-chord interferometer was used to measure the full electron density profile. The temperature of the fuel ions was measured with a neutral particle charge-exchange energy analyzer [27]. A fast Doppler spectrometer [28] was employed to measure both impurity ion temperature and flow velocity.

A pair of soft x-ray filters was used to *qualitatively* monitor the time evolution of the central electron temperature [29]. One filter is 0.6 mils (0.0006 in.) thick, while the other is 0.3 mils thick. Because of their different thicknesses, these filters have different response functions for a given soft x-ray spectrum, and the ratio of the signal from the thicker filter to that from the thinner filter is proportional to the electron temperature. As the electron temperature increases, the

signal from the thicker filter increases relative to that in the thinner filter, thereby increasing the ratio. However, beyond roughly 450 eV, the filter signals change by the same increment with changes in temperature. Thus, the ratio becomes constant and no longer reflects changes in temperature.

As discussed in Ref. 29, impurity line radiation in the soft x-ray range of the spectrum can contaminate this ratio to the point of making it useless. However, the change in temperature indicated by the filters was compared to the temperature measured with the Thomson scattering diagnostic in a density scan in normal, but relatively clean (low impurity level) MST discharges. As the density decreased, the Thomson-scattering-measured temperature increased, as usual, and the filter ratio increased monotonically as well [30]. This, plus the fact that impurity levels in EC and PPCD discharges are even lower than in clean, standard discharges, lends confidence to the use of this ratio as a qualitative indicator of the electron temperature.

To measure the electron temperature and density in the extreme edge (in the shadow of the limiters) an "operational Langmuir probe" [31] was used. Amplitudes and phase velocities of the dominant magnetic modes were measured with a toroidal array of up to 64 magnetic sensing coils. Line radiation from fuel and impurity particles was monitored with a standard complement of filtered photodiodes, monochromators, and spectrometers. Descriptions of the probes used to measure, e.g., the radial electric field profiles, is given in Chapter 4.

References

[1] H. A. B. Bodin and A. A. Newton, Nucl. Fusion **20**, 1255 (1980).

[2] S. C. Prager, Plasma Phys. Controlled Fusion **32**, 903 (1990).

[3] R. N. Dexter *et al.*, Fusion Technol. **19**, 131 (1991).

[4] M. R. Stoneking *et al.*, Phys. Rev. Lett. **73**, 549 (1994).

[5] G. Fiksel *et al.*, Phys. Rev. Lett. **72**, 1028 (1994).

[6] T. D. Rempel *et al.*, Phys. Rev. Lett. **67**, 1438 (1991).

[7] H. P. Furth, J. Killeen, and M. N. Rosenbluth, Phys. Fluids **6**, 459 (1963).

[8] P. W. Terry *et al.*, in Proceedings of the 13th International Conference on Plasma Physics and Controlled Nuclear Fusion Research, Washington D. C., 1990 (IAEA, Vienna, 1991), Vol. 2, p. 169.

[9] J. A. Beckstead, Ph.D. thesis, University of Wisconsin, Madison, Wisconsin, 1990.

[10] S. Hokin *et al.*, Phys. Fl. B **3**, 2241 (1991).

[11] B. E. Chapman *et al.*, Phys. Plasmas **3**, 709 (1996).

[12] Y. L. Ho, Nucl. Fusion **31**, 314 (1991).

[13] H. Ji *et al.*, Phys. Rev. Lett. **73**, 668 (1994).

[14] C. R. Sovinec, Ph.D. thesis, University of Wisconsin, Madison, Wisconsin, 1995.

[15] J. S. Sarff *et al.*, Phys. Rev. Lett. **72**, 3670 (1994).

[16] J. S. Sarff *et al.*, Phys. Rev. Lett. **78**, 62 (1997).

[17] B. E. Chapman *et al.*, submitted to Phys. Rev. Lett.

[18] R. J. Groebner, Phys. Fl. B **5**, 2343 (1993).

[19] K. H. Burrell, Phys. Plasmas **4**, 1499 (1997).

[20] H. Biglari, P. H. Diamond, and P. W. Terry, Phys. Fl. B **2**, 1 (1990).

[21] F. M. Levinton *et al.*, Phys. Rev. Lett. **75**, 4417 (1995).

[22] E. J. Strait *et al.*, Phys. Rev. Lett. **75**, 4421 (1995).

[23] T. N. Carlstrom, Plasma Phys. Controlled Fusion **38**, 1149 (1996).

[24] F. Wagner *et al.*, Phys. Rev. Lett. **53**, 1453 (1984).

[25] A. F. Almagri *et al.*, Phys. Fl. B **4**, 4080 (1992).

[26] D. J. Den Hartog and M. Cekic, Meas. Sci. Technol. **5**, 1115 (1994).

[27] E. Scime and S. Hokin, Rev. Sci. Instrum. **63**, 4527 (1992).

[28] D. J. Den Hartog and R. J. Fonck, Rev. Sci. Instrum. **65**, 3238 (1994).

[29] G. A. Chartas, Ph.D. thesis, University of Wisconsin, Madison, Wisconsin, 1991.

[30] M. Cekic and M. R. Stoneking (private communication).

[31] H. Ji, PLP Report No. 1145, University of Wisconsin, Madison, Wisconsin, 1994.

2. Review of H-mode

The search for strong radial electric field gradients in EC and PPCD discharges was motivated by these discharges' rough similarity to H-mode (high mode) enhanced confinement discharges in tokamaks and other magnetic configurations. An examination of the physics underlying the H-mode phenomenon can potentially help us understand some aspects of EC and PPCD discharges. In Sec. 2.0, I describe some common characteristics of the H-mode, and in Sec. 2.1, I discuss the fundamental importance of $\mathbf{E} \times \mathbf{B}$ flow shear in the reduction of fluctuations. Section 2.2 provides an experimental and theoretical discussion of the transition to the H-mode state. Section 2.3 contains observations of fluctuation reduction in the plasma edge and core during H-mode discharges. Edge-localized modes, which play several important roles in the H-mode, are the subject of Sec. 2.4. In Sec. 2.5, I briefly describe some enhanced confinement discharges besides H-mode in which $\mathbf{E} \times \mathbf{B}$ flow shear plays a role. Sec. 2.6 describes how H-mode physics may apply to the RFP.

2.0 Common characteristics

The H-mode state was first discovered in auxiliary heated divertor discharges in the ASDEX tokamak [1]. The H-mode has now been achieved in all divertor tokamaks [2], and it has also been achieved in discharges without divertors, where only limiters define the plasma boundary [2,3]. In addition to auxiliary heated discharges, H-mode has also been observed in Ohmic discharges [2,4,5]. Significantly,

the H-mode has also been achieved in magnetic configurations besides the tokamak, including a current-free stellarator [6] and a heliotron/torsatron [7]. Thus, *the appearance of the H-mode does not depend on a particular magnetic geometry.*

The commonly observed characteristics of the H-mode are described in two experimental review papers [2,8]. Fundamental to all H-mode discharges is a strongly inhomogeneous, negative (pointing inward) radial electric field (E_r) in a narrow region in the plasma edge. For example, in the DIII-D tokamak, E_r can change by as much as 20 kV/m over a 1 cm radial extent [8]. Both the sign and the magnitude of E_r are determined by the local pressure gradient and plasma flow velocity, as discussed in the next section. Strong gradients in E_r leads to strongly sheared $\mathbf{E} \times \mathbf{B}$ plasma flow, which, in accordance with theoretical prediction [9], is observed to reduce local fluctuations and transport, thereby improving particle and energy confinement. Fluctuations are also reduced in the plasma core, but this does not contribute significantly to the improved confinement (see Sec. 2.3).

Some other generally observed traits include a reduction of neutral particle radiation (H_α or D_α) and a steepening of the density profile in the shear region, both implying reduced particle transport. The plasma stored energy also increases, resulting in an improved energy confinement time. Also important in H-mode discharges are so-called edge-localized modes (ELM's) [10]. These instabilities are both detrimental and beneficial.

Empirically, it is found that the H-mode (i.e. the strongly sheared $\mathbf{E} \times \mathbf{B}$ flow), is triggered by sufficient heat flux through the plasma edge

(where the strong shear forms) [11]. Thus, one reliable means of triggering an H-mode is the application of auxiliary heating. Another more passive method in tokamaks involves sawtooth crashes, which are instabilities that cause rapid transport of energy from the plasma core to the edge. In Ohmic discharges, sawteeth are often the means by which an H-mode is triggered [4], and sawteeth sometimes act as the trigger in auxiliary heated discharges as well [12].

The amount of heating power that must be supplied to the edge plasma in order to trigger an H-mode varies with various plasma parameters [11]. In the tokamak, for example, the necessary power increases with both magnetic field strength and plasma density [11,13]. This power threshold also exhibits a fuel ion isotope dependence, as the threshold with deuterium is lower than that for both hydrogen and helium [11]. The power threshold also depends on the condition of the plasma-facing wall. Careful conditioning of the wall can reduce the power threshold and improve H-mode confinement [2].

2.1 Sheared $\mathbf{E} \times \mathbf{B}$ flow and fluctuation reduction

Biglari *et al.* [9] were among the first to conclude that strong $\mathbf{E} \times \mathbf{B}$ flow shear can reduce turbulent fluctuations. In the strong shear limit, where the shearing rate is larger than the rate of turbulent radial scattering, the radial correlation length of the ambient turbulence is reduced. This reduces the fluctuation amplitude and the associated radial transport, *independent of the sign of E_r or its shear.* Biglari *et al.* [9] demonstrate this analytically, in cylindrical geometry, as follows.

In cylindrical geometry, $\mathbf{E} \times \mathbf{B}$ rotation is almost purely poloidal in

the tokamak. With shear in the $\mathbf{E} \times \mathbf{B}$ rotation, there are two rates governing the fissure or decorrelation of a turbulent eddy, the *poloidal* ($\mathbf{E} \times \mathbf{B}$) shearing rate, $\omega_s = (k_{oy}\Delta r_t)|v_\theta' - v_\theta/r_+|$, and the *radial* diffusive scattering rate, $\Delta\omega_t = 4D/\Delta r_t^2$. Here, k_{oy}^{-1} and Δr_t characterize the poloidal and radial correlation lengths of the ambient turbulence, v_θ is the poloidal ($\mathbf{E} \times \mathbf{B}$) velocity, r_+ is the center-of-mass coordinate (of two components of the turbulent eddy), and D is a diffusion coefficient. The frequency ω_s can be thought of as the rate at which two components of the eddy separated radially by Δr_t become separated poloidally by k_{oy}^{-1}. The decorrelation rate $\Delta\omega_t$ is that induced by the turbulent radial diffusion of fluctuations by the ambient turbulence (in the absence of $\mathbf{E} \times \mathbf{B}$ shear). The expression for ω_s illustrates that even if $v_\theta' = 0$, fluctuations can still be shorn apart due to the effects of curvature (v_θ/r_+). Of course, $v_\theta' \neq 0$ in H-mode discharges and is substantially larger than v_θ/r_+. Thus, ω_s is dominated by the $\mathbf{E} \times \mathbf{B}$ flow shear.

In the absence of $\mathbf{E} \times \mathbf{B}$ flow shear, the decorrelation of the turbulent eddy occurs on a timescale on the order of $\Delta\omega_t^{-1}$, but in the strong shear limit ($\omega_s > \Delta\omega_t$), the decorrelation occurs on a hybrid timescale, $\tau_c = (2\omega_s^2\Delta\omega_t)^{-1/3} < \Delta\omega_t^{-1}$. Two noteworthy aspects of this expression are (1) that rotational shear plays a larger role than radial scattering in the fluctuation decorrelation and (2) the sign of ω_s [$\sim v_\theta' = d(E_r/B)/dr$] is irrelevant. This hybrid timescale corresponds to a new characteristic radial correlation length, $\Delta r_c = \Delta r_t(\Delta\omega_t/\omega_s)^{1/3}$, which represents a reduction from the case without flow shear. The poloidal correlation length remains unchanged.

Biglari *et al.* then show that the reduced radial correlation length

results in a reduction of fluctuation amplitude. Assume that the fluctuations, represented by ξ, are driven by the free energy associated with the relaxation of some macroscopic gradient (e.g., pressure), the scale length of which is represented by L_ξ. The driven fluctuations also decay by turbulent decorrelation, characterized by $\tau_f \sim \tau_c$, where τ_f^{-1} is defined as the rate at which a fluid blob fissures or the rate at which the relative separation of two fluid elements within the blob becomes comparable to the blob dimensions. One can then heuristically write

$$(\partial/\partial t + \tau_f^{-1})\langle|\xi/\xi_o|^2\rangle \approx D/L_\xi^2,$$

where ξ_o is the mean value of the fluctuating quantity.

In the absence of poloidal shearing ($\omega_s = 0$), $\tau_f^{-1} \sim D/\Delta r_t^2$, and for stationary turbulence ($\partial/\partial t \rightarrow 0$), it follows that $\langle|\xi/\xi_o|^2\rangle \approx (\Delta r_t/L_\xi)^2$. On the other hand, in the strong shear limit, $\tau_f^{-1} \approx (\omega_s^2\Delta\omega_t)^{1/3}$, from which it follows that $\langle|\xi/\xi_o|^2\rangle \approx (\Delta r_c/L_\xi)^2$. Therefore,

$$\langle|\xi/\xi_o|^2\rangle_{\omega_s\neq 0}/\langle|\xi/\xi_o|^2\rangle_{\omega_s=0} \sim (\Delta r_c/\Delta r_t)^2 \sim (\Delta\omega_t/\omega_s)^{2/3} < 1.$$

In other words, in the strong shear limit, the normalized fluctuation amplitude is reduced from its ambient (shear-free) value, and fluctuation driven transport can be reduced. The above expression also shows that the degree to which the fluctuations are reduced can vary. For a given rate of ambient radial scattering, fluctuation reduction will be more pronounced the larger the poloidal shearing rate.

In a cylindrical model (which has no neoclassical effects), such as

that used by Biglari *et al.* [9], there is little difference between perpendicular (≈ poloidal, in the tokamak) fluid velocity and the $\mathbf{E} \times \mathbf{B}$ flow velocity, and no distinction between these velocities can be made regarding fluctuation reduction [14]. In toroidal geometry, however, the $\mathbf{E} \times \mathbf{B}$ velocity and the fluid velocity due to E_r can be quite different. Neoclassically (in toroidal geometry) the poloidal component of the $\mathbf{E} \times \mathbf{B}$ drift is strongly damped [15]. Thus, the neoclassical flow due to E_r can be purely toroidal [16,17], while the $\mathbf{E} \times \mathbf{B}$ velocity has a large poloidal component. Because of damping, the poloidal rotation of the plasma does not reflect the large poloidal component of the $\mathbf{E} \times \mathbf{B}$ drift.

There has been some confusion in the literature as to which sheared velocity is important to H-mode. Part of this confusion may have arisen because the first observations of a change in E_r during an H-mode were based on impurity poloidal rotation measurements [18,19]. It has now been made clear that the $\mathbf{E} \times \mathbf{B}$ flow velocity, not simply the poloidal or toroidal fluid velocity, is the quantity of fundamental importance to the reduction of fluctuations. Kim *et al.* [20] demonstrated the importance of $\mathbf{E} \times \mathbf{B}$ shear in a toroidal geometry derivation of the equations governing electrostatic flute-like modes, believed to be important in the tokamak edge. For example, they derived the following equation:

$$\nabla\bullet(n\mathbf{V}_E + n\mathbf{V}_d) = \ldots = \mathbf{V}_{1E}\bullet\nabla_\perp n_1 + \mathbf{V}_{1E}\bullet\nabla_\perp n_o + \mathbf{V}_{1E}\bullet\nabla_\perp n_1 - n_o\mathbf{V}_{1\perp}\bullet\nabla\ln(B^2) + O(\delta^3).$$

Here, $\mathbf{V}_E$ and $\mathbf{V}_d$ are the $\mathbf{E} \times \mathbf{B}$ and diamagnetic flow velocities, n is the

density, and terms in italics are fluctuating quantities. The other subscripts represent the ordering of various terms. In this equation, the diamagnetic flow contribution cancels out, and the first and third terms on the right hand side reveal that flute-like density fluctuations are convected only with the $\mathbf{E} \times \mathbf{B}$ flow velocity. Kim *et al.* derive a similar equation for energy fluctuations. Thus, although shear in the toroidal and/or poloidal fluid velocities may exist, it is shear in the $\mathbf{E} \times \mathbf{B}$ flow velocity that can stabilize these fluctuations.

The importance of $\mathbf{E} \times \mathbf{B}$ shear can be understood in another way [14]. For a given mode, the phase and group velocities of the associated turbulence can be a complicated function of various plasma parameters. However, because all particles move with the same $\mathbf{E} \times \mathbf{B}$ velocity, this velocity will contribute to all modes. Thus, even though the stability of a given mode may depend on a number of parameters, if that mode can be stabilized by shear flow, it should be affected by sufficiently strong, sheared $\mathbf{E} \times \mathbf{B}$ flow. In this sense, $\mathbf{E} \times \mathbf{B}$ flow shear provides a virtually universal mechanism for reduction of turbulence.

The radial electric field is the gradient of the electrostatic plasma potential ($E_r = -\nabla V_p$). Thus, E_r and $\mathbf{E} \times \mathbf{B}$ can be determined with an electrostatic probe and knowledge of $\mathbf{B}(r)$. Alternatively, and more commonly, E_r can be constructed from measurements of fluid flow and pressure using the radial force balance equation [21],

$$E_r = \nabla P_i(n_i Z_i e)^{-1} - (\mathbf{V}_i \times \mathbf{B})_r = \nabla P_i(n_i Z_i e)^{-1} - V_\theta B_\phi + V_\phi B_\theta, \qquad (1)$$

to be evaluated for particle species i (fuel ion, impurity ion, or electron).

Here, n_i is the particle density, Z_i is the charge, P_i is the pressure, $\mathbf{V}_i$ is the fluid velocity, and $\mathbf{B}$ is the magnetic field. The subscripts θ and ϕ represent the poloidal and toroidal directions, respectively. There is a term $\propto \mathbf{V}\cdot\nabla\mathbf{V}$ neglected in this equation. Justifications for this omission are discussed in detail by Burrell *et al.* [22]. This term can make a nonzero contribution to the force balance equation in two ways: (1) through lowest-order average flows and (2) through a nonzero time-average of velocity fluctuations. Burrell *et al.* demonstrate that (1) should be small and that while (2) can conceivably make a significant contribution, there is as yet no data to verify or deny this.

The E_r that results from Eq. (1) should be the same for all particle species. This was tested by Kim *et al.* [23] on the DIII-D tokamak by measuring all three terms in the equation for fuel and impurity ions. First, they found that *the rotation of fuel ions differs in both magnitude and direction from that of the impurity ions* in the edge of H-mode discharges, as predicted theoretically by Kim *et al.* [15]. This has important consequences for any measurement of plasma rotation based solely on one particle species. Second, in spite of the large differences in rotation between species, they found that E_r calculated from Eq. (1) was, indeed, the same for both impurity and fuel ions. Prior to these measurements, only impurity rotation was typically measured (easier to measure than fuel ion rotation), and much theoretical work was devoted to explaining only the behavior of impurity ion poloidal rotation, without regard for toroidal rotation or the pressure gradient. It is now clear that all three terms in Eq. (1) can be significant.

The cylindrical model of Biglari *et al.* [9] has now been extended to

full toroidal geometry [24], providing a more realistic expression for the $\mathbf{E}\times\mathbf{B}$ flow shearing rate:

$$\omega_s = (RB_\theta)^2/B \times (\partial/\partial\Psi)E_r/RB_\theta, \qquad (2)$$

where R is the major radius, B is the total magnetic field, and Ψ is the radial flux coordinate. In the edge of H-mode discharges, $\omega_s \sim 6\times 10^5/s$, at least an order of magnitude larger than the rate of turbulent radial scattering [14]. Thus, H-mode discharges easily satisfy the strong shear limit, and fluctuations can be reduced.

Regardless of the strong shear criterion, however, it is possible for $\mathbf{E}\times\mathbf{B}$ flow shear, or any flow shear, to *drive* instability. In neutral fluid dynamics, one usually thinks of sheared flow velocity as a source of free energy that can drive turbulence through Kelvin-Helmholtz instabilities [25]. Fortunately, in a magnetized plasma, magnetic shear can preclude such instability. In a plasma of finite resistivity, the criterion for Kelvin-Helmholtz stability in the presence of $\mathbf{E}\times\mathbf{B}$ flow shear (in cylindrical geometry) is [9,14]:

$$\nabla E_r/E_r < (\eta\Delta\omega_t)^{-1/4}(V_A k_y/L_s c)^{1/2}, \qquad (3)$$

where η is the plasma resistivity, V_A is the Alfvén velocity, k_y is the poloidal wave number of the mode (fluctuation) in question, L_s is the magnetic shear length, and c is the speed of light. In H-mode discharges in the tokamak, this criterion comes closest to being violated in the edge, where ∇E_r and η are largest. Nevertheless, for typical

parameters, this criterion is satisfied and Kelvin-Helmholtz instability does not develop [14].

2.2 The transition to H-mode

In this section, I first illustrate the importance of wall conditioning and fueling techniques for the achievement of an H-mode. Then I briefly describe the evolution of E_r and the edge fluctuations through the transition to H-mode. I also give a short description of some recent theoretical work relating to the transition.

2.2.0 Wall conditioning and fueling

Observations from many devices have revealed an edge temperature threshold for the appearance of an H-mode [26]. This is related to the universally observed heating power threshold. By enhancing the edge radiated power and through collisional equilibration, fuel and impurity particles can cool the edge plasma and inhibit the transition to H-mode. The plasma-facing wall is a source of both neutral and ionized fuel and impurity particles, and neutral fuel particles also originate from external fueling sources, such as puff valves.

The deleterious effect of impurities was made clear in the first H-mode experiments on ASDEX [1]. It was observed that the addition of methane or krypton gas to the discharges could prevent an H-mode from being triggered. Most devices in which the H-mode is observed employ one or more techniques for conditioning the plasma-facing wall and minimizing impurity influx. These techniques include boronization

and glow discharge cleaning in helium [27]. With these techniques, the H-mode power threshold is lowered, presumably due to an already hotter edge plasma, and H-mode confinement improves [2].

Fueling techniques can also be important, particularly for machines fueled primarily with puff valves (as opposed to neutral beams). Typically, puff valves are turned off during H-mode, because recycling and desorption of fuel from the plasma-facing wall, coupled with the increased particle confinement time, are sufficient to sustain the plasma density. Further, turning off the puff valves is actually a requirement for triggering an H-mode in some devices. For example, H-mode in the Compass tokamak typically appears only after puffing stops [28], and puffing into an established H-mode discharge can cause it to revert to standard (degraded) confinement [29].

This fueling dependence can be understood in terms of the edge temperature threshold. The neutral fuel particles from puff valves are typically at room temperature, while fuel particles from the plasma-facing wall can have temperatures of several eV, and many are already ionized before entering the plasma [30]. Thus, recycled/desorbed "wall fuel" can result in lower radiated power and reduced collisional cooling of the edge plasma. Puffing is not always deleterious, however. An H-mode in the Tuman-3 tokamak can actually be triggered by an increase in the gas puff rate, as well as by injection of a fuel pellet [31].

The H-mode dependence on wall conditioning, fueling, and edge temperature must ultimately be explained in terms of the E_r gradient, determined by the pressure gradient and fluid flow terms in Eq. (1). However, the contribution to the terms of Eq. (1) from, e.g., neutral fuel

particles, is complicated. On the one hand, neutral fuel particles can reduce the edge temperature, thereby reducing the edge pressure and possibly its gradient. The reduced temperature can also increase edge viscosity, which damps flow shear. Thus, the E_r gradient is reduced. On the other hand, neutral particles are a source of plasma ions, so their contribution to the plasma density can enhance the pressure gradient, which can increase the likelihood of an H-mode transition. This may partially explain the observation of gas-puff-induced H-mode in Tuman-3 [31]. The idea that neutral particles can contribute to the H-mode transition was discussed by Carreras *et al.* [32].

2.2.1 Radial electric field at the H-mode transition

Several questions about the evolution of E_r during the transition to H-mode were just recently answered experimentally. One fundamental question was in regard to the paradigm of $\mathbf{E} \times \mathbf{B}$ flow shear reduction of fluctuations. At the transition, does flow shear develop *before* fluctuations decrease (as one would hypothesize)? Moyer *et al.* [33] found that this is indeed the case in DIII-D. Another important question was: what term(s) in Eq. (1) contributes to E_r and its gradient right at the transition? Moyer *et al.* [33] also addressed this question, finding that the $(\mathbf{V} \times \mathbf{B})$ term was dominant at the transition, but that the ∇P term became important soon thereafter.

In the last few years, there have been many theories attempting to explain/model the transition to the H-mode state. One fairly recent theory, based partially on earlier work [34,35], was discussed by Diamond *et al.* [36]. Their theory describes the plasma self-generation

of sheared poloidal flow due to the fluctuation-based Reynold's stress, which then contributes to a gradient in the radial electric field and can lead to the transition to H-mode. They derive the following equation for the time evolution of the flux-surface-averaged poloidal velocity:

$$\partial\langle V_\theta\rangle/\partial t = -\partial/\partial r[\langle v_r v_\theta\rangle - \langle b_r b_\theta\rangle/\rho_m \mu_o] - \mu\langle V_\theta\rangle,$$

where the first term on the right hand side is the Reynold's stress, and the second term represents flow damping by magnetic pumping. The quantities v and b are velocity and magnetic field fluctuations. The Reynold's stress is largest where the fluctuation amplitude exhibits a large radial derivative, e.g., near a low order rational surface.

The Reynold's stress mechanism can operate far from the plasma edge, unlike transition mechanisms from earlier work (e.g., Ref. 37) that relied on (nonambipolar) ion orbit loss (scrapeoff) in the extreme edge. Thus, the theory of Diamond *et al.* can help describe enhanced confinement discharges other than H-mode in which $\mathbf{E} \times \mathbf{B}$ flow shear is strong over much of the plasma core, and the core plays an important role in the global confinement improvement (see Sec. 2.5 for examples).

2.3 Fluctuations and confinement in the edge and core

In accordance with the theory of Biglari *et al.* [9], both density and floating potential (electrostatic) fluctuations are reduced in the H-mode shear region [2,8,33,39]. The density profile, and sometimes the temperature profile, steepen in this region, indicating the presence of a transport barrier [8]. Electrostatic fluctuations beyond the shear region

in the scrape-off layer are sometimes reduced as well [33,40,41]. The reduction beyond the shear region is not well understood, but it has been suggested that, e.g., the pressure profile in this region may be flattened, thus reducing the drive for turbulence, or that the small E_r gradient in this region is still sufficient for fluctuation reduction.

In addition to electrostatic fluctuations, there have been a few observations of reduced magnetic fluctuations in the edge of H-mode discharges [8,42,43], and in one case [42], this reduction was estimated to account for the H-mode confinement improvement. In the tokamak, the large stabilizing toroidal magnetic field results in a relatively low level of magnetic fluctuations (normalized to the equilibrium field). Thus, it is more commonly believed that electrostatic fluctuations are the primary cause of particle and energy transport and that their reduction in H-mode accounts for the bulk of the confinement improvement. However, to my knowledge, the possible significance of magnetic fluctuations has not been ruled out.

In the plasma core, density fluctuations and thermal diffusivity are reduced during H-mode, and various possibilities for this reduction have been proposed [8]. They include a flattening of the core density profile due to the steepening in the edge shear region, penetration of E_r gradients into the core region, and modification of the current density profile due to bootstrap current driven in the edge shear region.

A set of experiments [44,45,46] on the DIII-D tokamak showed that $\mathbf{E} \times \mathbf{B}$ flow shear plays at least some role in the H-mode reduction of core fluctuations. However, these experiments also revealed that the changes in the plasma core play a minor role in the overall H-mode

confinement improvement. In a technique referred to as "magnetic braking," a static radial magnetic field (error) is applied to slow the toroidal rotation of the core plasma. The error field does not affect the core pressure gradient or poloidal rotation, however. The toroidal rotation V_ϕ [Eq. (1)] in the core is normally in the direction to increase E_r, which is positive in the core. Thus, the reduction of V_ϕ reduces E_r and its gradient, as well as the shear in the $\mathbf{E} \times \mathbf{B}$ flow. Qualitatively consistent with the theory of Biglari *et al.* [9], the amplitude of the core density fluctuations increased with braking by a factor of 1.5 – 2 [45]. Note that the radial correlation lengths of the affected core fluctuations are of the order of a few centimeters [2], while the core $\mathbf{E} \times \mathbf{B}$ flow shear region extends over much of the minor radius.

In the equilibrium phase of the H-mode, the $\mathbf{E} \times \mathbf{B}$ flow shear in the edge is dominated by the diamagnetic (pressure gradient) term [Eq. (1)]. Thus, it is little affected by the error field [46]. Unexpectedly, application of the braking field and the resultant increase in core fluctuations did not significantly degrade the global energy confinement time [45,46]. This is particularly surprising since the error field might be expected to drive large magnetic islands and thermal transport in the core. This result suggests that the global confinement improvement in H-mode discharges is due primarily to the fluctuation reduction in the edge (i.e., the edge determines global confinement).

2.4 Edge-localized modes

An edge-localized mode (ELM) [10] is a discrete (in time), burst-like magnetohydrodynamic instability that occurs in the edge of H-

mode discharges in tokamaks and stellarators. Occurring with a repetition frequency ranging from 10–200 Hz, ELM's appear in various signals such as H_α or D_α emission and the edge radial magnetic field [10]. Several types of ELM's have been identified [10,47,48], and at least one type is believed to be driven by the large pressure gradient associated with the edge shear region. The primary significance of ELM's is their momentary impact on edge particle and energy transport. Each ELM destroys the transport barrier (strong flow shear region), but the barrier is quickly restored following the ELM. Thus, each ELM briefly reduces H–mode confinement, leading one to conclude that suppression of ELM's would be desirable.

The repetition frequency of one ELM variety decreases with increasing heating power, and with sufficient heating power, this type of ELM can be totally suppressed, leading to so–called ELM–free H–mode [10]. As expected, the absence of ELM's does result in improved confinement, but only temporarily. It is found that without ELM's, the improved impurity particle confinement time results in accumulation of impurities in the plasma core. This increases the radiated power loss from the plasma, eventually causing the uncontrolled termination of the H–mode [8].

From a fusion reactor standpoint, such uncontrolled, non–steady–state behavior is undesirable. Thus, recent work has actually focused on inducing ELM's [49,50,51]. This reduces the maximum H–mode confinement, but allows steady state H–mode operation, sometimes lasting as long as the device pulse length [8]. The repetition rate of one type of ELM can actually be increased with additional heating power

[10]. Alternatively, the repetition rate can be increased by applying an appropriate static or rotating magnetic field perturbation [49,50,51]. The techniques for ELM control are so advanced today that the ELM repetition frequency can be increased or decreased at will. Unfortunately, while ELM's are controllable and well characterized empirically, there is as yet no theory that can account for their multifarious behavior.

2.5 Other enhanced confinement discharges relying on $\mathbf{E} \times \mathbf{B}$ flow shear

Several other enhanced confinement regimes have been observed in recent years, and all appear to have some dependence on $\mathbf{E} \times \mathbf{B}$ flow shear. One type is referred to as biased H–mode, and it has been achieved in tokamaks [52,53,54] and a linear tandem mirror [55]. In these discharges, an insertable biased probe drives a radial current across the outer magnetic flux surfaces. This increases the radial electric field and plasma rotation, resulting in the formation of a transport barrier. Interestingly, this typically results in a substantial increase in the particle confinement time with little or no increase in the energy confinement time.

Some tokamak discharges have exhibited much improved core confinement, beyond that achieved in H–mode. These discharges are characterized in part by strong $\mathbf{E} \times \mathbf{B}$ flow shear and fluctuation reduction over a substantial portion of the plasma core. One such discharge type is the VH–mode (very–high–confinement mode) [56]. This was first discovered following intensive boronization in the DIII–D tokamak. Global confinement in the VH–mode is roughly twice that of

the H-mode. More recently, tokamak discharges involving both E_r gradients and "negative magnetic shear" (where the q-profile has a local off-axis minimum in the core region) have exhibited core transport *reduced to the level predicted by neoclassical theory* [57,58]. Transport at the neoclassical level is the theoretical minimum achievable in tokamaks. Thus, $\mathbf{E} \times \mathbf{B}$ flow shear is emerging as a universal means of improving both edge and core confinement in magnetic fusion devices.

2.6 The relevance of H-mode physics to the RFP

Since no H-mode-like phenomena have been previously observed in the RFP, no RFP-specific theoretical work has been done in the area of $\mathbf{E} \times \mathbf{B}$-flow-shear reduction of fluctuations. Nevertheless, this paradigm may still be applicable in certain cases.

In the edge of the RFP, particle transport is driven by electrostatic fluctuations [59], while the mechanism underlying energy transport has not been identified. In the RFP core, magnetic fluctuations have been measured to account for both particle [60] and energy [61] transport, and these fluctuations are generally believed to determine RFP energy confinement.

In analogy with H-mode discharges, a 1 – 2 cm wide region of strong $\mathbf{E} \times \mathbf{B}$ flow shear in the edge of the RFP could affect the electrostatic fluctuations residing there. Existing analytical work, such as that of Biglari *et al.* [9], predicts the reduction of fluctuations whose correlation lengths are less than the width of the shear region. High frequency electrostatic fluctuations (with short correlation lengths) can, thus, be susceptible to strong $\mathbf{E} \times \mathbf{B}$ flow shear. However, lower

frequency fluctuations can have correlation lengths >> 2 cm, so while their reduction by localized $\mathbf{E} \times \mathbf{B}$ flow shear is conceivable, such an interaction has not been described analytically. The magnetic fluctuations in the core are global, i.e., their perturbative effects (eigenfunctions) extend over most of the plasma. Thus, they would overlap any region of strong $\mathbf{E} \times \mathbf{B}$ flow shear in the edge. However, it is not known if the shear could affect these fluctuations.

In tokamaks, electrostatic fluctuations are generally believed to determine global energy confinement. Thus, the edge reduction of electrostatic fluctuations by strong shear is sufficient to explain the improved energy confinement of H-mode discharges. If strong shear in the RFP were only able to affect the (small-scale) electrostatic fluctuations in the edge, then the impact of the shear on RFP energy confinement would presumably be small. If, on the other hand, local shear is able to affect longer wavelength magnetic (and electrostatic) fluctuations, the effect on energy confinement could be pronounced.

Regardless of possible differences between the tokamak and RFP in the effect of strong $\mathbf{E} \times \mathbf{B}$ flow shear on confinement, the mere formation of the radial electric field gradient should still be governed by the same underlying physics, embodied by Eq. (1). Thus, the influences of, e.g., edge heating, fuel isotope, fueling technique, and wall conditioning could be similar. If $\mathbf{E} \times \mathbf{B}$ flow shear can play some role in RFP confinement, the RFP community should be able to more easily harness the shear by drawing on the copious experience with the H-mode in other devices.

References

[1] F. Wagner *et al.*, Phys. Rev. Lett. **49**, 1408 (1982).

[2] K. H. Burrell, Plasma Phys. Controlled Fusion **36**, A291 (1994).

[3] S. Sengoku *et al.*, Phys. Rev. Lett. **59**, 450 (1987).

[4] T. H. Osborne *et al.*, Nucl. Fusion **30**, 2023 (1990).

[5] M. V. Andrejko *et al.*, Plasma Phys. Control. Fusion **36**, A165 (1994).

[6] V. Erckmann *et al.*, Phys. Rev. Lett. **70**, 2086 (1993).

[7] K. Toi *et al.*, Plasma Phys. Controlled Fusion **36**, A117 (1994).

[8] R. J. Groebner, Phys. Fl. B **5**, 2343 (1993).

[9] H. Biglari, P. H. Diamond, and P. W. Terry, Phys. Fl. B **2**, 1 (1990).

[10] H. Zohm, Plasma Phys. Controlled Fusion **38**, 105 (1996).

[11] T. N. Carlstrom, Plasma Phys. Controlled Fusion **38**, 1149 (1996).

[12] F. Wagner *et al.*, Phys. Rev. Lett. **53**, 1453 (1984).

[13] M. Kaufman *et al.*, Plasma Phys. Controlled Fusion **35**, B205 (1993).

[14] K. H. Burrell *et al.*, Phys. Plasmas **4**, 1499 (1997).

[15] Y. B. Kim, P. H. Diamond, and R. J. Groebner **3**, 2050 (1991).

[16] S. K. Wong and F. L. Hinton, Phys. Rev. Lett. **52**, 827 (1984).

[17] F. L. Hinton and S. K Wong, Phys. Fluids **28**, 3082 (1985).

[18] R. J. Groebner, K. H. Burrell, and R. P. Seraydarian, Phys. Rev. Lett. **64**, 3015 (1990).

[19] K. Ida *et al.*, Phys. Rev. Lett. **65**, 1364 (1990).

[20] Y. B. Kim *et al.*, Phys. Fl. B **3**, 384 (1991).

[21] F. L. Hinton and R. D. Hazeltine, Rev. Mod. Phys. **48**, 239 (1976).

[22] K. H. Burrell *et al.*, Phys. Plasmas **1**, 1536 (1994).

[23] J. Kim *et al.*, Plasma Phys. Controlled Fusion **36**, A183 (1994).

[24] T. S. Hahm and K. H. Burrell, Phys. Plasmas **2**, 1648 (1995).

[25] S. Chandrasekhar, Hydrodynamic and Hydromagnetic Stability (Dover, New York 1981).

[26] R. J. Groebner *et al.*, Plasma Phys. Controlled Fusion **36**, A13 (1994).

[27] J. Winter, Plasma Phys. Controlled Fusion **38**, 1503 (1996).

[28] S. J. Fielding *et al.*, Plasma Phys. Controlled Fusion **38**, 1091 (1996).

[29] P. G. Carolan *et al.*, Plasma Phys. Controlled Fusion **36**, A111 (1994).

[30] G. M. McCracken and P. E. Stott, Nucl. Fusion **19**, 889 (1979).

[31] S. V. Lebedev *et al.*, Plasma Phys. Controlled Fusion **38**, 1103 (1996).

[32] B. A. Carreras, P. H. Diamond, and G. Vetoulis, Phys. Plasmas **3**, 4106 (1996).

[33] R. A. Moyer *et al.*, Phys. Plasmas **2**, 2397 (1995).

[34] P. H. Diamond and Y. B. Kim, Phys Fl. B **3**, 1626 (1991).

[35] B. A. Carreras, V. E. Lynch, and L. Garcia, Phys. Fl. B **3**, 1438 (1991).

[36] P. H. Diamond *et al.*, Phys. Rev. Lett. **72**, 2565 (1994).

[37] K. C. Shaing, E. C. Crume, and W. A Houlberg, Phys. Fl. B **2**, 1492 (1990).

[38] P. W. Terry (private communication).

[39] E. J. Doyle *et al.*, Phys. Fl. B **3**, 2300 (1991).

[40] E. Holzhauer *et al.*, Plasma Phys. Controlled Fusion **36**, A3 (1994).

[41] G. R. Tynan *et al.*, Plasma Phys. Controlled Fusion **36**, A285 (1994).

[42] N. Ohyabu *et al.*, Phys. Rev. Lett. **58**, 120 (1987).

[43] K. H. Burrell *et al.*, Phys. Fluids B **2**, 1405 (1990).

[44] R. J. La Haye *et al.*, Nucl. Fusion **33**, 349 (1993).

[45] C. L. Rettig *et al.*, Phys. Fl. B **5**, 2428 (1993).

[46] R. J. La Haye *et al.*, Phys. Plasmas **1**, 373 (1994).

[47] H. Zohm *et al.*, Nucl. Fusion **35**, 543 (1995).

[48] T. Ozeki *et al.*, Nucl. Fusion **30**, 1425 (1990).

[49] M. Mori *et al.*, in Proceedings of the 14th International Conference on Plasma Physics and Controlled Nuclear Fusion Research, Würzburg, 1992 (IAEA, Vienna, 1993), Vol. 2, p. 567.

[50] A. W. Morris *et al.*, in Proceedings of the 15th International Conference on Plasma Physics and Controlled Nuclear Fusion Research, Seville, 1994 (IAEA, Vienna, 1995), Vol. 1, p. 365.

[51] M. Mori, Plasma Phys. Controlled Fusion **38**, 1189 (1996).

[52] R. J. Taylor *et al.*, Phys. Rev. Lett. **63**, 2365 (1989).

[53] R. R. Weynants *et al.*, Proceedings of the 13th International Conference on Plasma Physics and Controlled Nuclear Fusion Research, Washington DC, 1990 (IAEA, Vienna, 1991), Vol. 1, p. 473.

[54] L. G. Askniazi *et al.*, Nucl. Fusion **32**, 271 (1992).

[55] O. Sakai, Y. Yasaka, and R. Itatani, Phys. Rev. Lett. **70**, 4071 (1993).

[56] G. L. Jackson *et al.*, Phys. Fl. B **4**, 2181 (1992).

[57] F. M. Levinton *et al.*, Phys. Rev. Lett. **75**, 4417 (1995).

[58] E. J. Strait *et al.*, Phys. Rev. Lett. **75**, 4421 (1995).

[59] T. D. Rempel *et al.*, Phys. Rev. Lett. **67**, 1438 (1991).

[60] M. R. Stoneking *et al.*, Phys. Rev. Lett. **73**, 549 (1994).

[61] G. Fiksel *et al.*, Phys. Rev. Lett. **72**, 1028 (1994).

3. Improved confinement and operational requirements

In this chapter, I quantify the improved confinement in EC and PPCD discharges (with emphasis on EC discharges), including a discussion of some potential pitfalls in the measurement/calculation of the particle and energy confinement times. I also discuss the operational requirements necessary for these discharges. These requirements include sufficiently strong toroidal magnetic field reversal, sufficiently low density, conditioning of the plasma-facing wall, control of magnetic field errors, and fueling without puff valves. In Sec. 3.0, I introduce EC and PPCD discharges with a brief summary of the operational requirements. In Sec. 3.1, I discuss and compare the improved confinement in these discharges. Section 3.2 delves further into the reversal and density requirements. In Sec. 3.3, I describe the mechanisms for impurity influx in the MST, and in Sec. 3.4, I discuss the wall conditioning techniques used to minimize impurity influx. Section 3.5 entails a discussion of the fueling techniques developed for EC discharges. Section 3.6 provides a brief chapter summary.

3.0 Introduction

Almost all MST discharges exhibit sawtooth oscillations [1,2,3], each comprised of a relatively slow rise phase and a more rapid crash phase. During the sawtooth rise phase, the μ profile (where $\mu = \mu_0 \mathbf{J}\cdot\mathbf{B}/B^2$, $\mathbf{J}$ is the current density, and $\mathbf{B}$ is the magnetic field) becomes centrally peaked as a result of resistive diffusion and the peaked parallel equilibrium inductive electric field. This peaking ultimately

leads to the crash phase, during which current parallel to **B** is redistributed, and $\mu(r)$ is flattened. Sawtooth crashes are discrete dynamo events. By generating edge parallel (~ poloidal) plasma current and toroidal magnetic flux, crashes help sustain the RFP magnetic configuration. However, sawtooth crashes are a very destructive form of dynamo, in that they correspond to a large increase in core-resonant magnetic fluctuations and the resultant degradation of particle and energy confinement. On the whole, sawteeth are detrimental to MST performance.

The sawtooth cycle time in normal discharges is typically 2 – 5 ms. However, discharges with a sawtooth cycle time up to 20 ms have now been observed [1]. In Fig. 1 is shown the cross-section-averaged toroidal magnetic field during a normal, sawtoothing discharge and during a discharge with sawtooth crashes temporarily suppressed. The discharge with crash suppression is an example of an enhanced confinement (EC) discharge. PPCD discharges are also characterized by sawtooth crash suppression, and the suppression lasts as long (or sometimes longer) than the PPCD pulse [4]. Further discussion of sawteeth and sawtooth crash suppression is included in Chapter 6.

In the case of EC discharges, it was initially believed that the improved confinement was due simply to the prolonged absence of sawtooth crashes, but discharges were later observed that had equally long sawtooth cycle times *without* significantly improved confinement (discussed later in this chapter). In Chapter 4, I illustrate that one (or possibly the) difference between these two cases is the presence of a strongly sheared $\mathbf{E} \times \mathbf{B}$ flow in the edge of those discharges with

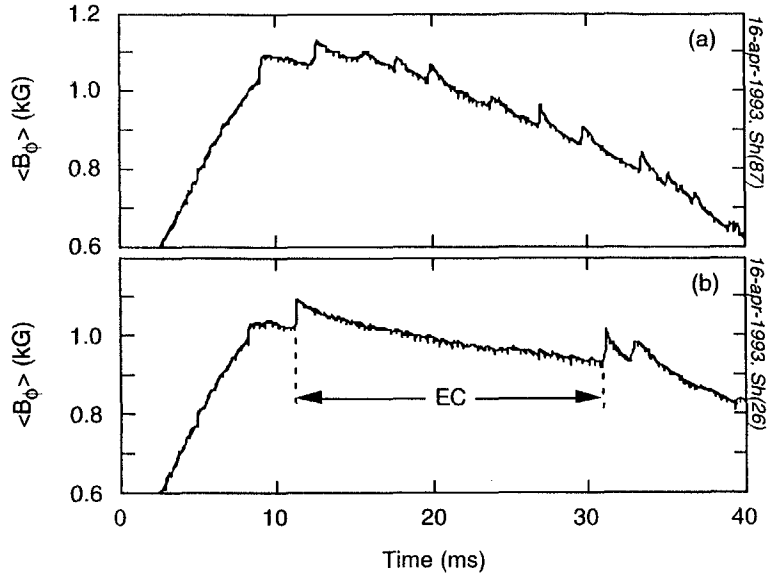

Fig. 1. Time variation of the cross-section-averaged toroidal magnetic field in (a) a normal sawtoothy discharge and (b) a discharge with an enhanced confinement (EC) period.

enhanced confinement. Chapter 4 also illustrates that PPCD discharges also exhibit strong radial electric field gradients.

Subject to constraints on toroidal magnetic field reversal, electron density, wall conditioning, magnetic field errors, and fueling, EC and PPCD discharges are achievable at all plasma currents of which the MST is capable (100 kA $\leq I_\phi \leq$ 600 kA). The two most important operational requirements for EC discharges are sufficiently strong toroidal field reversal and sufficiently low density. The toroidal field reversal is

represented by $F \equiv B_\phi(a)/\langle B_\phi \rangle$, where $B_\phi(a)$ is the toroidal field at the edge, and $\langle B_\phi \rangle$ is the cross-section average. The reversal and density requirements relax with increasing I_ϕ. For example, at 200 kA, the minimum (least negative) F is -0.5, and the maximum line-averaged density, $\langle n_e \rangle$ is 6×10^{12} cm^{-3}. At 500 kA, the minimum F is -0.2, and the maximum $\langle n_e \rangle$ is 1.2×10^{13} cm^{-3}. The required reversal and density vary smoothly with plasma current. PPCD automatically satisfies the reversal requirement [4,5], and it has a density dependence that varies with plasma current. However, for a given plasma current, PPCD appears to have a higher density limit than EC discharges.

Careful conditioning of the plasma-facing wall to minimize impurity influx is also required. EC discharges and high-quality PPCD discharges were first obtained following boronization [1,5,6,7], but both are now achievable with more standard wall conditioning techniques such as pulsed discharge cleaning in helium [7]. Also necessary for minimization of impurity influx is control of magnetic field errors [8], primarily at the poloidal gap (vertical cut in the conducting shell). Data shown in a later section illustrates that field errors can result in substantial plasma-wall interaction and impurity influx.

Both the fuel and the fueling method also play a role. Deuterium generally provides longer and more reproducible EC periods than hydrogen, and wall fueling is preferred over gas puff fueling. Wall fueling is achieved by turning off the puff valves after formation of the discharge, allowing the wall (including the limiters) to provide the necessary fuel through recycling and other processes. PPCD may exhibit a similar fuel and fueling dependence, but careful comparisons have not

been made. I have found, however, that the combination of deuterium and wall fueling leads to high quality PPCD discharges.

Consider the conditions in which the first EC discharges were achieved (in the fall of 1992). Periods of enhanced confinement occurred in ~ 350 kA hydrogen RFP's with the required $F \sim -0.3$ and $\langle n_e \rangle \leq 1 \times 10^{13}$ cm^{-3}. The MST had been in operation since 1988, so this combination of F and $\langle n_e \rangle$ had certainly been tried before 1992 but *without* the achievement of EC discharges. The reason EC discharges finally occurred, I believe, is that the condition of the plasma-facing wall and control of field errors had evolved sufficiently. This was due in part to initial experiments with boronization and new improvements in field error control at the poloidal gap. Wall conditioning and field error control are still vital to both EC and PPCD discharges.

3.1 Improved confinement

Before quantifying the confinement of EC and PPCD discharges, I illustrate the differences between standard and EC discharges in Fig. 2. These discharges are in hydrogen with I_ϕ = 450 kA, and they are the same discharges as shown in Fig. 1. They have the same operational parameters, including strong toroidal field reversal and sufficiently low density, but as I discuss in a later section, the discharge on the left develops a large magnetic field error after 10 ms. The central electron temperature, indicated roughly by the ratio of two soft x-ray signals (see Chapter 1), is shown in Figs. 2(a) and 2(e), and the Ohmic input power is shown in Figs. 2(b) and 2(f). The emission from carbon (impurity) ions in the plasma edge is shown in Figs. 2(c) and 2(g). Brief

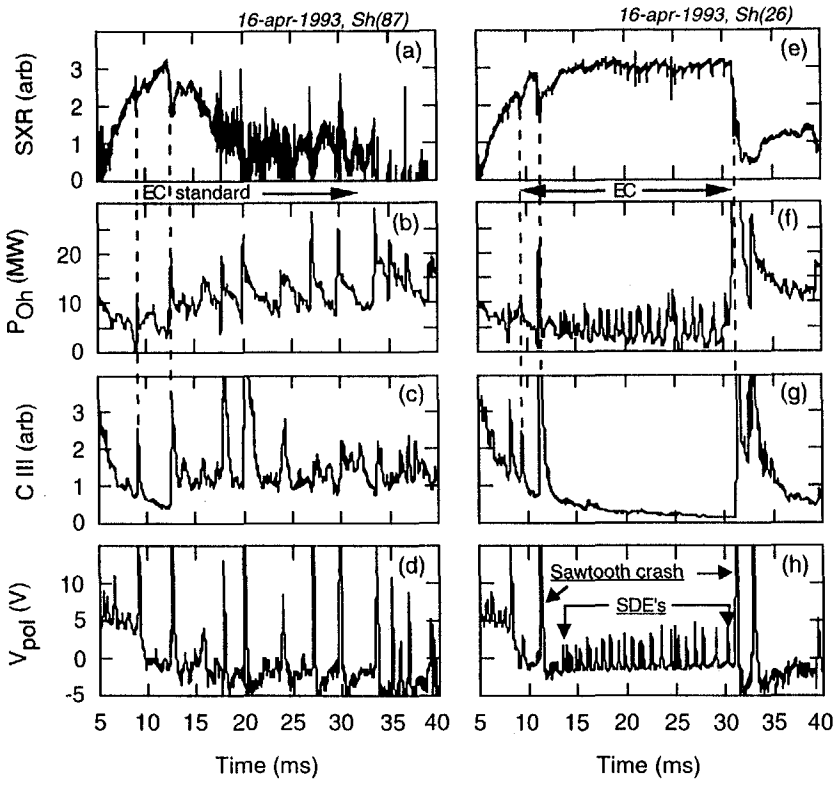

Fig. 2. Time variations of (a) ratio of two soft x-ray signals ∝ core electron temperature, (b) Ohmic input power, (c) C III (464.74 nm) radiation, and (d) surface poloidal voltage in a standard discharge. These same parameters are shown in (e) - (h) for an enhanced confinement discharge. Sawtooth crashes occur throughout the discharge on the left and occasionally in the discharge on the right. Small dynamo events (SDE's) occur throughout the EC period on the right.

periods of enhanced confinement occur in both discharges around 10 ms, as denoted in the figure. Shortly after 10 ms, these periods are interrupted by sawtooth crashes, during which the central electron temperature drops, and both the Ohmic input power and impurity radiation increase. The discharge on the left then degrades to standard confinement, while the discharge on the right exhibits a sustained period of enhanced confinement. With enhanced confinement, the central electron temperature is higher, and the Ohmic input power is lower. Radiation power loss from edge impurities is also reduced, as is the radiation from neutral fuel atoms (not shown).

In addition to illustrating the difference between standard and enhanced confinement, these two discharges also illustrate that enhanced confinement does not always produce a longer-than-normal sawtooth cycle time. The length of EC periods (which is determined by the sawtooth cycle time) observed to date has ranged from about 2 – 20 ms. The long EC period on the right in Fig. 2 also serves to introduce so-called small dynamo events (or SDE's, the subject of Chapter 5), which are the small bursts evident in the Ohmic input power. Both SDE's and sawtooth crashes appear in the surface poloidal voltage [e.g., Fig. 2(h)] as well, which increases in response to an increase in the toroidal flux in the plasma volume. In addition to producing toroidal flux, SDE's also cause a momentary degradation of confinement, as they increase the Ohmic input power and decrease the central electron temperature (looking closely at the soft x-ray plot).

The EC energy confinement time was measured in discharges similar to that on the right in Fig. 2. The discharges have a toroidal

plasma current, I_ϕ = 400 - 500 kA and line-averaged density, $\langle n_e \rangle \leq 1 \times 10^{13}$ cm^{-3}. Unlike the case in Fig. 2, however, the Ohmic power (averaged over, e.g., 1 - 2 ms) in most EC periods can vary substantially with time due to large variations in SDE spacing and amplitude.

The energy confinement time, $\tau_E \equiv$ (stored thermal energy)/(Ohmic input power), is defined as follows:

$$\tau_E = [(3/2)\int(n_e T_e + n_i T_i)dV]/P_{Ohmic}, \quad (1)$$

where n_e and n_j are the electron and ion densities, and T_e and T_i are the electron and ion temperatures. The integral is over the plasma volume. Calculation of τ_E is based on measurements of $\langle n_e \rangle$, $T_e(0)$, $T_i(0)$, and the Ohmic input power. Assuming a quartic shape for all the profiles, e.g., $n_e(r) = n_e(0)[1 - (r/a)^4]$, and assuming $n_i(r) = n_e(r)$ and $T_i(r) = (0.75)T_e(r)$ [based only on the fact that the measured $T_i(0) \approx (0.75)T_e(0)$], one arrives at the following formula:

$$\tau_E \approx (0.0224)\langle n_e \rangle T_e(0)/P_{Ohmic}, \quad (2)$$

where $[\tau_E]$ = ms, $[\langle n_e \rangle] = 10^{13}$ cm^{-3}, $[T_e(0)]$ = eV, and $[P_{Ohmic}]$ = MW.

One can also calculate β_p, the poloidal beta, which is the ratio of the volume-averaged plasma thermal pressure to the edge poloidal magnetic field pressure. The poloidal beta is a measure of the efficiency with which the applied poloidal magnetic field is able to confine the plasma. With the above assumptions, one derives the following formula:

$$\beta_p \approx (46900)\langle n_e \rangle T_e(0)/B_\theta^2(a), \quad (3)$$

where $[\beta_p]$ = %, $[B_\theta(a)]$ = G, and the units of $\langle n_e \rangle$ and $T_e(0)$ are as above.

The assumed shape of the density and temperature profiles is based on existing measurements of $n_e(r)$ and $T_e(r)$. The full electron density profile has been measured in EC and PPCD discharges (see Chapter 5) and reveals that the quartic assumption is actually conservative for n_e (i.e., the profile can be flatter than quartic). Taking $n_i = n_e$ is based simply on the assumption of quasineutrality and $Z_{eff} \approx 1$. The electron temperature has only been measured at two spatial locations, r/a = 0 and r/a ~ 0.5, and the off-axis data is from standard discharges only. These two data points indicate that $T_e(r)$ is quite flat. The shape of $T_i(r)$ is unknown, and it could be nonmonotonic due to effects such as local anomalous ion heating [9].

Probably the largest uncertainty in τ_E arises from the Ohmic input power, which is calculated from the power balance relation, $P_{Ohmic} = P_{total} - dU_m/dt$. Here, P_{total} is the total power externally input to the plasma, which can be measured accurately, and U_m is the inductive stored energy (energy stored in the magnetic field), which must be calculated with an RFP equilibrium model. Thus, the Ohmic power is what remains of the total input power after subtracting the fraction of the total that goes to increasing the magnetic field energy. For the EC discharges described here, U_m and dU_m/dt are calculated with the polynomial function model or PFM [10], based on measurements of $F \equiv B_\phi(a)/\langle B_\phi \rangle$ and $\theta = B_\theta(a)/\langle B_\phi \rangle$ throughout each discharge.

The PFM and all other equilibrium models prove inadequate when

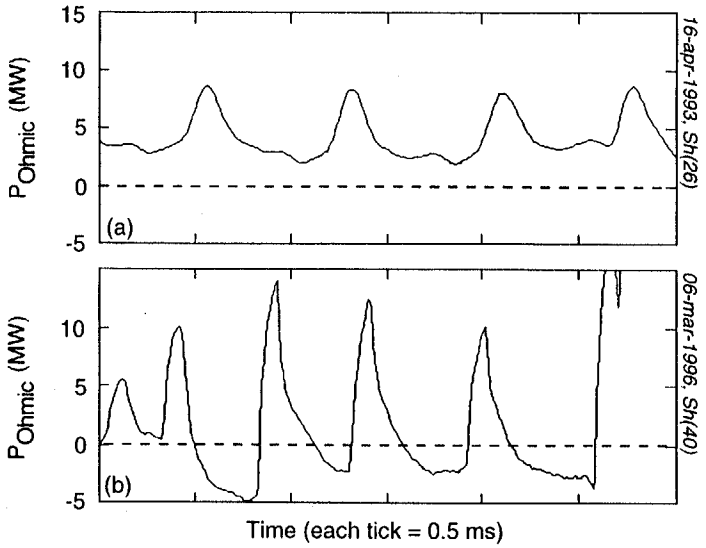

Fig. 3. Ohmic input power during EC periods with (a) F = -0.26 and (b) F = -0.65. Each burst is a small dynamo event (except for the sawtooth crash in the last 0.5 ms of (b). The discharge in (a) is the same as that on the right in Fig. 2.

faced with rapid changes to the equilibrium, such as occurs at sawtooth crashes and small dynamo events. To illustrate the effect of small dynamo events, I plot in Fig. 3 the Ohmic input power (calculated with the PFM) from two EC periods. The EC period in Fig. 3(a), which is a portion of the long EC period in Fig. 2, has *relatively* weak toroidal field reversal, while the period in Fig. 3(b) has much stronger reversal. As I discuss further in the next section and in Chapter 5, the amplitude of

SDE's in all parameters that SDE's affect increases as reversal is strengthened. When the SDE's become large as in Fig. 3(b), the Ohmic power between them is often negative, which is unphysical. The EC discharges in which τ_E has been measured thus far have had large plasma current, thereby allowing relatively weak reversal. Thus, as illustrated in Fig. 3(a), the Ohmic power in these periods does not generally become negative between SDE's. Even so, this does not assure that the PFM or any model is correct.

PPCD discharges are characterized by strong toroidal field reversal and large SDE's, similar to those of Fig. 3(b), so much effort has been devoted to verifying the accuracy of the various equilibrium models in these discharges. In one case, experimental measurements of the plasma internal inductance were compared with a calculation of this quantity using the so-called alpha model, a three-parameter cylindrical equilibrium model [4]. The internal inductance, $L_i \equiv [2/a^2 B_\theta^2(a)]\int B_\theta^2 r dr$, is determined experimentally by measurement of the poloidal asymmetry of B_θ at the plasma surface, $B_\theta(\theta) = \langle B_\theta(a)\rangle[1 + \Lambda(a/R)\cos\theta]$. The poloidal asymmetry factor, Λ, is related to L_i by $\Lambda = L_i/2 + \beta_p - 1$. It was shown in Ref. 4 that the measured and calculated L_i were in close agreement, thus bolstering confidence in the model calculation of P_{Ohmic}.

However, this agreement between experiment and model was based on an ensemble of discharges, in which the effects of SDE's were smoothed out. With individual SDE's (particularly those of larger amplitude), *all of the models fail in the calculation of the Ohmic input power*. This is true for both PPCD and EC discharges. Since P_{Ohmic} =

$P_{total} - dU_m/dt$, the negative excursions result from overestimation of the change in magnetic stored energy. Thus, only in a time-averaged sense, averaging over several SDE's, can the models be at all trusted. In Chapter 7, I will discuss what can be done in the attempt to more accurately calculate the Ohmic input power.

Comparisons of the various models to one another have also been made, and in a time-averaged sense, they agree fairly well with one another. For instance, the Ohmic input power calculated with both the PFM and the alpha model was compared for the long EC period in Fig. 2. The PFM calculated Ohmic power exhibits peak-to-peak SDE amplitudes like those seen in Figs. 2 and 3(a), while the alpha (and other) models produce larger peak-to-peak amplitudes, including larger negative excursions. Regardless of the calculated difference in SDE behavior, however, the average Ohmic power from 20 – 30 ms, e.g., was 3.5 MW according to the PFM and 2.6 MW according to the alpha model. This approximately 25% difference is not too large considering the markedly different peak-to-peak SDE amplitudes.

A comparison of the measured and calculated plasma internal inductance has not been made for EC discharges, but unlike PPCD discharges, EC discharges are as close to steady state (averaging over SDE's) as MST discharges come. Thus, the average Ohmic input power should be more amenable to equilibrium model calculation in these discharges. As reflected in the case above, the time-averaged Ohmic input power calculated by the PFM is consistently larger than that calculated by other models [5]. Thus, for a conservative estimate of the Ohmic input power in EC discharges, I utilize the PFM. Note again,

Table 1. Confinement parameters during EC and standard discharges with the same (strong) reversal.

	EC	standard
I_ϕ	497 kA	482 kA
$\langle n_e \rangle$	1.0×10^{13} cm^{-3}	1.1×10^{13} cm^{-3}
$T_e(0)$	571 eV	344 eV
P_{Ohmic}	3.9 MW	8.0 MW
τ_E	3.3 ms	1.1 ms
β_p	7.3%	5.3%

however, that in the calculation of τ_E, it is imperative that the Ohmic power be time-averaged. This is the case in the confinement data presented next.

The energy confinement time and poloidal beta are calculated for EC periods by taking a > 1 ms average over $\langle n_e \rangle$ and P_{Ohmic}, centered on the Thomson scattering laser firing time. To allow reasonable fits to the Thomson scattering data, several discharges must be ensemble averaged. The ensemble average energy confinement time and poloidal beta were measured in both hydrogen and deuterium discharges, and they had similar values in each case, regardless of the plasma current (400 or 500 kA). One ensemble of hydrogen EC discharges resulted in the confinement parameters shown in Table 1. The same parameters are shown for standard discharges with the same toroidal field reversal. An example of a typical standard discharge in this case is shown on the left in Fig. 2. Thus, the energy confinement time of EC discharges is

triple the standard value, while the increase in β_p is more modest.

The best confinement parameters measured for PPCD thus far are $\tau_E \sim 5$ ms and $\beta_p \sim 9\%$, calculated from an ensemble of 340 kA discharges [4]. One possible reason for the difference between τ_E and β_p in EC and PPCD discharges lies in the difference in SDE behavior between the two cases. As is discussed in Chapter 5, one of the hallmarks of recent PPCD experiments has been the suppression of SDE's for multi-millisecond periods. Such PPCD discharges comprised the above 340 kA ensemble. On the other hand, SDE suppression has not been observed in EC discharges, except at low plasma current (200 kA, see Chapter 5). Thus, for this reason, the difference in β_p and τ_E in EC and PPCD discharges is unsurprising. Note that measuring $T_e(0)$ with Thomson scattering is not yet possible at the low electron density required for low current EC discharges (due to signal-to-noise limitations), but with a temporary suppression of confinement-degrading SDE's, EC confinement may approach that of PPCD.

The EC particle confinement time, τ_P, is unknown due to large uncertainty in the particle source rate. The particle source rate is usually estimated from measurements of the line radiation (H_α or D_α) from neutral fuel atoms. At present, the MST has only a single detector for this radiation. Such a local measurement can grossly misrepresent the source rate due to toroidal and poloidal asymmetries in fuel particle influx (e.g., near puff valves). Nevertheless, it is likely that τ_P does improve somewhat. The line-averaged density in EC periods typically remains constant or even increases, while the locally measured source rate apparently drops. The density evolution depends on a number of

factors, including the frequency and amplitude of SDE's and whether gas puffing is applied in addition to the ever-present wall fueling. PPCD discharges exhibit similar behavior.

For any estimates of τ_P in EC and PPCD discharges, there is a possible lesson to be learned from H-mode discharges in DIII-D. Rensink *et al.* [11] found that while the typical H-mode rise in core density was due in part to improved particle confinement, there was also a contribution from reduced screening of neutrals at the plasma edge, due to a thinning of the scrapeoff layer. With reduced screening, neutrals penetrate further into the plasma before being ionized, thereby improving their chance of reaching the plasma core. In essence, the edge fueling efficiency, in addition to the global particle confinement time, is improved during an H-mode.

3.2 Toroidal field reversal and density requirements

In this section, I will further discuss the need for sufficiently strong toroidal field reversal and sufficiently low density in EC discharges. To illustrate the reversal requirement, I compare in Fig. 4 two discharges with different reversal. Operationally, the discharges are otherwise the same, with a plasma current of ~ 400 kA and line-averaged density of $\sim 7 \times 10^{12}$ cm^{-3}. The most obvious difference between these two discharges lies in the Ohmic input power [Figs. 4(d) and 4(h)]. In the discharge with strong reversal (more negative F), there are two EC periods (from about 11 – 12 ms and 16 – 24 ms). The Ohmic input power during these periods is punctuated by closely-spaced SDE's. The Ohmic input power in the weakly reversed discharge,

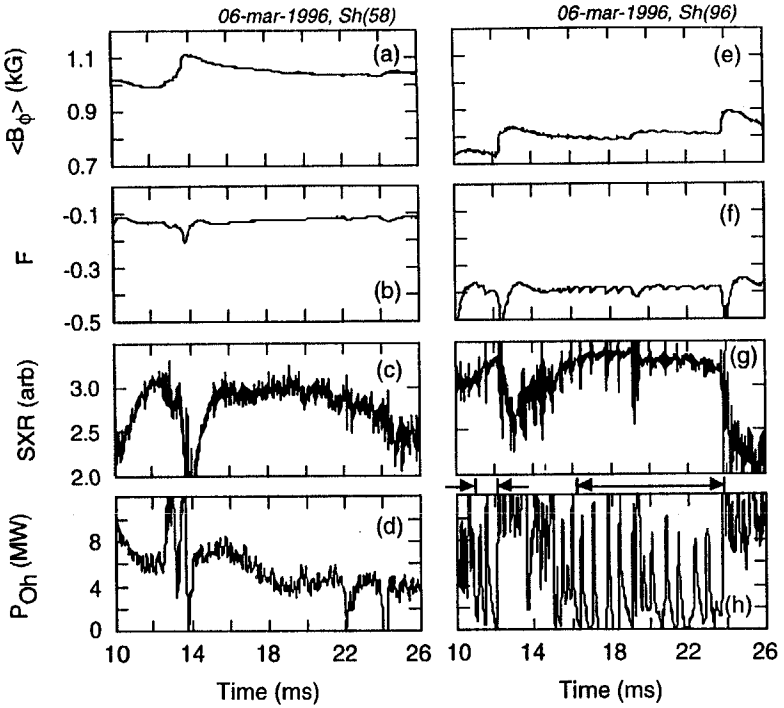

Fig. 4. Time variations of (a) cross-section-averaged toroidal magnetic field, (b) F, the reversal parameter, (c) ratio of two soft x-ray signals ∝ core electron temperature, and (d) Ohmic input power in a weakly reversed standard discharge. These same parameters are shown in (e) – (h) for a strongly reversed discharge with two periods of enhanced confinement (indicated by arrows).

on the other hand, varies smoothly (between sawtooth crashes).

Even with the relatively frequent SDE's, the time-averaged Ohmic power in the EC discharge is lower than that for the standard discharge. For example, the average from 18 – 24 ms in the standard discharge is 4.1 MW, while the average from 17 – 23 ms in the EC discharge is 2.9 MW. From the soft x-ray emission ratio, Figs. 4(c) and 4(g), one observes that the electron temperature is slightly larger in the EC discharge. Unfortunately, the soft x-ray ratio in the higher temperature EC case is near saturation [12], thus potentially understating the central electron temperature in that discharge. Note that the confinement difference between these two discharges exists even though the sawtooth cycle times in each discharge are similar. Thus, even though crash suppression is a necessary ingredient for enhanced confinement, it is not sufficient.

The difference in central electron temperature, $T_e(0)$, between a set of weakly reversed and EC discharges was quantified with the Thomson scattering diagnostic, and the resulting data is shown in Table 2. This is a different comparison than in the previous section, which compared EC and standard phases of strongly reversed discharges.

The small difference in Ohmic input power and the relatively low EC energy confinement time is explained in part by the shot-to-shot variability in SDE spacing. The closer the spacing of these events, the higher the average Ohmic input power (and the lower the average temperature). The EC discharges in the above ensemble were not screened for small dynamo event spacing. This illustrates that, *due to variations in SDE spacing and amplitude, not all EC discharges exhibit* τ_E

Table 2. Confinement parameters during strongly reversed EC discharges and weakly reversed standard discharges.

	EC	standard
F	≤ -0.2	-0.1
I_ϕ	400 kA	400 kA
$\langle n_e \rangle$	0.9×10^{13} cm^{-3}	0.9×10^{13} cm^{-3}
$T_e(0)$	430 eV	290 eV
P_{Ohmic}	4.1 MW	4.8 MW
τ_E	2.2 ms	1.2 ms

$\geq$ *3 ms*. Averaging over all EC periods, the EC energy confinement time is almost certainly less than 3 ms.

The emergence of discrete small dynamo events, one of the hallmarks of EC discharges, is gradual as toroidal field reversal is increased. This is illustrated in Fig. 5, in which the Ohmic input power is shown for discharges that differ only in toroidal field reversal. The reversal parameter F ranges from -0.1 in Fig. 5(a) to -0.4 in Fig. 5(d). With F = -0.1, there is no hint of small dynamo events, but they emerge as reversal is strengthened. Note as well that the amplitude of these events, in the Ohmic power, increases with reversal. If SDE behavior is tied to the radial electric field gradient (Chapter 4) as one might guess, does Fig. 5 imply that the magnitude of the radial electric field gradient increases gradually with reversal, or does the gradient simply come into existence with an unchanging magnitude at a threshold level of

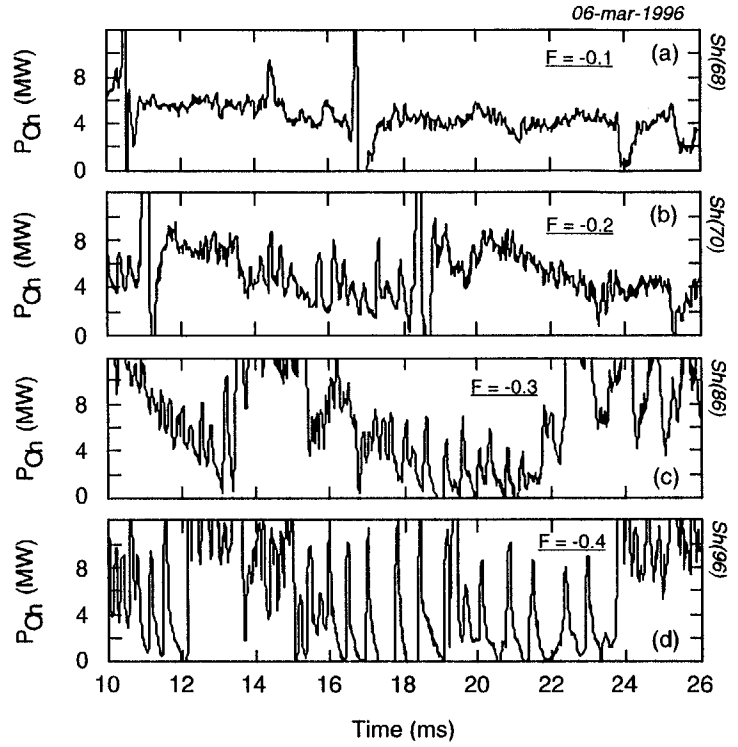

Fig. 5. Ohmic input power in 400 kA, 6×10^{12} cm^{-3} discharges with varying toroidal field reversal (a) F = -0.1, (b) F = -0.2, (c) F = -0.3, and (d) F = -0.4.

reversal? Data does not yet exist to address this issue.

That enhanced confinement is achieved with strong reversal is actually somewhat ironic. Before the advent of EC discharges, operation with strong reversal almost invariably led to more frequent and violent

sawtooth crashes, and the resulting energy confinement was generally degraded relative to that in weakly reversed discharges. To illustrate this point, compare the Ohmic input power in two discharges *without* enhanced confinement. Between sawtooth crashes, the Ohmic power in a strongly reversed discharge [Fig. 2(b)] is roughly twice that in a weakly reversed discharge [Fig. 4(d)], and the temperature is lower in the strongly reversed discharge. Thus, enhanced confinement occurs in a region of parameter space that formerly resulted in poor performance.

The density requirement for EC discharges plays a role similar to the reversal requirement. In addition to the upper density limit described in the first section, there is also a lower density limit. This lower limit is typically that beyond which all MST discharges begin to degrade. This limit has not been explored thoroughly at all plasma currents, but in 200 kA EC discharges, for example, discharge quality begins to degrade below $\langle n_e \rangle \sim 3 \times 10^{12}$ cm^{-3}.

As the upper density limit is approached from above, the emergence of EC characteristics (specifically SDE's) is gradual, very much like their emergence as toroidal field reversal is increased (Fig. 5). Further, discharges in which the density is too high for EC behavior are somewhat similar to discharges in which the reversal is too weak. This is illustrated in Fig. 6, where the Ohmic input power in two 400 kA discharges is compared. In Fig. 6(a), the reversal is sufficiently strong, but the density is too high. In Fig. 6(b), the reversal is too weak, but the density is sufficiently low. Failing to satisfy either the reversal or density requirement prevents enhanced confinement.

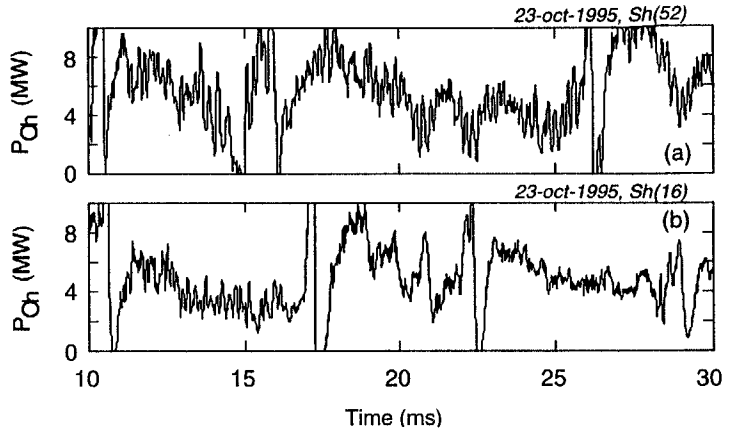

Fig. 6. Ohmic input power in a discharge with (a) $F \sim -0.23$ and $\langle n_e \rangle \sim 1.1 \times 10^{13}$ cm^{-3} and (b) $F \sim -0.13$ and $\langle n_e \rangle \sim 6 \times 10^{12}$ cm^{-3}.

3.3 Impurity influx

Impurity influx can prevent EC and PPCD discharges. This is implied by these discharges' dependence on wall conditioning and control of field errors, a lack of which leads to increased impurity influx. Unless they become completely ionized, impurity ions provide a continuous channel for power loss through (line) radiation, which cools the plasma. As discussed in Chapter 2, there is an edge temperature threshold for triggering an H-mode (i.e., strong $\mathbf{E} \times \mathbf{B}$ flow shear), and it is possible that EC and PPCD discharges have a similar dependence. By decreasing the electron temperature and increasing the Ohmic input power $\propto Z_{eff} T_e^{-3/2}$ (where Z_{eff} is the mean ionic charge), any impurity

influx can also degrade the energy confinement of established EC and PPCD discharges. In this section, I will first summarize the mechanisms for impurity influx in the MST. Then, I will describe some measurements and experiments revealing the adverse effect of impurities.

3.3.0 Mechanisms for impurity influx

The primary source of impurities in the MST is the plasma-facing wall. Roughly 90% of the plasma-facing surface of the MST's aluminum vacuum vessel is unshielded. The remaining 10% is covered by many centimeter-thick graphite and ceramic tiles. These tiles (or limiters) minimize direct contact between the plasma and the bare aluminum. References to "the wall," include both the bare aluminum and the tiles. The dominant impurities in the MST are boron, carbon, nitrogen, oxygen, and aluminum, and erosion of the wall causes their injection into the plasma.

There are at least three mechanisms by which impurities can be injected into the MST plasma. One is sputtering, where energetic ions and neutrals strike the wall and cause the ejection of wall materials [13]. Sputtering can occur anywhere on the wall, and it can be particularly intense with a large magnetic field error or a sawtooth crash, both of which lead to a larger-than-normal particle flux to the wall. Another mechanism, thermal evaporation, occurs if the particle and radiation flux heats the wall to the point of melting and boiling, or even sublimation [13]. This may occur with very localized heating due, e.g, to a magnetic field error.

Yet another source of impurities is unipolar arcing, where the wall acts as both the cathode and anode for a tiny arc of electron current [13,14,15]. In this case, impurities are injected due to melting and boiling at the point on the wall where the arc originates. Unipolar arcing can occur anywhere on the wall, but it is most probable at the MST's insulated voltage gaps [16]. For EC and PPCD discharges, the toroidal gap (horizontal cut in the shell) is most problematic due to the (surface poloidal) voltage that appears across it during sawtooth crashes, small dynamo events, and each PPCD pulse. This voltage causes one side of the gap to acquire a more positive potential and the other side a more negative potential, both with respect to the edge plasma. The side with the negative potential, the cathode side, is then more likely to exhibit unipolar arcing.

3.3.1 An example of the impact of unipolar arcing

An important lesson regarding the role of unipolar arcing was learned after MST operation was halted from June 1993 to July 1994 for installation of a new toroidal field (B_ϕ) transformer. Prior to this shutdown, EC and PPCD discharges of good quality had been achieved. However, attempts to revive these discharges after the shutdown failed for about one year. One reason for the failure to reachieve EC discharges was that some of the operational requirements (fueling and reversal) were not actually known in 1993, but it so happened that they were automatically (and fortuitously) satisfied by the standard mode of operation at that time. The standard mode of operation was different after the shutdown.

Another possible reason for the failure to immediately reachieve quality EC and PPCD discharges was tied to the direction of B_ϕ. The direction of B_ϕ following the shutdown was reversed relative to its direction before the shutdown, and this had several consequences. Unipolar arcs propogate (one after another) across a surface in a single direction determined by $\mathbf{J} \times \mathbf{B}$ (where $\mathbf{J}$ is the arc current density) [14]. By inducing unipolar arcing with many similar plasmas, arcing on a given surface can be minimized (but not eliminated) [13]. This is due in part to the elimination of slight protrusions of surface material which are highly susceptible to arcing. Prior to the shutdown, the direction of B_ϕ had remained unchanged for several years, and the wall was probably conditioned to minimize arcing, but this conditioning may have been negated following the shutdown, due in part to the new direction of the edge magnetic field leading to a new direction for arc propogation.

One obvious candidate region for fresh arcing was the toroidal gap, as the cathode side of this gap was formerly the anode side. Fresh arcing might also have been occurring near the poloidal gap (vertical cut in the shell), due to the new direction of arc propogation. A copious amount of aluminum was eroded and redeposited in RFP discharges following the shutdown, and this could easily have been due to fresh unipolar arcing. One other potentially detrimental result of the new B_ϕ direction was that fast (energetic) electrons [17] were now propogating in a new direction in the edge. These electrons can inflict damage by melting, and they were now striking previously untouched surfaces.

In May of 1995, B_ϕ was switched back to its pre-shutdown

direction. For comparison, discharges were run on the same day before and after the switch. The Ohmic input power ($\propto Z_{eff}T_e^{-3/2}$) decreased ~ 25% following the switch, and within a few weeks, high quality EC and PPCD discharges were reestablished. Note that if unipolar arcing was the primary mechanism for impurity influx in this case, this implies that the pre-shutdown arc conditioning was not affected by the approximately one year of post-shutdown operation.

3.3.2 The impact of field errors

Magnetic field errors are largest and most problematic at the poloidal gap [8]. By causing locally increased transport and shifting of the plasma column into the wall, field errors can lead to intense plasma-wall interaction and impurity influx. The MST has several systems for correction of field errors at the poloidal gap. One consists of eight internal correction coils driven in series with the primary winding of the poloidal field circuit. This system is designed to correct for errors of various poloidal mode numbers. Another system, driven by its own capacitor bank, provides a compensating m = 1 vertical field offset, which affects the horizontal position of the plasma column.

The importance of the coils driven in series with the primary winding was made clear in a set of 500 kA discharges. With the coils active, EC discharges were plentiful, but when the coils were disabled (keeping all else fixed), the impurity level (indicated by C IV) increased by a factor of two, and few EC discharges were achieved. Internal sensing coils showed that the average radial error field (normalized to the poloidal field at the edge) was 1 - 2% with the correction coils active

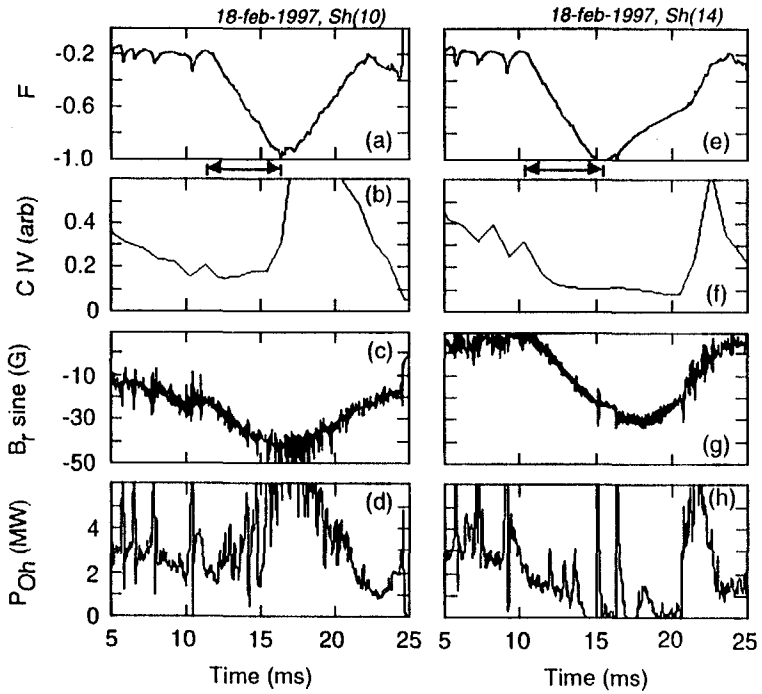

Fig. 7. Time variations of (a) the reversal parameter, (b) C IV (154.9 nm) radiation, (c) vertical component of the m=1 radial field at the poloidal gap, and (d) Ohmic input power in a discharge with PPCD (indicated by arrows) but without m=1offset correction. These same parameters are shown in (e) - (h) for a discharge with PPCD and m=1 correction.

and 7 – 8% with the coils disabled [18].

The need for the m = 1 vertical field system was apparent during experiments with PPCD, and the results described below are also relevant to EC discharges with very strong toroidal field reversal (F ≤

-0.5). Two discharges with PPCD are shown in Fig. 7. For reference, PPCD in the discharge on the left begins at ~ 11.5 ms and ends at ~ 16 ms. With the correction system disabled, the vertical component of the radial field [Fig. 7(c)] is fairly large before PPCD and becomes larger with PPCD. Thus, instead of improving the discharge, PPCD degrades it, as illustrated by Figs. 7(b) and 7(d). With the correction system enabled, the magnitude of the error field is not as large during PPCD. However, the error at the end of the PPCD pulse is not insubstantial, differing from the uncorrected case by only about 10 G. Thus, it may be the field error amplitude during the initial phase of PPCD that matters as far as the quality of the PPCD phase is concerned. In other words, field error control may be needed primarily to allow PPCD to trigger a phase of enhanced confinement. Then, once PPCD is established, the plasma may be less sensitive to error fields, due to the overall reduction of particle and energy flux to the wall.

Field errors at the gap may have played a significant role in the discharges shown in Fig. 2. Figure 8 contains the Ohmic input power and vertical component of the m = 1 error field for these two discharges. In the brief periods of enhanced confinement around 10 ms in each discharge, the error field decreases toward zero. The sawtooth crash that ends each period then increases the error field (indicated by arrows for each discharge). The error in shot 87 increases to about 40 G, and the discharge subsequently degrades to standard confinement with a steadily increasing field error. The error in shot 26, however, increases to only about 20 G, and the discharge enters a long period of enhanced confinement with a modest field error throughout. The larger

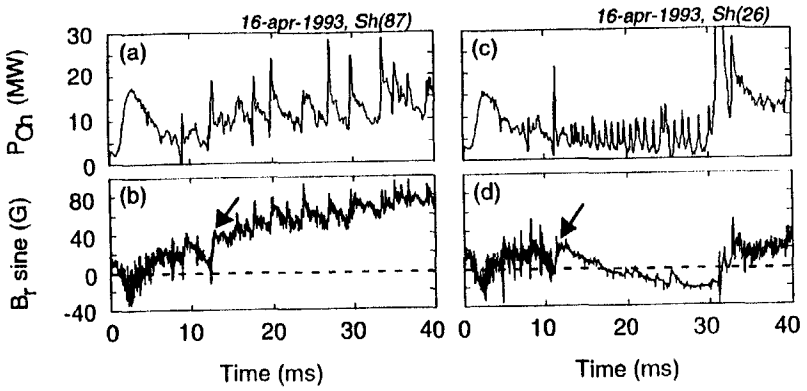

Fig. 8. Ohmic input power and vertical component of the m=1 radial magnetic field at the poloidal gap in (a) - (b) a discharge with a long period of standard confinement and (c) - (d) a discharge with a long period of enhanced confinement. These are the same discharges as in Fig. 2. The arrows indicate the end of the brief periods of enhanced confinement exhibited by each discharge.

crash-induced field error in shot 87, and the impurity influx that was the likely result, may be part of the reason that this discharge degraded to standard confinement. EC discharges are not yet achievable with good shot-to-shot reproducibility, and uncorrected field errors such as that in shot 87 may be one cause.

3.4 Wall conditioning

Wall conditioning is accomplished primarily by pulsed discharge cleaning with helium and solid-target boronization [6]. These techniques are critical to the achievement of high quality EC and PPCD discharges.

3.4.0 Pulsed discharge cleaning

Most fusion plasma devices employ some variation of glow or pulsed discharge cleaning using hydrogen or helium. A good review of these and other techniques is found in Ref. 7. Hydrogen has proven useful in devices with contaminated metal surfaces. Atomic hydrogen has a high chemical reactivity, and it combines with many impurity species, including oxygen, to form volatile substances that are desorbed (released from the contaminated surface) and pumped out [13]. Desorption of these compounds occurs thermally, if the contaminated surface is hot enough, and it can also occur due to the impact of energetic particles.

For devices in which a large fraction of the plasma-facing wall is covered with graphite, helium is preferred over hydrogen. The primary reason is that, unlike helium, large quantities of hydrogen can be trapped in the surface region of the graphite. The random desorption of this hydrogen during normal (RFP, tokamak, etc.) discharges can hamper control of the plasma density. Unlike hydrogen, helium does not combine chemically with other elements. Contaminants are released from the wall by the impact of the energetic helium ions.

Ten percent of the plasma-facing wall in the MST is covered with graphite (and some ceramic), while the rest is bare aluminum. Thus, it is not obvious *a priori* which gas is optimum. The MST's pulsed discharge cleaning (PDC) system was employed in a test of both hydrogen and helium under a variety of circumstances, including discharges with both low and high temperature and density. In one series of tests, a mix of 80% hydrogen and 20% helium was applied

based on the hypothesis that a combination of these gases would best suit the MST. Another series of tests involved only hydrogen, while another involved only helium. The performance of the gas mix and the individual gases was evaluated based on impurity levels before, during, and after a series of PDC discharges. These levels were monitored with a variety of spectroscopic diagnostics, as well as a residual gas analyzer.

These tests indicated that PDC in 100 kA (the maximum available PDC plasma current) helium discharges gave the best overall results. However, there was still some uncertainty as to the optimum fill pressure or density, which for a fixed plasma current also determines the plasma temperature. Thus, in 100 kA discharges, the Thomson scattering diagnostic was used to measure the central electron temperature, and a Langmuir probe was used to measure the edge temperature and density. In these discharges, only the operational pressure, measured with an ionization guage [19], was varied.

The central and edge electron temperature in PDC is shown in Fig. 9(a), while the edge density is shown in Fig. 9(b). If the central helium ion temperature is near the central electron temperature, then the potential for sputtering exists during PDC. For PDC to be useful, it should desorb impurity particles while minimizing sputtering. Thus, it was concluded that PDC at higher pressure was preferred. There is only a single helium puff valve available for PDC, and with all vacuum pumps open to the MST, the maximum achievable pressure is 0.8 mTorr. Higher pressures, like the 1.1 mTorr data point in Fig. 9, are achieved either by reducing the speed of the pumps or by valving some of them off, but this reduces the rate at which liberated impurity

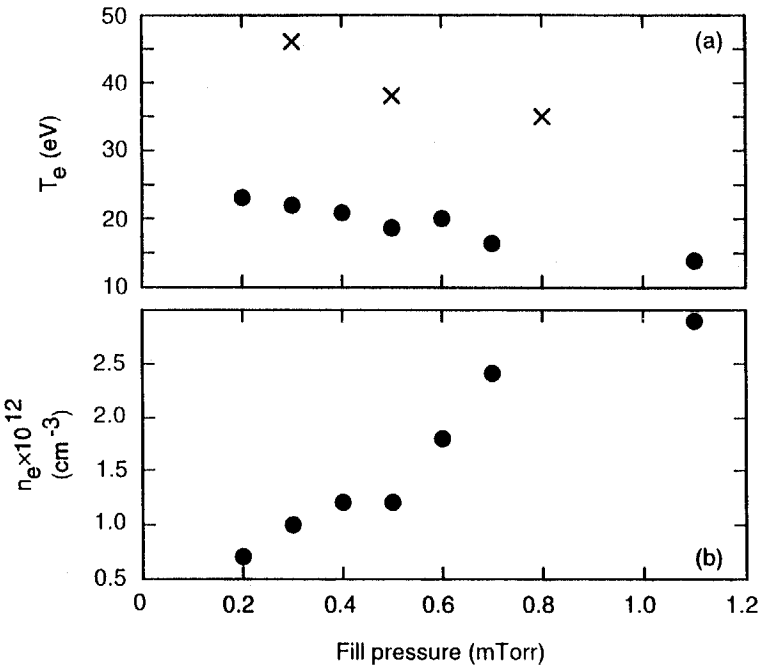

Fig. 9. Variations with fill pressure of (a) central (x) and edge (•) electron temperature and (b) edge density in 100 kA helium PDC discharges.

particles are pumped out. Thus, 0.8 mTorr was chosen as the optimum PDC pressure.

The superiority of helium over hydrogen in the MST was further verified following the previously mentioned shutdown for replacement of the B_ϕ transformer. Following the shutdown, only hydrogen was initially available for PDC, and the resultant RFP discharges were far

from ideal. Later, helium became available, and RFP discharge quality showed immediate improvement.

It must be noted that, in addition to PDC, RFP operation at high plasma current is also important for wall conditioning. The RFP repetition rate is small (one discharge every 2 – 3 minutes) compared to the rate for PDC (one discharge every 5 seconds), but the total energy reaching the wall is substantially larger in each RFP discharge, causing the liberation of more contaminants. Following events such as an up-to-air, RFP discharges are essential for reconditioning the wall.

3.4.1 Boronization

Boronization is the application of boron, usually in combination with one or more additional low Z (atomic number) elements, to the plasma-facing wall. Boronization serves many purposes. First, the coating it provides partially protects the wall from plasma bombardment, thus minimizing impurity injection. Further, when erosion does occur, elements of the low Z coating material instead of the higher-Z wall material are injected into the plasma, thus minimizing increases in radiation power loss and plasma resistivity. Boron is also an oxygen "getter," meaning that it binds with and traps oxygen coming into contact with it. The coating may also fill in around slight protrusions of wall material which would otherwise be likely sites for unipolar arcing [14].

Boronization in the MST is done using the solid-target technique [6], where a solid boron-containing compound serves as the source of boron. Boron carbide (B_4C) is the compound of choice for the MST.

Boronization is normally done in standard helium PDC discharges, but it has also been tried during hydrogen PDC and even RFP discharges. In all cases, a rod of B_4C is inserted into and eroded by the plasma, and to enhance erosion, the rod is biased. Positive bias attracts electrons, and ablation of the rod can occur, in principle, due to the electron energy deposited on the rod surface. Negative bias attracts ions, which cause erosion of the rod by processes such as sputtering and spallation.

Boronization with a biased rod was first carried out successfully with negative bias, but erosion of the rod in this polarity can be fairly uneven, with one side of the rod often remaining untouched. It was hoped that positive bias would lead to more uniform erosion. However, while a large electron current could be drawn with this polarity, no significant erosion of the rod ever occurred.

Boronization often involved rods at different toroidal locations, one of which was the poloidal gap. It was found that boronization at the gap led to more frequent and higher quality EC periods than boronization at other locations, and this is not unexpected, since plasma-wall interaction is probably most severe at this location in most discharges.

There were a few other findings regarding boronization with negative bias. First, there is a pressure (density) window, 0.3 – 1.7 mTorr, in which helium PDC must be run for any erosion of the rods to occur. Second, it was observed that current will cease to flow through a rod and erosion stops after the rod resides in one orientation for several PDC sessions. Apparently, this has something to do with the one-sided erosion of the rod, as a simple rotation of the rod about its axis by, e.g.,

180 degrees, can reliably revive it. A third and unfortunate side effect of negative-bias boronization is that small chunks or crumbs can be ejected from the rod into the plasma. These crumbs are not always vaporized in the plasma, and they sometimes work their way onto O-ring surfaces in vacuum isolation valves. This has led to valve failure and vacuum accidents, sometimes making this mode of boronization a nuisance. It is hoped that positive-bias boronization will ultimately work with higher bias voltages than have yet been available, thereby avoiding such debris.

3.5 Fueling

Fueling with little or no gas puffing has helped to maximize the quality of EC and PPCD discharges. Here, gas puffing is replaced by wall fueling, where fuel is provided by the plasma-facing wall. Wall fueling alone has been used to sustain the plasma density for periods up to 30 ms. The EC and PPCD requirement for careful wall conditioning suggests the possibility that the edge temperature plays some role. In particular, the presence of a strongly sheared, H-mode-like $\mathbf{E} \times \mathbf{B}$ flow in these discharges suggests that there may be a temperature threshold involved (see the H-mode discussion in Chapter 2).

In this context, there are several potential advantages of wall fueling over puff valve fueling, some of which I take from Ref. 13. Wall fuel is comprised both of recycled fuel and preloaded fuel. Recycled fuel is simply fuel particles in a given discharge that collide with and are immediately backscattered from the wall. Preloaded fuel is comprised of fuel particles that were adsorbed by the wall earlier in a

given discharge or in a previous discharge. Backscattered particles are typically reflected from the wall with roughly half of their incident energy, which can be substantial, and particles released from the wall after being adsorbed have energies of a few eV. The fuel particles from puff valves, on the other hand, are at room temperature. In addition to this temperature difference, a significant fraction of wall fuel particles enter or reenter the discharge already ionized, while puffed fuel is entirely neutral. Thus, through collisional equilibration and radiation, puffed fuel can cool the edge plasma significantly more than wall fuel.

Some attempts have been made to quantify the effects of wall versus puffed fueling. For instance, the electron temperature in the extreme edge (in the shadow of the limiters) was measured with a Langmuir probe. For a fixed central line-averaged density, the temperature with puffed fuel was lower than that with wall fuel by ~ 20%. However, there was no reliable means of measuring the temperature in the region 5 - 10 cm from the plasma edge, where the radial electric field gradient forms (Chapter 4). Thus, the only recourse was to observe the impact of puffing on EC discharges. It was found that, for the same line-averaged density, the frequency and quality of EC periods was lower for puffed fueling than it was for wall fueling. However, a low level of puffing combined with wall fueling was tolerable. As with EC discharges, use of wall fuel has coincided with the achievement of the highest quality PPCD discharges, but a detailed comparison of wall versus puffed fueling with PPCD has not been made.

Given the need for wall fueling and the fact that recycling is not always sufficient on its own, various techniques for preloading the wall

were explored. In one test, the MST pressure was sustained in the mTorr range for several seconds by multiple gas puffs and then allowed to return to its base level, all before an RFP discharge. However, it was found that the wall could not sustain the plasma density, i.e., fuel had not been adsorbed by the wall. It was then guessed, and later confirmed in the literature [20], that significant wall loading would only occur in the presence of a plasma.

Hydrogen PDC was used to test this hypothesis. It was run both overnight and for short (5 – 45 minute) sessions between RFP discharges. It was also run with boronization, with the idea that the boron–carbon coating might maximize hydrogen trapping on the wall. Hydrogen PDC was successful in loading the wall, but this loaded fuel was soon depleted, regardless of the length of the PDC session. Without puffing, the density could only be sustained in the first two or three RFP discharges following PDC. After that, the achievable density became too low, and PDC would have to be run again (a time consuming process).

The next and most successful technique tried was to load the wall in a given RFP discharge to provide fuel for the next RFP discharge. The latter half of a typical 60 ms RFP discharge, during which the plasma current is ramping down, is generally not needed for data collection. Thus, this portion of the discharge can be sacrificed for wall loading, and puffing and the density in this phase can be increased as much as necessary. The wall can then be sufficiently loaded such that no puffing is necessary for at least the first 30 ms of the next discharge. This technique allows automatic wall loading (no time consuming PDC is needed). Further, by monitoring the shot–to–shot history of the line–

averaged density, the density can be kept fairly constant over the course of a run day.

To reproducibly achieve a target density in the first half of a discharge, the line–averaged density integrated over time in a given shot is a good indicator of what the density will do in the next shot. One simply observes the area under the (line–averaged) density curve. If this area in a given shot is larger than in the previous shot, the density in the subsequent shot will almost certainly be larger (with no change in puffing).

When starting RFP discharges following a night of helium PDC, the walls are not loaded, so puffing is required throughout the first and possibly the second discharges. Then, puffing can be turned off for the desired time window (0 – 30 ms, 10 – 20 ms, etc.). To compensate for this decrease, puffing outside this time window has to be increased. Arriving at the target density then requires a few more shots. If the density initially overshoots the target, puffing can be decreased. The density may then undershoot, requiring an increase in puffing. By making smaller and smaller adjustments (up and down), one can arrive at the target density. Once the target is reached, the line–averaged density must be monitored and any adjustments made as necessary. Note that this technique for reproducibly achieving a target density also works when puffing is used throughout the discharge. One must simply bear in mind that the density in a given shot always plays a role in determining the density for the next shot.

Any reasonable target density can be achieved reproducibly with a variety of puff valve controller settings. These settings are

determined by a number of variables, such as the desired target density, the length of each discharge, and the plasma current, all of which vary day to day. Coincidentally, this technique lends itself to "softer" discharge termination as well. When the density is larger near the end of the discharge, the plasma current will ramp down more gradually, reducing mechanical and electrical stress on the MST.

Note that the density can sometimes change unexpectedly by a substantial amount from one shot to the next with little change in puff settings. For example, a density increase can occur if particle confinement improves (e.g., due to EC or PPCD) or more intense plasma–wall interaction occurs (e.g., due to violent crashes or field errors), and this is not always controllable or predictable by the operator.

Keeping a fixed cycle time (the time between discharges) is necessary to maintain a reproducible density. The wall fuel in a given discharge is comprised of the particles on the wall surface. However, fuel particles adsorbed by the wall can diffuse below the wall surface and return to the surface at a later time. Thus, if the time between discharges is changed, more or less fuel particles will have diffused back to the surface (subject to a saturation limit). Small changes in the cycle time will not affect fueling dramatically, but if it is increased by several minutes or more, the density in the following shot will typically be larger than expected, with no change in puff settings.

There is a possible isotopic dependence to fueling. Although there is no evidence in the literature to suggest any difference between hydrogen and deuterium as far as fueling is concerned [13], there may sometimes be differences in the MST. For reasons not yet understood,

deuterium discharges are less likely to lock than hydrogen discharges, for a given set of plasma parameters. When a discharge locks, field errors at the poloidal gap grow [8], and this can lead to increased plasma–wall interaction and increased wall fueling. Also, locking can shorten discharges in an unpredictable way. Thus, when hydrogen is used and locking is prevalent, control of the density is more difficult. However, when locking is not an issue, such as at low plasma current, I have observed no isotopic dependence to fueling.

3.6 Summary

In this chapter, I have described the operational requirements for achieving high quality EC and PPCD discharges. These requirements include sufficiently strong toroidal field reversal, sufficiently low density, conditioning of the plasma–facing wall, control of field errors, and fueling without puff valves. These requirements may be based in part on the physics underlying the formation of the strongly sheared $\mathbf{E} \times \mathbf{B}$ flow (next chapter). There are certainly many parallels between the requirements for EC (and PPCD) discharges and those for H–mode discharges. When these requirements are satisfied, EC periods are achievable with an energy confinement time ≥ 3 ms, triple the normal value.

References

[1] B. E. Chapman *et al.*, Phys. Plasmas **3**, 709 (1996).

[2] J. A. Beckstead, Ph.D. thesis, University of Wisconsin, Madison, Wisconsin, 1990.

[3] S. Hokin *et al.*, Phys. Fl. B **3**, 2241 (1991).

[4] J. S. Sarff *et al.*, Phys. Rev. Lett. **78**, 62 (1997).

[5] J. S. Sarff *et al.*, Phys. Rev. Lett. **72**, 3670 (1994).

[6] D. J. Den Hartog *et al.*, J. Nucl. Mater. **200**, 177 (1993); D. J. Den Hartog and R. D. Kendrick, *ibid.* **220–222**, 631 (1995).

[7] J. Winter, Plasma Phys. Controlled Fusion **38**, 1503 (1996).

[8] A. F. Almagri *et al.*, Phys. Fl. B **4**, 4080 (1992).

[9] E. Scime *et al.*, Phys. Rev. Lett. **68**, 2165 (1992).

[10] J. C. Sprott, Phys. Fl. **31**, 2266 (1988).

[11] M. E. Rensink *et al.*, Phys. Fl. B **5**, 2165 (1993).

[12] G. A. Chartas, Ph.D thesis, University of Wisconsin, Madison, Wisconsin, 1991.

[13] G. M. McCracken and P. E. Stott, Nucl. Fusion **19**, 889 (1979).

[14] F. Schwirzke, J. Nucl. Mater. **128–129**, 609 (1984).

[15] A. E. Robson and P. C. Thonemann, Proc. Phys. Soc. **73**, 508 (1959).

[16] R. N. Dexter *et al.*, Fusion Technol. **19**, 131 (1991).

[17] M. R. Stoneking *et al.*, Phys. Rev. Lett. **73**, 549 (1994).

[18] K. Mirus (private communication).

[19] Ionization guages are typically calibrated for air. Thus, the true pressure in hydrogen and helium is obtained by multiplying the guage measured pressure by factors of ~ 2.4 and ~ 6.8, respectively.

[20] S. Sengoku *et al.*, J. Nucl. Mater. **145–147**, 556 (1987).

4. Sheared **E** × **B** flow

Both EC and PPCD discharges exhibit a strongly sheared **E** × **B** flow in the edge, and while the electric field is opposite in sign to the radial electric field in H-mode discharges, the underlying physics may be similar. In Sec. 4.0, I describe the probes and techniques used to measure the radial electric field profile and related edge quantities. Section 4.1 contains probe measured data, for both EC and PPCD discharges. In Sec. 4.2, I discuss observations suggesting a reduction of transport in the edge of these discharges. In Sec. 4.3, I describe impurity ion flow in these discharges. Section 4.4 provides a discussion of the effects on rotation of toroidal field reversal, fueling technique, fuel isotope, and wall conditioning. In Sec. 4.5, I speculate on a possible triggering mechanism for the sheared **E** × **B** flow, namely heat flux through the plasma edge. In Sec. 4.6 is a brief chapter summary.

4.0 Electrostatic probe design and technique

The probe measurements [1] discussed in this chapter were all made in discharges with a plasma current ≤ 200 kA and a line-averaged density of about 5×10^{12} cm^{-3}. This low plasma current allows insertion of the probes into the edge plasma without their immediate destruction due to heat flux. However, at this relatively low density (required for EC discharges), superthermal (fast) electrons run rampant in the plasma edge [2,3]. These energetic electrons travel parallel to the local magnetic field, primarily in one direction, and they can render electrostatic probe signals unreliable (e.g., from the sudden onset of

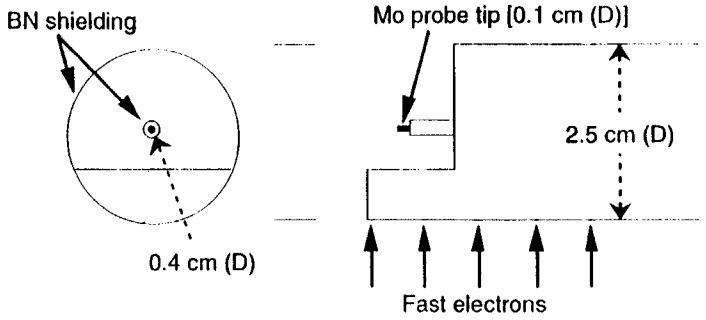

Fig. 1. Sketch of a probe with a fast electron shield. The probe consists of a molybdenum tip and boron nitride shielding. The diameters of three of the probe components are indicated.

thermionic electron emission). They can also destroy metallic probe tips in the course of a single RFP discharge. Thus, a fast electron shield was designed for the probes (see Fig. 1). The probes are oriented such that the bulk of the fast electrons strike the shield, never reaching the probe tip. The fast electrons still erode the boron nitride shielding, but the probe remains intact for several RFP sessions.

The plasma potential and radial electric field ($E_r = -\nabla V_p$) are measured using the swept probe technique [4,5], which I will briefly describe. The other electrostatic and magnetic probe measurements rely on simple, standard techniques, and I will not discuss them here. The swept probe consists of a single tip, as shown in Fig. 1. To this tip is applied a (sweeping) sinusoidal bias voltage, provided by a function generator driving a power amplifier. One half of each sinusoid generates a current-versus-voltage (I-V) curve, from which the plasma

potential can be derived. The positive and negative bias voltages must be large enough to draw electron and ion saturation currents, respectively.

A single I-V curve without the influence of fast electrons is shown in Fig. 2(a). The ×'s in this plot are the discretely sampled data points, while the solid lines are exponential and linear fits to the data. The plasma potential is taken as the point at which the two fits intersect. The power amplifier is limited to and operated at a sweeping frequency of 250 kHz, so each I-V curve spans 2 μs (4 μs for a complete sinusoid). The swept probe digitizer is clocked at 50 MHz, but it has only 32k of memory. Thus, one can only acquire about 0.6 ms of data per discharge.

The fast electron shield was initially designed for the swept probe, as I-V curves without the shield often exhibit *two* distinct exponential regions, preventing accurate determination of the plasma potential. An example of such a curve is shown in Fig. 2(b). The additional exponential reflects the presence of the fast electrons [5], which are characterized by a drifted Maxwellian with a temperature substantially larger than that of the bulk electrons [3]. As stated above, fast electrons travel primarily in one direction parallel to magnetic field lines. There is, however, a nonzero population of fast electrons traveling in the other (anti-parallel) direction [3], and these electrons are not blocked by the shield. Therefore, even with the shield in place, some I-V curves exhibit the double exponential feature. Such curves are not included in the plasma potential ensemble average. Another problem sometimes encountered with the swept probe (in EC and PPCD discharges) is that the probe is unable to draw the very large electron saturation current

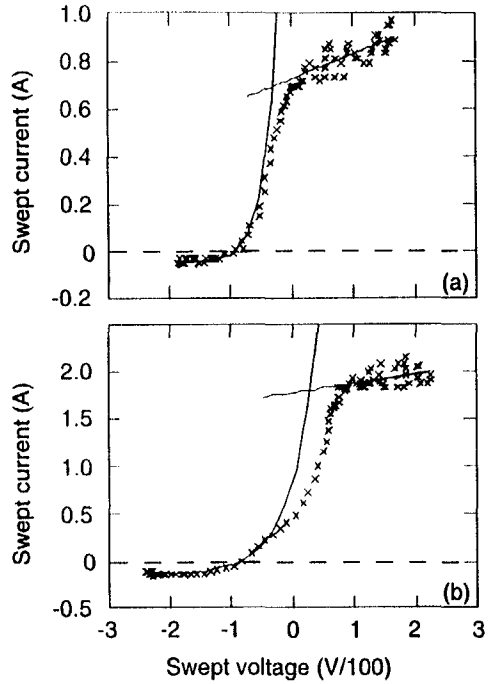

Fig. 2. I-V curves from the swept Langmuir probe (a) without and (b) with the effect of fast electrons. Fast electrons cause a double exponential. The plasma potential is determined by the intersection of the exponential and linear fits. I-V curves as in (b) are not included in the plasma potential ensemble average.

often associated with the region of strong shear. Thus, no linear region (in the upper right portion of the curve) exists with which to determine the plasma potential. This will be discussed further in the next section.

Each data point in the radial profiles (of the plasma potential,

floating potential, etc.) shown below is an ensemble average of time-averaged data from 10 – 30 similar discharges. Error bars, when included, are purely statistical in nature and represent the variation within each ensemble average [6]. The uncertainty associated with the determination of V_p from the I–V curve is not included in the error bars, but it is estimated to be about 5%. The time windows for all quantities except the plasma potential vary in length to match the varying length of EC and PPCD periods, and all time windows are chosen to avoid sawtooth crashes. Radial profiles of electrostatic quantities such as the floating potential were compared with and without the fast electron shield, and while the magnitude of each radial point did exhibit some dependence on the shield's presence, the shape of the profiles did not [e.g., the profiles in EC discharges exhibited flow shear (next section) with and without the shield].

All probe measurements shown in this chapter were made from vertical ports. This minimizes the effects on profile data of the outboard shift of the plasma column between sawtooth crashes. That this shifting causes significant poloidal asymmetry in edge-measured quantities was verified with the MST's so-called operational Langmuir probe [7]. Data from this probe were compared in similar discharges with the probe inserted 1 cm from the wall (the limiter-plasma boundary) at an inboard location, 45 degrees from vertical, and an outboard location, 75 degrees from vertical. The density and temperature, for example, at the outboard location were 2 – 3 times larger than at the inboard location. Thus, for a given radial insertion relative to the vacuum vessel wall, probes on the outboard side are

effectively deeper inside the plasma than probes on the inboard side. Mounting probes on vertical ports reduces the effect of this poloidal asymmetry.

4.1 Radial electric field gradients in EC and PPCD discharges

In this section, I discuss the radial electric field (E_r) profiles in EC, PPCD, and standard discharges. The gradients in E_r evident during EC and PPCD discharges are absent in standard discharges. Based on the radial electric field and edge magnetic field profiles, one finds that EC and PPCD discharges are well into the strong ($\mathbf{E} \times \mathbf{B}$ flow) shear regime, first discussed in Chapter 2. The time dependence of the shear is also discussed, based on measurements of the floating potential profile (related to the plasma potential). These measurements reveal that the flow shear forms more than 1 ms before floating potential (electrostatic) fluctuations are reduced.

The radial electric field and its gradient are relatively small in standard discharges, but both become large in a narrow region in the edge of EC discharges. The profiles of E_r and V_p are shown in Fig. 3 for both cases. Also shown is the floating potential (V_f) profile. Both sets of discharges in Fig. 3 have the same plasma current and line-averaged density, but the EC discharges are strongly reversed ($F \sim -0.5$), while the standard discharges are weakly reversed ($F \sim -0.2$).

The positive-going jump in V_p (and V_f) in the EC case translates to a locally large, positive E_r and a region of large E_r gradients at least 2 cm wide. The strong gradients in the EC case emerge with only a local change in the plasma potential. The plasma potential and radial electric

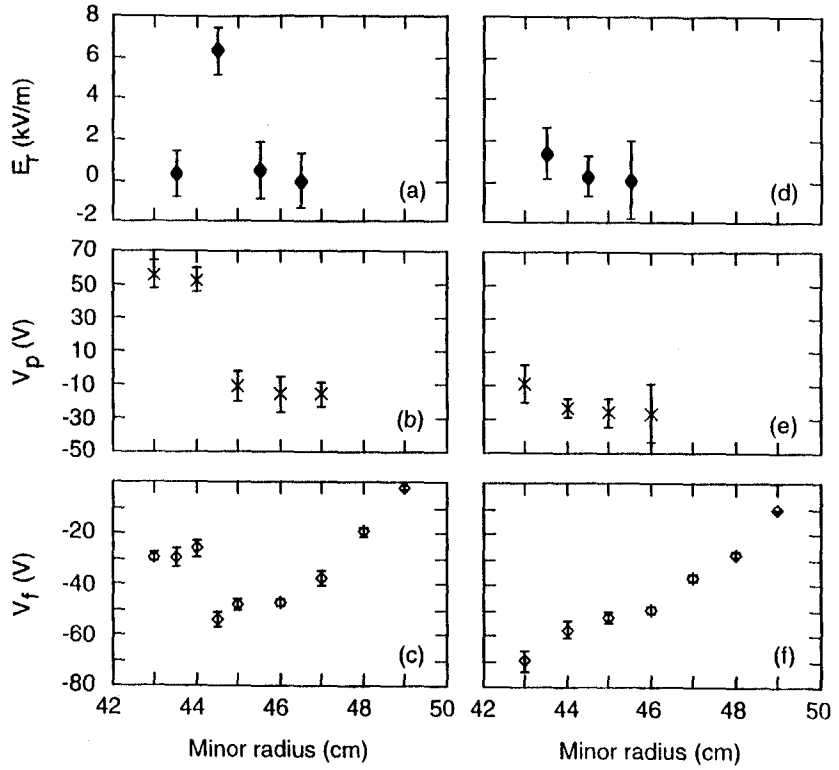

Fig. 3. Radial profiles of (a) radial electric field, (b) plasma potential, (c) floating potential in enhanced confinement (EC) discharges. These profiles are plotted in (d) - (f) for standard (weakly reversed) discharges. The plasma edge is at roughly 51 cm.

field do not change significantly outside the shear region. The floating potential and plasma potential are related by $V_f = V_p - \alpha T_e$, where α is a constant, and T_e is the electron temperature. Thus, for an expected $T_e(r)$, decreasing with minor radius, the positive jump in V_f is consistent

with the jump in V_p. In other words, if there were no increase in V_p, T_e would make V_f steadily more negative with decreasing radius. This is the case for standard discharges [Fig. 3(f)].

The positive (pointing outward) E_r in the strong shear region is in contrast to the negative E_r typical of the H-mode shear region in tokamaks and other devices [8]. This implies that, in EC discharges, one or both flow terms in the radial force balance equation,

$$E_r = \nabla P_i(n_i Z_i e)^{-1} - (\mathbf{V}_i \times \mathbf{B})_r = \nabla P_i(n_i Z_i e)^{-1} - V_\theta B_\phi + V_\phi B_\theta, \qquad (1)$$

must be significant in order to compensate for the negative contribution made to E_r by the pressure gradient (the terms in this equation were defined in Chapter 2). Figure 4 contains the profiles of the poloidal and toroidal magnetic fields, B_θ and B_ϕ, measured with probe-mounted magnetic sensing coils in the edge of (strongly reversed) EC discharges. Since $B_\theta \approx 10B_\phi$ in the region of large E_r gradients, it is likely that $|V_\theta B_\phi| << |V_\phi B_\theta|$. None of the terms in Eq. (1) have been measured, but assuming no pressure gradient and negligible poloidal rotation, one can estimate a lower bound on the toroidal rotation at the point of maximum E_r: $V_\phi > E_r/B_\theta \approx 65$ km/s.

One can extrapolate $B_\phi(r)$ in Fig. 4 to find the reversal radius (where $B_\phi = 0$). It is located at about 38.5 cm, or 13.5 cm from the wall. Thus, the E_r gradient region is roughly 5 – 6 cm beyond the reversal radius. The location of the reversal radius may be important to plasma rotation and the strongly sheared $\mathbf{E} \times \mathbf{B}$ flow, as will be discussed later in this chapter.

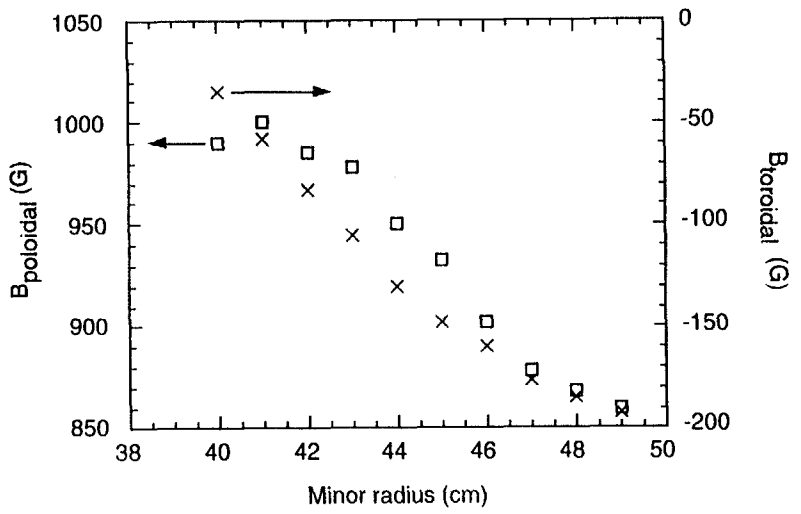

Fig. 4. Profiles of the poloidal and toroidal magnetic fields in 200 kA, F = -0.5 discharges.

To determine if fluctuation reduction is possible due to this E_r gradient, one must first calculate the $\mathbf{E} \times \mathbf{B}$ shearing rate (discussed in Chapter 2), an expression for which in toroidal geometry is given by Burrell [9]:

$$\omega_s = (RB_\theta)^2/B \times (\partial/\partial\Psi)E_r/RB_\theta \approx (1/B)\partial E_r/\partial r. \qquad (2)$$

Here, R is the major radius, B is the total magnetic field, and Ψ is the radial magnetic flux coordinate. In this geometry, $|\nabla\Psi| = RB_\theta$ [10]. For EC discharges, $\omega_s \sim 7 \times 10^6$/s. Shear in the $\mathbf{E} \times \mathbf{B}$ flow is considered

strong if ω_s is larger than the decorrelation rate of the ambient turbulence in the absence of $\mathbf{E} \times \mathbf{B}$ shear, $\Delta\omega_t$ [9,10,11]. Roughly speaking, when this criterion is satisfied, reduction of fluctuations can occur. Taking a result from Chapter 6, $\Delta\omega_t \sim 3 \times 10^5$/s. Thus, EC discharges are well within the strong shear regime, and reduction of turbulent fluctuations can occur. Of course, the shearing rate in standard discharges is much smaller than in EC discharges.

Even though EC discharges are in the strong flow shear regime, one must verify that the $\mathbf{E} \times \mathbf{B}$ shear does not drive the Kelvin–Helmholtz instability (discussed in Chapter 2). In typical magnetic fusion plasmas, magnetic shear is sufficient to prevent this instability, according to the criterion (in cgs units) [9,11],

$$\nabla E_r/E_r < (\eta \Delta\omega_t)^{-1/4}(V_A k_y/L_s c)^{1/2}, \qquad (2)$$

where η is the plasma resistivity, V_A is the Alfvén velocity, k_y is the perpendicular wave number of the mode (fluctuation) in question, L_s is the magnetic shear length, and c is the speed of light. Estimating the resistivity and choosing $k_y = n/R > (6/150)$ cm^{-1}, this criterion is easily satisfied. Therefore, EC discharges are Kelvin–Helmholtz stable.

We are as yet unable to measure the time dependence of the radial electric field profile. However, we are able to measure the time dependence of the floating potential profile, which has already been shown [Fig. 3(c)] to reflect the radial electric field gradient. The measurement is made with a so–called rake probe. The rake probe consists of six tips, spaced 1 cm apart in the radial direction. The probe

is inserted such that the tips are parallel to the local magnetic field but pointing away from the bulk of the fast electrons. The probe body consists of boron nitride and serves as a fast electron shield.

Rake probe data during an EC discharge is shown in Fig. 5. Note that this discharge has F ~ –0.75, a stronger reversal than usual. Figure 5(c) shows the time evolution of the floating potential 11 cm from the wall. Figures 5(d) – 5(f) show time–averaged profiles of V_f for different time windows. From 14 – 15 ms, there is a brief EC period, punctuated by discrete small dynamo events. These events can be seen in the Ohmic input power, Fig. 5(a), and in the radiation from deuterium neutrals, Fig. 5(b). Just after 15 ms is a sawtooth crash. Following this is another longer EC period, but the SDE amplitude in this period is reduced. This reduction is apparently linked to increased plasma–probe interaction (impurity influx), the implications of which I will discuss in the next section. Despite some differences in the details of the EC floating potential profiles in Figs. 3 and 5, the profiles still reflect the large E_r gradient. The differences may be due in part to the simultaneous (rake probe, Fig. 5) versus point–by–point (single–tipped probe, Fig. 3) reconstruction of the profile, or it could be due to actual differences between the two sets of discharges.

Following the sawtooth crash after 15 ms is a transition phase, during which the floating potential fluctuations are large [Fig. 5(c)]. The fluctuations (at 41 cm) drop off substantially just after 18 ms, and a similar reduction is observed at each radial point out to 46 cm (the locations covered by the rake probe). Roughly 1 ms *before* this fluctuation reduction occurs, the floating potential profile assumes the

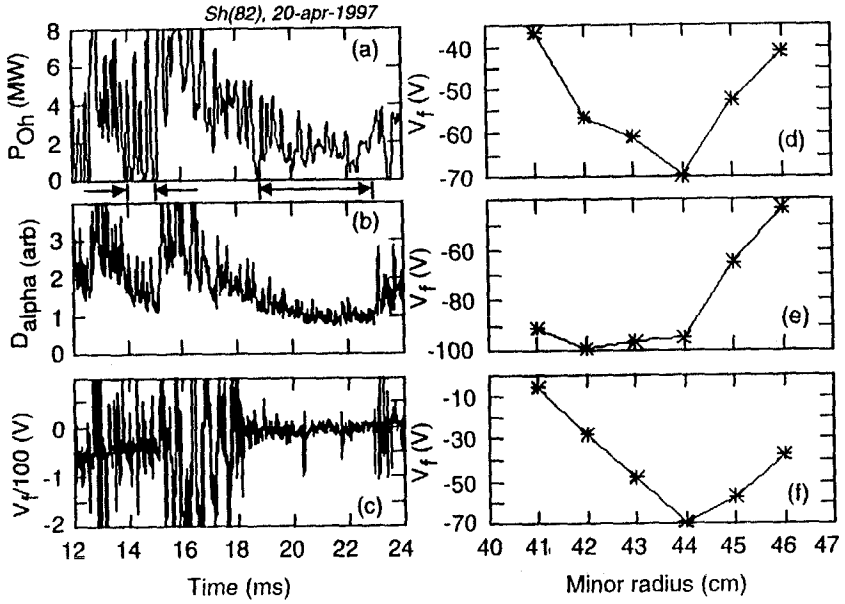

Fig. 5. Time variations of (a) Ohmic input power, (b) neutral deuterium radiation, and (c) floating potential at 41 cm minor radius. Time averaged profiles of the floating potential from (d) 14 - 15 ms, (e) 15.5 - 16.5 ms, and (f) 18.5 - 22.5 ms. The two EC periods are indicated by arrows. This noisy data is intentionally left unsmoothed to emphasize the reduction of fluctuations that occurs in the second EC period.

(strong-shear-like) shape illustrated in Fig. 5(f), thus implying that the $\mathbf{E} \times \mathbf{B}$ flow shear develops *before* the fluctuations are reduced, as one would anticipate. However, one might expect the reduction of fluctuations to occur sooner after the (re)formation of the $\mathbf{E} \times \mathbf{B}$ flow shear region, perhaps on a microsecond "fluctuation timescale." That the reduction is slower may be due to (1) a *gradual* increase in the

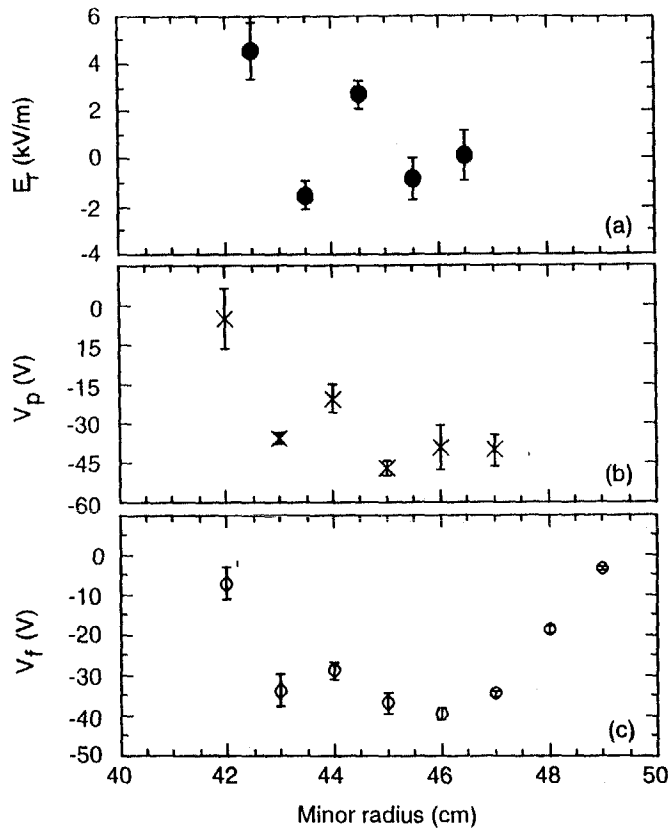

Fig. 6. Radial profiles of (a) radial electric field, (b) plasma potential, and (c) floating potential averaged over 10 - 20 PPCD discharges. The plasma edge is at roughly 51 cm. The plasma and floating potential profiles were measured many weeks apart and under different plasma conditions. Thus, they should not be compared quantitatively, e.g., to calculate a temperature profile.

magnitude of the $\mathbf{E} \times \mathbf{B}$ flow shear, not reflected by $V_f = V_p - \alpha T_e$ (as V_p and T_e may evolve together) or (2) slower evolution of, e.g., the pressure gradient, which may drive fluctuations.

In PPCD discharges, the $\mathbf{E} \times \mathbf{B}$ flow is also strongly sheared. The PPCD profiles of E_r, V_p, V_f are shown in Fig. 6. PPCD drives strong reversal, and F in the discharges used to generate Fig. 6 typically reached ~ −0.9. Thus, the standard, weakly reversed profiles in Fig. 3 are useful for comparison against the PPCD profiles. Compared to the EC profiles in Fig. 3, the profiles of E_r, V_p, and V_f during PPCD have a more complicated structure. However, were it not for the local maximum in the plasma potential at 44 cm (which also appears in the separately measured floating potential), the radial electric field profile in PPCD would have a shape similar to that in EC discharges. It is not known why the profiles in PPCD are more structured, but it may stem from the fact that, unlike EC periods, PPCD causes a continuous change to the edge plasma equilibrium.

The region of strong shear with PPCD appears to extend over several cm, but the strongest shear occurs in the region between 42 and 45 cm. As with EC discharges, comparison of the $\mathbf{E} \times \mathbf{B}$ shearing rate and the decorrelation rate of the ambient turbulence confirms that PPCD is also in the strong shear regime. Further, PPCD discharges are calculated to be Kelvin–Helmholtz stable.

The plasma potential at 42 cm [the innermost data point in Fig. 3(b)] is as yet somewhat preliminary. A problem with swept probe measurements in PPCD (and occasionally EC) discharges is that the density and temperature in the strong shear region are so large that the

probe bias supply is sometimes unable to draw electron saturation current. The I–V curves in this case have no linear region (the right-most part of the curve in Fig. 2), preventing accurate determination of the plasma potential. This was a common problem at 42 cm, and only complete I–V curves were used in the determination of V_p. However, examination of the incomplete I–V curves suggested that V_p at 42 cm may actually be more positive than shown in Fig. 6.

The region of strongest shear during PPCD (F ~ −0.9) is located deeper inside the plasma than the shear region in EC discharges with F ~ −0.5, suggesting that the location of strong shear may track the reversal radius. The position of the reversal radius depends on F, and as F becomes more negative, the reversal radius decreases. It is possible that at higher plasma current, where EC discharges with fairly weak reversal (F ~ −0.2) are possible, the region of strong shear may develop at a larger minor radius than it does in low current, strongly reversed discharges.

4.2 Local transport barriers in EC and PPCD discharges?

There is suggestive, but not conclusive evidence that the $\mathbf{E} \times \mathbf{B}$ flow shear and the associated reduction of edge fluctuations (Chapter 6) constitutes a barrier to transport in the edge of EC and PPCD discharges. The evidence is based on interferometric measurements of the density profile and probe measurements of various edge quantities.

Figure 7 shows electron density profiles measured with an 11-chord interferometer, which has a spatial resolution (determined primarily by channel-to-channel spacing) of ~ 8 cm. Figure 7(a) shows

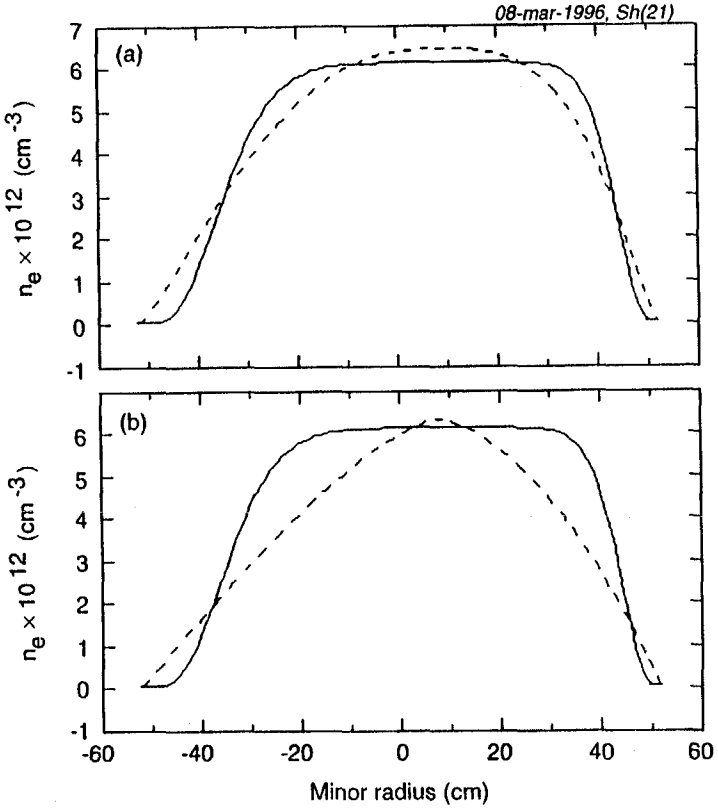

Fig. 7. (a) electron density profiles in an EC period during an SDE (dashed line) and between SDE's (solid line) and (b) a comparison of the density profile (dashed line) during a pre-EC transition phase (roughly 1 ms after a sawtooth crash) and the between-SDE profile shown in (a).

two density profiles during an EC period. One profile was measured between small dynamo events (SDE's), while the other was measured during an SDE. The flat profile, which falls off sharply in the edge, is common between SDE's in EC and PPCD discharges. When an SDE occurs, the flat profile becomes more rounded, and the edge gradient is relaxed, consistent with SDE's degrading edge confinement. The edge perturbing effect of each SDE may play an important role in the probe-measured data discussed later in this section. One other effect of each SDE is a slight increase in the core density. The mechanism underlying this effect is unknown, but there is an apparent increase in the core particle confinement time or the particle source rate.

Refer now to Fig. 7(b), in which is shown a comparison of the between-SDE density profile and the profile during a pre-EC transition phase, after a sawtooth crash but before the onset of discrete SDE's. Such a transition is seen from about 12 - 13 ms in Fig. 1 of Chapter 5. As the transition phase gives way to the full-fledged EC period, the profile becomes flatter and flatter with a gradual steepening of the edge profile.

The steep edge profile suggests the presence of a transport barrier and that this barrier is relaxed with each SDE, similar to the dynamics of H-mode discharges exhibiting ELM's [8]. However, the density profile in weakly reversed, non-EC discharges has a shape (to within the resolution of the measurement) similar to that of the between-SDE profile in EC periods. A large density gradient in the edge of standard discharges is not surprising, since it is a commonly held notion that the RFP edge always acts as a transport barrier to some extent. Thus, this

data does not confirm or deny that the $\mathbf{E} \times \mathbf{B}$ flow shear and edge fluctuation reduction in EC and PPCD discharges corresponds to a larger–than–normal reduction in transport.

From the data in Fig. 3, one can roughly estimate $T_e = (V_p - V_f)/\alpha$ for EC discharges. With α = 2.5 (calculated from MST parameters), one estimates T_e(46 cm) ~ 16 eV and T_e(44 cm) ~ 32 eV, suggesting that the electron temperature doubles going from outside to inside the region of strong flow shear. Note, however, that these numbers very likely underestimate T_e, since effects such as secondary electron emission add a positive offset to V_f everywhere [5]. To correct for such effects, one needs the electron energy distribution in the edge, and this data is not yet available for EC (or PPCD) discharges.

Figure 8 shows profiles of the ion saturation current $J_s \sim n_e T_e^{1/2}$ (where n_e is the electron density) for EC, PPCD, and standard discharges. Also included are the EC and PPCD radial electric field profiles. The ion saturation current and ∇J_s in EC and PPCD discharges are both larger than that in standard discharges over most of the plasma edge. The EC profile is steepest in two locations (indicated by solid lines), both overlapping the region of strong $\mathbf{E} \times \mathbf{B}$ flow shear. From 44 to 43 cm, $\nabla J_s \sim$ 1.3 A/cm^2/cm, while from 46 to 45 cm, $\nabla J_s \sim$ 0.8 A/cm^2/cm. Thus, ∇n_e and/or ∇T_e are largest between 43 and 44 cm.

However, there is also a flat region in the EC profile, in the middle of the region of strong shear. This may reflect a local minimum in the flow shear, where the radial electric field peaks, but it may also reflect the presence of SDE's. One caveat regarding $J_s(r)$ is that it was measured several weeks apart from $V_p(r)$ and $V_f(r)$, and on the day it

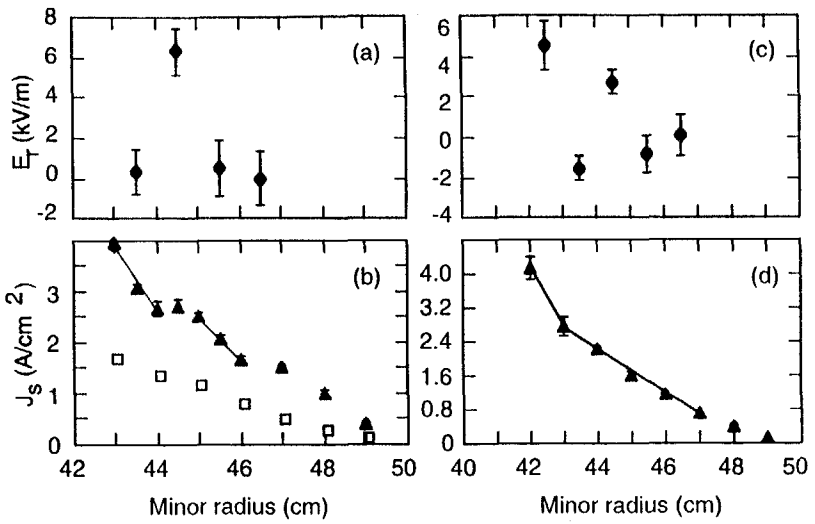

Fig. 8. Radial profiles of (a) radial electric field and (b) ion saturation current in EC discharges. These same profiles are plotted in (c) and (d) for PPCD discharges (note the change of scales). The ion saturation current profile from (weakly reversed) standard discharges is shown (box symbols) in (b). Error bars for this profile are smaller than the plot symbols.

was measured, SDE's were more frequent than they had been previously. Unavoidably, this and other data averages over SDE's. As shown in Fig. 7, SDE's tend to flatten the edge density profile. Thus, they may contribute to the local flat region. Such a local flattening of the density profile is one effect of ELM's in H–mode discharges [8].

Unlike the EC case, $J_s(r)$ in PPCD discharges [Fig. 8(d)] is smoother and shows no flat region. This may be due to the relative scarcity of SDE's during PPCD (discussed in Chapter 5). Still, $J_s \sim n_e T_e^{1/2}$ steepens

from 43 to 42 cm. In this region, ∇J_s ~ 1.4 A/cm^2/cm, compared to ~ 0.5 A/cm^2/cm beyond it. One puzzle, however, is why there is no apparent steepening of the profile beyond 43 cm, where the gradient in E_r is still significant. Of course, the profile in this region (and everywhere else) is still steeper than in the standard case, and local E_r gradient effects may be hidden.

There is one other observation that suggests the presence of a transport barrier in EC and PPCD discharges, as well as its absence in standard discharges. In the discussion of Fig. 5, I mentioned the onset of strong plasma-probe interaction in EC discharges. This occurs when probes are inserted 1 - 2 cm into the region of strong $\mathbf{E} \times \mathbf{B}$ flow shear, suggesting a substantial increase (versus radius) in the density and/or temperature in that region. Significantly, the radius at which the strong interaction occurs moves with the shear region. For example, in the EC discharges comprising Fig. 3, the region of strong shear developed around 44 cm. In this case, a probe could be inserted to about 46 cm without significant interaction. When the probe was moved to about 44 cm, however, plasma-probe interaction increased substantially.

In PPCD discharges, such as those comprising the data in Fig. 6, the onset of strong plasma-probe interaction only occurred when the probe was inserted deeper than 43 cm. In standard discharges, probes can be inserted to at least 42 cm without significant increases in plasma-probe interaction. When the interaction does occur, it causes erosion of the probe body, not the data-gathering probe tips. Thus, the onset of plasma-probe interaction does not taint the data.

The observations described in this section are suggestive of the

presence of a transport barrier in EC and PPCD discharges. The apparent increase in density and/or temperature in the region of strong shear are consistent with this idea. Further, since ∇J_s in EC and PPCD discharges is larger than in standard discharges over the entire plasma edge, it is possible that the entire edge acts as a transport barrier. This is conceivable, given the edge-wide reduction of fluctuations in these discharges (Chapter 6).

4.3 Impurity ion flow in EC and PPCD discharges

In many devices other than the MST, the radial force balance equation [Eq. (1)] is used to reconstruct the radial electric field profile, and all three terms (the pressure gradient, and poloidal and toroidal rotation) are important. The MST's diagnostic set does not yet allow local measurements of any of these terms. However, one is able to measure impurity ion toroidal rotation averaged over some fraction of the minor radius [12]. As will be discussed below, this measurement has severe limitations when considering the highly localized nature of the strong radial electric field gradients. Nevertheless, impurity ion toroidal rotation in some (but not all) EC and PPCD discharges exhibits interesting behavior not usually seen in standard discharges. This behavior may reflect the substantial change in the radial electric field in these discharges.

In Fig. 9 is the C III (an edge impurity species) velocity during two 400 kA discharges, both of which are locked (i.e., the magnetic modes do not rotate in the lab frame of reference). The discharge on the left has only standard (degraded) confinement, while the discharge

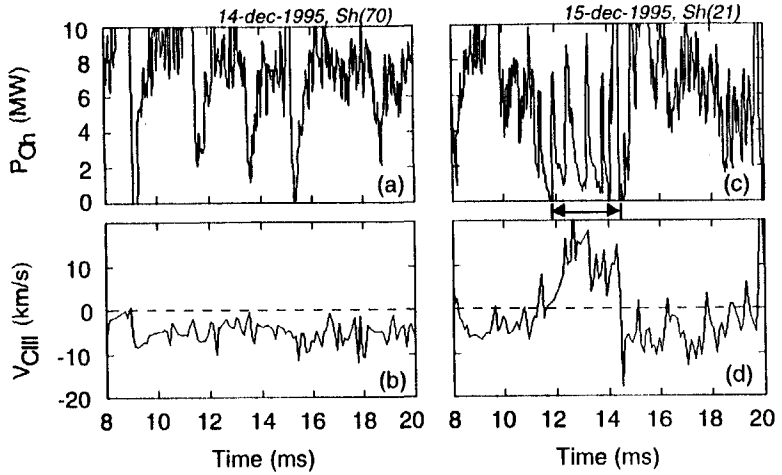

Fig. 9. (a) Ohmic input power and (b) velocity of C III ions in a strongly reversed, standard discharge. These same quantities are shown in (c) and (d) during a strongly reversed discharge with a brief EC period (indicated by arrows).

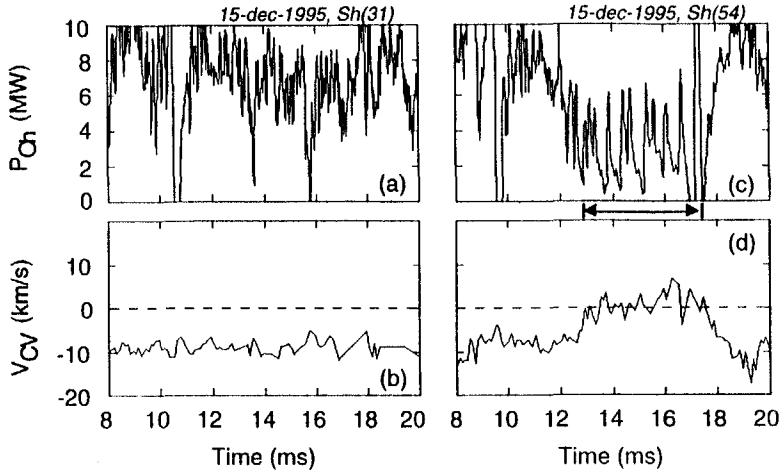

Fig. 10. (a) Ohmic input power and (b) velocity of C V ions in a strongly reversed, standard discharge. These same quantities are shown in (c) and (d) during a strongly reversed discharge with a brief EC period (indicated by arrows).

on the right exhibits a brief period of enhanced confinement. Normally, locking is associated with confinement degradation, but many EC periods have been observed in the presence of locking. For example, the discharge with the long EC period in Fig. 2 of Chapter 3 was locked.

The most striking feature in Fig. 9 is the reversal of the C III rotation velocity during the EC period. The change occurs quite rapidly. Such a reversal of flow direction can also be observed in the C V (a global impurity species) rotation during EC periods, an example of which is shown in Fig. 10. The discharges in Fig. 10 are also at 400 kA and are locked. In addition to the flow reversal, one notes that in both EC and standard discharges, the impurity ions have a finite rotation velocity even when the magnetic modes are locked. This is commonly observed and is consistent with differential diamagnetic rotation between the modes and plasma.

When the magnetic modes are not locked, impurity ion rotation does not usually reverse during EC periods. However, as in locked discharges, it does become less negative. In the sign convention used here, the modes rotate in the negative direction, and their rotation is somewhat coupled to the ions, leading to a more negative ion rotation velocity in the core and edge. Thus, mode rotation contributes a

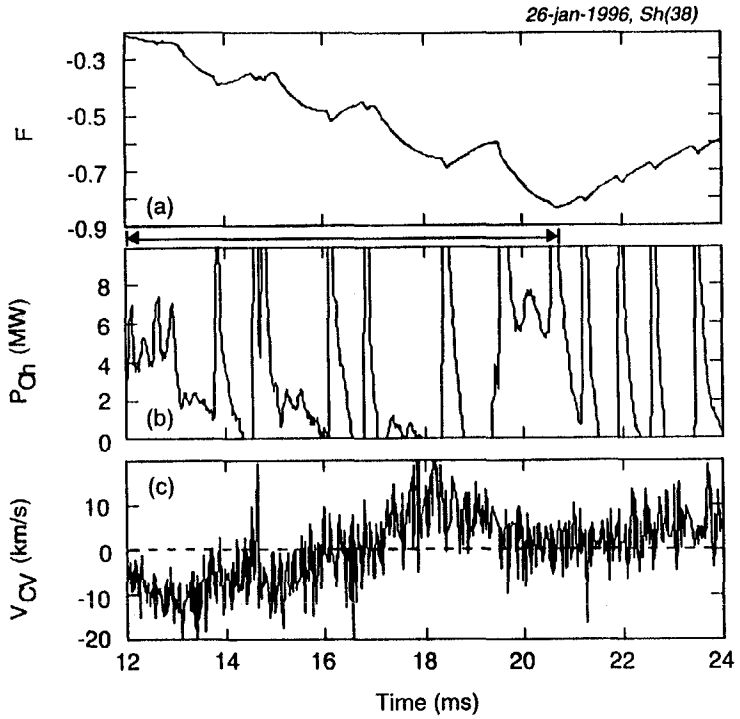

Fig. 11. (a) reversal parameter, (b) Ohmic input power, and (c) velocity of C V ions in a discharge with PPCD (indicated by arrows) followed by an EC period. PPCD ends just after 20 ms. The time resolution of the C V velocity shown here is finer than in the EC cases of Figs. 9 and 10.

negative offset to the ion rotation.

The rotation velocity of CV ions during PPCD is shown in Fig. 11. Data showing the rotation of C III ions during PPCD is not available. The reversal parameter is included in Fig. 11 to illustrate when PPCD begins

and ends. Note that following PPCD, at about 21 ms, there is an EC period. This discharge is unlocked until 16 ms and locked thereafter. Similar to the EC case in Fig. 10, the CV rotation reverses during PPCD, after locking occurs. It also reverses in the EC period following PPCD.

Substantial changes in the globally averaged impurity rotation velocity do not always occur during EC periods or PPCD. For example, the C III velocity was monitored in 200 kA, F ~ −0.5 EC periods, and the velocity in this case was about the same as that in standard cases. This apparent lack of change may be due to the many subtleties associated with the interpretation of these flow measurements. The flow velocities may or may not reflect local changes in the edge radial electric field.

One of the problems lies in the fact that the (passive) flow measurements depend on the emission profiles of C III and C V. Impurity ion flow can only be measured where the impurity ion line radiation is sufficiently strong to be detected by the spectrometer. For instance, C V ions can exist over much of the plasma cross section, so measurements of C V rotation (and temperature) will typically be global averages. On the other hand, C III ions are typically localized to the edge, which in some cases may be well outside the shear region of EC and PPCD discharges. The shape of impurity emission profiles depends on the plasma temperature and density, as well as the rate of impurity particle diffusion. Further, the location of the strong shear region can vary, at least, with changes in the reversal of the edge toroidal magnetic field (see earlier discussion). The final average flow velocity is weighted toward those regions with the largest ion density (and radiation emission) and velocity. Techniques such as charge-exchange-

recombination spectroscopy with a neutral beam are required for local flow measurements.

4.4 The effect on rotation of reversal, fueling, and wall conditioning

In Chapter 3, I discussed the importance of toroidal field reversal and fueling for the achievement of EC and PPCD discharges. These dependencies may be due in part to effects on plasma rotation. I will now show data revealing the dependence of bulk rotation on toroidal field reversal, and I will discuss the ideas that the fueling technique, fuel isotope, and condition of the plasma-facing wall can play an important role in plasma rotation. Anything that affects plasma rotation will, through Eq. (1), affect E_r and its gradient.

Figure 12 shows the rotation (phase) velocity of the (m = 1, n = 6) core-resonant tearing mode for different values of F. Keeping the plasma current and density fixed, F was varied from −0.1 to −0.4 in deuterium discharges. The maximum phase velocity increases from about 35 km/s at F = −0.1 to about 70 km/s at F = −0.4. To my knowledge, the latter is the fastest rotation ever observed in the MST. The C V rotation was not measured in these discharges, but the modes and C V rotation typically track one another [13]. The C III rotation was measured, and it was found to vary with the mode rotation, suggesting a link between the core and the edge (where C III resides). At F = −0.1, the C III velocity was about −5 km/s, while at F = −0.4, it increased to about −20 km/s, where the minus sign indicates that the C III rotation is in the direction of the mode rotation.

The reason that reversal affects mode and plasma rotation is not

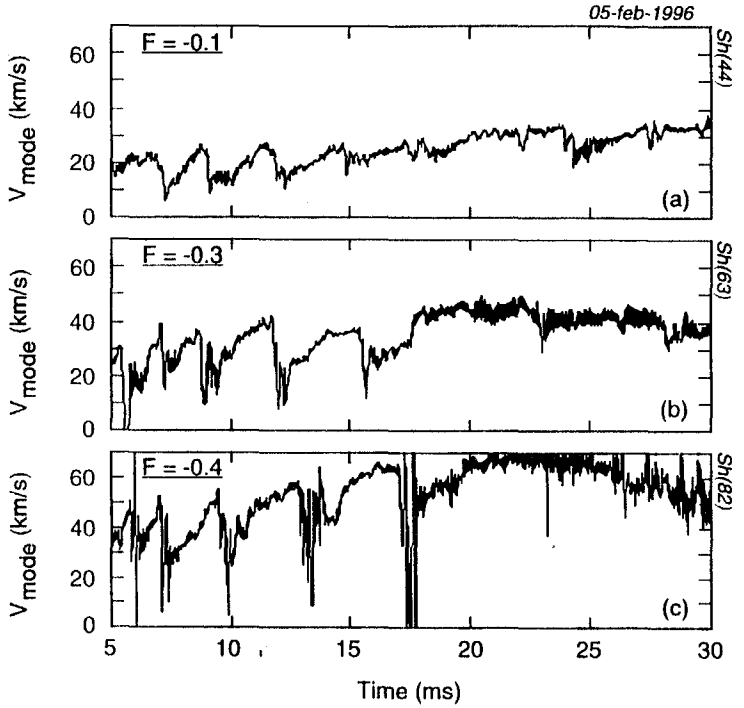

Fig. 12. Phase velocity of the m = 1, n = 6 mode with (a) F = -0.1, (b) F = -0.3, and (c) F = -0.4. These velocities shown as positive for convenience, but they are actually negative in the MST sign convention.

known, but it may be related to the proximity of the reversal radius to the wall. All m = 0 modes are resonant at the reversal radius, and it is believed that they interact with the wall, resulting in a drag on them and the edge plasma. Moving these modes away from the wall, and in

particular, the field-error-prone poloidal and toroidal gaps, may weaken this drag. By nonlinear coupling [14], the rotation of the core-resonant m = 1 modes can be influenced by that of the m = 0 modes, thereby linking the core and the edge rotation.

Note that operation at F = -0.4 does not automatically lead to rapid rotation such as that in Fig. 12. In fact, I have not witnessed such rapid rotation since observing these discharges. As is discussed next, the fueling technique and fuel isotope as well as the condition of the plasma-facing wall can also play a role in plasma rotation, and they may have played a role in the discharges in Fig. 12.

In an important paper on rotation in Ohmically heated tokamak discharges, Rowan *et al.* [15] discussed the effect of neutral particles (specifically hydrogen and helium) on plasma rotation. Neutral particles can reduce the flow velocity in the plasma edge by at least two means. When a neutral particle enters the plasma, it will eventually be ionized either by electron impact or charge exchange, and both processes can reduce plasma flow. In the case of electron impact, the neutral is simply ionized, and it must then be accelerated from a low energy. This is a process of equilibration that produces a drag on the plasma. In the second case, the neutral loses it electron(s) by direct charge exchange with a plasma ion. If this ion is a proton or deuteron, it becomes charge-neutral and quickly leaves the plasma, carrying with it some of the plasma's momentum. Thus, charge exchange is a means by which momentum is transported out of the plasma.

The impact of these neutrals varies in part with the depth to which they penetrate before losing an electron. The farther the

neutrals penetrate, the larger the fraction of the plasma volume they can affect. For a given input energy, the velocity of a neutral is determined by its mass. However, the time required for ionization (by electron impact or charge exchange) is similar for all particle species of interest. Thus, heavier neutrals (e.g., helium) will not penetrate as far as lighter ones (e.g., hydrogen). Rowan *et al.*, [15] measured the velocity of C V ions in the edge of the TEXT tokamak and found it to be larger in helium discharges than in hydrogen discharges, consistent with the differing penetration depths of hydrogen and helium.

It is in this context that the fueling technique and fuel isotope in the MST can play a significant role. Wall fuel (see Chapter 3) consists of a smaller neutral fraction than the completely neutral puffed fuel. Thus, wall fuel may have a lesser effect on edge plasma rotation. Deuterium is more massive than hydrogen, so use of deuterium may further minimize rotation damping. In addition to plasma rotation, neutrals can affect the edge pressure and its gradient. Thus, through all three terms in Eq. (1), neutrals can affect the radial electric field, including its gradient. This may help to explain the observation that wall fueling and deuterium leads to more reproducible EC discharges than puffed fueling and hydrogen. Interestingly, the heating power threshold for H-mode has an isotopic dependence, with the power necessary in hydrogen being larger than that in deuterium [16].

Impurity influx can also affect rotation, regardless of the smaller neutral impurity penetration depth, for the same reasons discussed by Rowan *et al.* [15]. This may explain in part why wall conditioning is required for EC and PPCD discharges, as well as H-mode discharges in

other devices. In a study on the DIII-D tokamak, it was found that boronization allowed faster plasma rotation [17]. In an impurity doping experiment in the MST, it was found that substantial amounts of puffed argon could slow or even stop the rotation of the dominant magnetic modes, which are closely coupled to the rotation of the bulk plasma [13,18].

Referring back to Fig. 12, the record rate of rotation shown there may then be understandable in part due to effects of fuel and impurity neutrals. These discharges were in deuterium and they were fueled entirely by the wall from 0 – 30 ms. Further, they took place at a time when the plasma-facing wall was well conditioned, by boronization and intensive high-current RFP discharges. Thus, in addition to the dependence on reversal, rotation may depend on fueling and wall conditioning.

The ideas above may help explain some observations regarding locking. For a given plasma current, there is a locking dependence on toroidal field reversal, density, and fuel isotope. Discharges with weak reversal, higher density, or hydrogen fueling are more likely to lock than discharges with strong reversal, lower density, or deuterium fueling. The dependence on reversal and fuel isotope may be understandable in terms of the ideas in the preceding discussion. The dependence on density may be as well, for high density generally leads to higher recycling and a larger edge neutral population. Historically, mode locking has been linked primarily to magnetic field errors, but it is clear that there are other contributing effects as well.

4.5 What triggers the large radial electric field gradient?

There is no theoretical or experimental work specific to the RFP regarding formation of a strongly inhomogeneous radial electric field. Thus, as a first cut at identifying the triggering mechanism in the MST, one must look at the data concerning the large radial electric field gradient in tokamak H-mode discharges. As discussed in Chapter 2, it has been well established empirically that the H-mode in tokamaks and stellarators can be triggered by sufficient heat flux through the plasma edge [16]. More specifically, it is heat flux through the region where the strong shear forms, apparently to achieve the necessary threshold temperature. Further, there are constraints on the density and magnetic field strength that affect the level of heating power necessary for H-mode, and failing to satisfy these constraints can prevent an H-mode altogether [16]. Thus, heat flux is only one ingredient (and the final ingredient) necessary for an H-mode.

To trigger an H-mode in a controllable manner, the necessary heat flux is commonly provided by auxiliary techniques such as neutral beam or radio frequency heating [8]. However, the necessary heat flux can also be provided spontaneously by sawtooth crashes, which cause the rapid transport of particles and energy from the plasma core to the edge. Sawtooth crashes are the sole triggering mechanism in Ohmically heated H-mode discharges, and they sometimes act as the trigger in auxiliary heated discharges as well [19,20,21].

In EC and PPCD discharges in the MST, there are also potential edge heating mechanisms at work. EC periods always follow sawtooth crashes, which cause transport from the core to the edge similar to

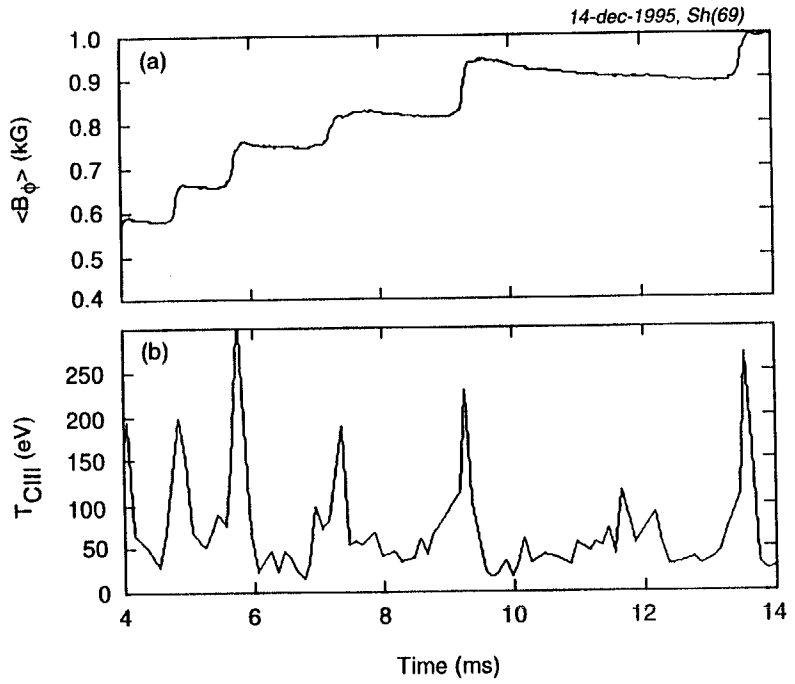

Fig. 13. (a) cross-section-averaged toroidal magnetic field and (b) temperature of C III ions. The C III temperature increases with each sawtooth crash.

sawteeth in tokamaks, and the auxiliary edge current associated with PPCD must cause some level of Ohmic heating. Thus, the possibility exists that the strong shear in the MST is brought about by heating. Verification of this hypothesis, and the presence of a possible temperature threshold, awaits local measurements of the electron and majority ion temperatures in the edge of these discharges. However, at

least in the case of sawtooth crashes, there is already evidence for a momentary increase in the edge temperature.

To illustrate the edge heating that occurs with sawtooth crashes, the temperature of (edge localized) C III ions is shown in Fig. 13. Observe the sharp increase in temperature with each sawtooth crash. Such an increase has also been observed in qualitative soft x-ray measurements of the electron temperature [22]. The overall increase in heat flux at the crash was also observed by Fiksel *et al.* [23]. Core-to-edge transport is not the only edge heating mechanism at work during sawtooth crashes. For instance, each crash causes a large increase in parallel current in the edge (to flatten the current profile), thereby resulting in additional Ohmic heating [24].

The poloidal current driven during PPCD is illustrated in Fig. 14. The PPCD pulse begins shortly after 10 ms. Coincident with this pulse is an increase in the total poloidal current, calculated with the so-called modified polynomial function model [25]. This figure also illustrates the increase in poloidal current during sawtooth crashes, before PPCD begins, and during small dynamo events, which occur during PPCD.

The PPCD pulse can directly and indirectly heat the region where the strong shear will form. Direct heating will occur if the current induced by the PPCD pulse reaches this region and causes local Ohmic heating. For PPCD in 200 kA discharges, this requires the PPCD current pulse to diffuse about 10 cm into the plasma in about 1 – 2 ms. An indirect means by which the (future) shear region can be heated is by inward heat transport. Some Ohmic heating will certainly occur at a larger minor radius than where the shear will form. This heat may then

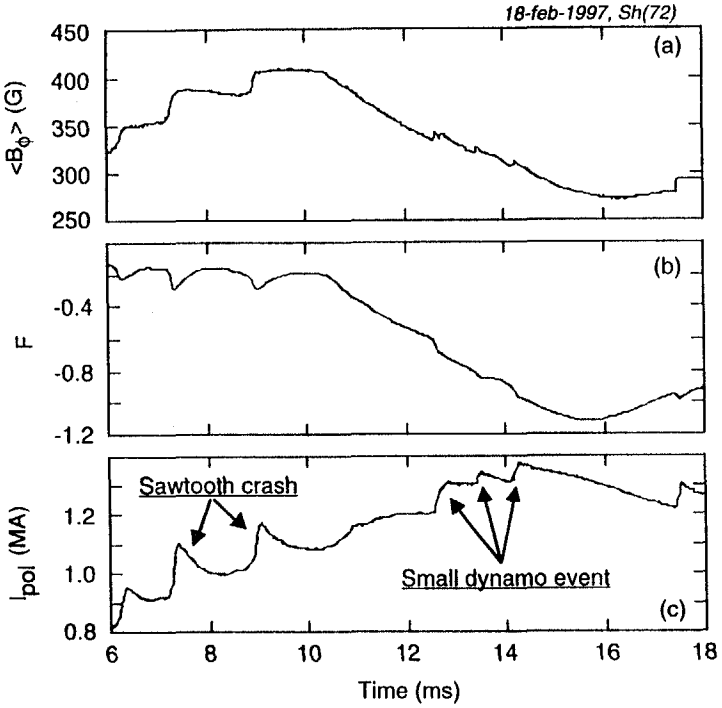

Fig. 14. (a) cross-section-averaged toroidal magnetic field, (b) reversal parameter, and (c) total calculated poloidal current in a discharge with PPCD. PPCD starts just after 10 ms.

be transported inward at a rate that is likely faster than the rate of current transport (resistive diffusion).

There is a threshold PPCD current, determined in part by the toroidal plasma current and electron density, below which PPCD can actually degrade a discharge, or at best have no effect. Figure 15 shows

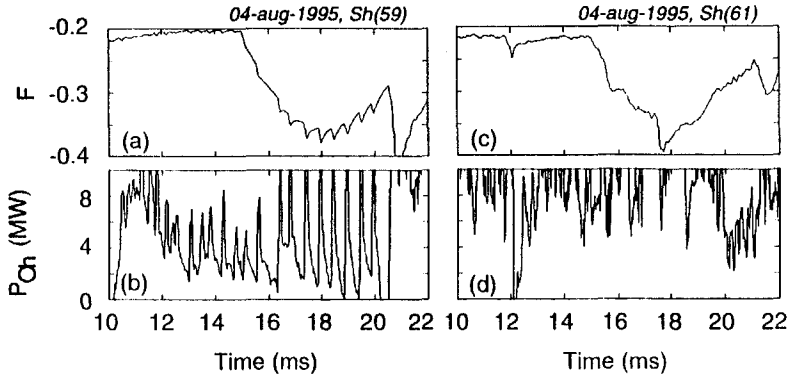

Fig. 15. (a) reversal parameter and (b) Ohmic input power in a discharge in which PPCD starts during an EC period. In (c) and (d) are these same quantities in a discharge with PPCD but without an EC period.

two discharges with PPCD below the threshold. Lower PPCD current leads to weaker reversal (compare the reversal parameter in Fig. 15 with that of, e.g., Fig. 14). Figure 15(d) illustrates the typical result when PPCD is fired below threshold into a standard discharge. In Fig. 15(b), on the other hand, is a discharge in which PPCD is fired during an EC period. Here, PPCD increases the small dynamo event amplitude to the level usually observed with PPCD. In other words, PPCD was able to function below the normal threshold with a pre-established EC period. *If* the edge is hotter during EC periods than during standard discharges, and *if* there is a temperature threshold for PPCD as there is for an H-mode, then this result can be understood in terms of edge heating.

4.6 Summary

In this chapter I have described the existence of strong $\mathbf{E} \times \mathbf{B}$ flow shear in the edge of EC and PPCD discharges. The potential importance of this shear in the improved EC and PPCD confinement is suggested primarily by probe-measured data in the edge. Apparently, the temperature and/or density profiles steepen in the region of strong shear and over the entire edge plasma, relative to standard discharges. Measurements of the time dependent floating potential profile (related to the plasma potential profile) reveal that the development of the $\mathbf{E} \times \mathbf{B}$ flow shear occurs before edge fluctuations are reduced, as anticipated, but that the reduction occurs on a relatively long (~ 1 ms) timescale.

I also described the effect on rotation of, e.g., toroidal field reversal and wall conditioning. Through the radial force balance equation, variations in rotation can affect the radial electric field profile and the $\mathbf{E} \times \mathbf{B}$ flow shear. Further, I suggested that, as is the case in H-mode discharges, edge heating may play an important role in the development of the strongly inhomogeneous radial electric field. This implies that auxiliary heating could be of benefit to the RFP.

References

[1] I would like to thank C.-S. Chiang for all his help with these probe measurements, particularly his construction and implementation of numerous probes, often on short notice.

[2] M. R. Stoneking *et al.*, Phys. Rev. Lett. **73**, 549 (1994).

[3] M. R. Stoneking, Ph.D. thesis, University of Wisconsin, Madison, Wisconsin, 1994.

[4] R. Balbin *et al.*, Rev. Sci. Instrum. **63**, 4605 (1992).

[5] N. Hershkowitz, in Plasma Diagnostics: Discharge Parameters and Chemistry, Vol. 1, edited by O. Anciello and D. L. Flamm (Academic, New York, 1991).

[6] P. R. Bevington and D. K. Robinson, Data Reduction and Error Analysis for the Physical Sciences, 2nd ed. (McGraw-Hill, New York, 1992).

[7] H. Ji, PLP Report No. 1145, University of Wisconsin, Madison Wisconsin, 1994.

[8] R. J. Groebner, Phys. Fl. B **5**, 2343 (1993).

[9] K. H. Burrell, Phys. Plasmas **4**, 1499 (1997).

[10] T. S. Hahm and K. H. Burrell, Phys. Plasmas **2**, 1648 (1995).

[11] H. Biglari, P. H. Diamond, and P. W. Terry, Phys. Fl. **2**, 1 (1990).

[12] D. J. Den Hartog and R. J. Fonck, Rev. Sci. Instrum. **65**, 3238 (1994).

[13] D. J. Den Hartog *et al.*, Phys. Plasmas **2**, 2281 (1995).

[14] S. Assadi, S. C. Prager, and K. L. Sidikman, Phys. Rev. Lett. **69**, 281 (1992).

[15] W. L. Rowan *et al.*, Phys. Fl. B **5**, 2485 (1993).

[16] T. N. Carlstrom, Plasma Phys. Controlled Fusion **38**, 1149 (1996).

[17] C. L. Rettig *et al.*, Phys. Fl. B **5**, 2428 (1993).

[18] S. Assadi, Ph.D. thesis, University of Wisconsin, Madison, Wisconsin, 1994.

[19] F. Wagner *et al.*, Phys. Rev. Lett. **53**, 1453 (1984).

[20] T. H. Osborne *et al.*, Nucl. Fusion **30**, 2023 (1990).

[21] Y. Muira *et al.*, Plasma Phys. Controlled Fusion **36**, A81 (1994).

[22] J. A. Beckstead, Ph.D. thesis, University of Wisconsin, Madison, Wisconsin, 1990.

[23] G. Fiksel *et al.*, Phys Rev. Lett. **72**, 1028 (1994).

[24] A. F. Almagri *et al.*, Phys. Fl. B **4**, 4080 (1992).

[25] W. Shen and J. C Sprott, Phys. Fl. B **3**, 1225 (1991).

5. Small dynamo events

Small dynamo events play many important roles in EC and PPCD discharges, and they appear with the same basic phenomenology in both cases. This chapter focuses on some of the characteristics and effects of small dynamo events, a few of which have been mentioned in previous chapters. In Sec. 5.0, I first discuss the parallel current and flux production associated with small dynamo events. These events are a new type of discrete dynamo. I also describe their effect on the dominant magnetic modes as well as possible causes of these events. In Sec. 5.1, I discuss the controllability of small dynamo events, both in amplitude and frequency of occurrence. Similar in some ways to the case of edge-localized modes in H-mode (Chapter 2), control of small dynamo events has proven critical to maximizing the confinement in both EC and PPCD discharges. In Sec. 5.2 is the chapter summary.

5.0 Introduction to small dynamo events

Small dynamo events (SDE's), like sawtooth crashes, correspond to discrete bursts of dynamo activity, characterized by an increase in parallel current (and generation of toroidal flux, in these cases). Sawtooth crashes occur when the core-resonant m = 1 magnetic modes are destabilized by a gradient in the $\mu = \mu_o \mathbf{J}\cdot\mathbf{B}/B^2$ profile. The parallel current associated with each crash then reduces this gradient and stabilizes the modes. On the other hand, small dynamo events first appear in the edge-resonant modes, such as those with m = 0, and the root cause of the events has not been identified. It is not known

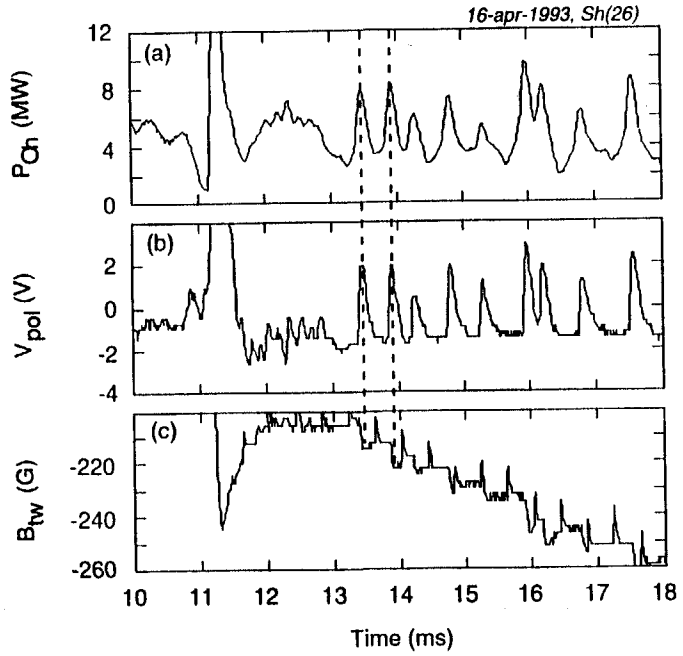

Fig. 1. (a) Ohmic input power, (b) surface poloidal voltage, and (c) toroidal magnetic field at the wall (plasma edge) during a discharge with an EC period. This is the same discharge as shown in Fig. 2 of Chapter 3.

whether the current driven by each small dynamo event stabilizes the edge modes (as occurs with sawtooth crashes and the core modes). The modality and possible causes of SDE's are discussed more below.

The toroidal flux generation associated with SDE's is illustrated in Fig. 1. In the discharge shown here, a sawtooth crash occurs just after 11 ms and is followed by an EC period. Before the onset of discrete

SDE's at about 13.5 ms, there is an approximately 2 ms transition period. The surface poloidal voltage and toroidal field at the wall are shown in Figs. 1(b) and 1(c). Recall that a positive increase in the surface poloidal voltage corresponds to an increase in the positive (nonreversed) toroidal flux in the plasma volume. Thus, with each SDE, the total toroidal flux increases, but at the same time, the toroidal field at the edge becomes more negative (reversed). This is characteristic of an RFP dynamo event. While the changes in toroidal flux are measured with coils external to the plasma, the burst of parallel current associated with this flux production has been measured in the plasma edge with an insertable Rogowski probe (data not shown). Note the plateau in the edge toroidal field in the transition phase, corresponding to a lack of SDE's. There are, however, tiny bursts evident in the surface poloidal voltage during this phase which may be precursory SDE's.

Sawtooth crashes and small dynamo events are alike in that both appear in the dominant magnetic modes, which in the MST have poloidal mode numbers m = 1 and m = 0. However, this is where the similarity between these two types of dynamo event ends. A series of SDE's is shown in Fig. 2. The surface poloidal voltage is shown for reference, as usual. Each burst in the surface poloidal voltage is accompanied by a burst in the modes with n = 1 (and m = 0, if the n = 1 is resonant) and n = 30 (and m = 1). The mode amplitudes are measured with an internal array of magnetic sensing coils. All modes with m = 0 are resonant at the reversal radius (where q = m/n = 0), the position of which varies with toroidal field reversal and typically lies somewhere in the outer 25% of the plasma. High-n modes such as the n

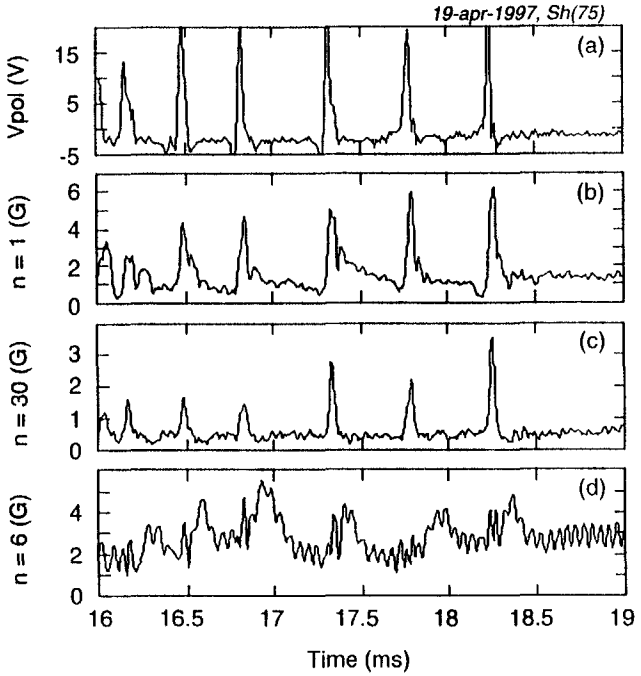

Fig. 2. (a) Surface poloidal voltage and (b)-(d) amplitudes of various magnetic modes during an EC period. Each burst is a small dynamo event.

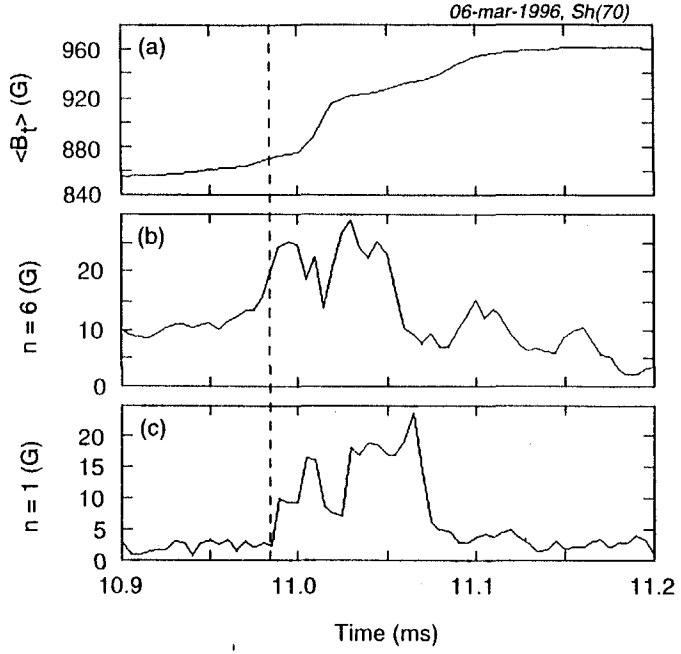

Fig. 3. (a) cross-section-averaged toroidal magnetic field, (b) m=1, n=6 mode amplitude, (c) m=0, n=1 mode amplitude. A sawtooth crash begins just before 11 ms.

= 30 (with q = 1/30 = 0.033) are resonant just inside the reversal radius (at a slightly smaller minor radius).

There is also a response to each SDE in the innermost resonant modes, represented here by the (m = 1, n = 6) or (1,6) mode. However, the response is sometimes delayed by a short time relative to the response in the n = 1 and n = 30 modes, and it is also somewhat broader in time. That the small dynamo event, which apparently originates in the edge, can quickly affect a core-resonant m = 1 mode may be due to the global nature of the m = 1 modes. These modes' eigenfunctions span most of the plasma cross section, and the modes can be influenced by gradients (or the lack thereof) far from their resonant surfaces [1,2]. Thus, the current generated by each SDE, e.g., may directly affect the m

= 1 amplitudes.

The sequence in which the m = 1 and m = 0 modes respond to each SDE is opposite that in which they respond to a sawtooth crash. Typically, as shown in Fig. 3, crashes begin with a sharp increase in the amplitude of the innermost resonant mode. This is followed closely by responses in such modes as the (0,1). Thus, as far as the sequence of mode response is concerned, sawtooth crashes are inside–out events, while SDE's are outside–in. This is consistent with other data, such as the time evolution of the electron density profile, which suggests that SDE's originate in the edge, unlike crashes, which originate in the core.

There are several other differences between crashes and SDE's. One is that SDE's are far less destructive than crashes. This is illustrated in Fig. 4, which contains an EC period, a period with PPCD, and a sawtooth crash. Clearly, the response in the Ohmic input power and radiation from impurity and fuel particles is substantially lower during SDE's than during the crash. Thus, SDE's produce toroidal flux in a significantly less destructive manner than sawtooth crashes. Another noteworthy aspect of the discharge in Fig. 4 is that the amplitude of the SDE response in the radiation signals follows that of the Ohmic input power. Going from the EC to the PPCD phase, the SDE amplitude increases in all three signals. Magnetic modes resonant in the plasma edge, such as the (0,1), respond in a similar manner.

Another difference lies in the apparent role played by the modes in each case. Sawtooth crashes ultimately arise from destabilization of the core–resonant m = 1 modes, which occurs due to peaking of the parallel current profile. It is not known, however, if SDE's are *caused* by

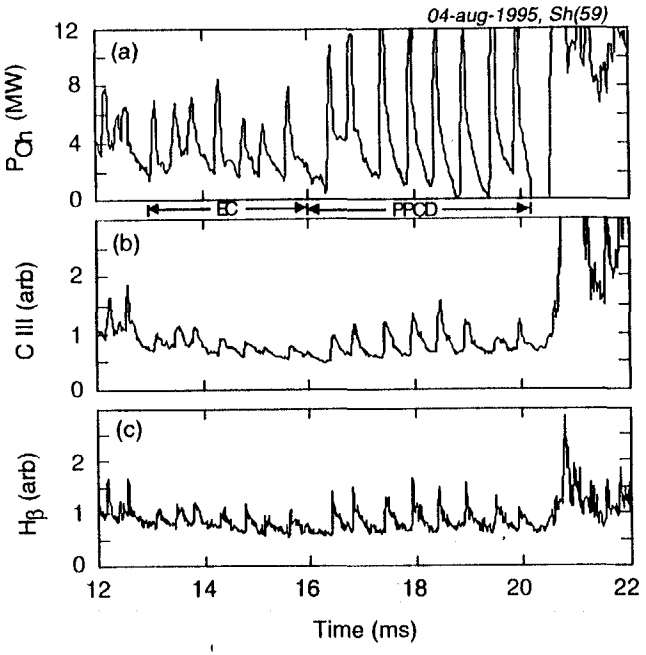

Fig. 4. (a) Ohmic input power, (b) C III (464.74 nm) radiation, and (c) neutral hydrogen radiation during a discharge with an EC period from 13-16 ms, a PPCD pulse from 16-20 ms, and a sawtooth crash at 20.5 ms.

destabilization of the edge–resonant modes or whether these modes are simply responding to changes induced by other means. In other words, the destabilization of the edge magnetic modes with each SDE may just be a reflection of the event and not a root cause.

One bit of evidence that may address this question was presented in Fig. 8(b) of Chapter 4. This figure shows the profile of the ion

saturation current, a quantity proportional to the density and temperature. This profile, averaged (in time) over small dynamo events, exhibits a flat region in the middle of the region of strong $\mathbf{E} \times \mathbf{B}$ flow shear. This (weakly) suggests that each small dynamo event begins in the region of strong shear, flattening the local density and/or temperature profiles. Since the saturation current was not flat elsewhere, and since the shear region is several centimeters away from the reversal radius, this implies that the destabilization of the edge magnetic modes may simply be a response to each event. However, the saturation current profile has not been measured near the reversal radius.

What causes the small dynamo events? If one ignores the weak evidence presented in the previous paragraph and assumes that destabilization of the (0,1) and other nearby modes is the root cause of SDE's, it is possible that edge gradients in the pressure and/or $\mu = \mu_o \mathbf{J}\cdot\mathbf{B}/B^2$ profiles play a role. Simulations have shown that both gradients can destabilize the m = 0 modes [2]. Data presented in Chapter 4, e.g., the ion saturation current profiles, suggest that the $\mathbf{E} \times \mathbf{B}$ flow shear region (and perhaps the entire edge) provides a barrier to transport and that the density and/or temperature gradients may be substantial (compared to standard discharges). Comparison of the electron density profile between and during SDE's in Fig. 5 (reproduced from Chapter 4) confirms that there is a large density gradient in the edge region and that this gradient is momentarily relaxed by each SDE. This data suggests that a pressure gradient may be involved. However, a large edge temperature gradient, if any, translates to a large

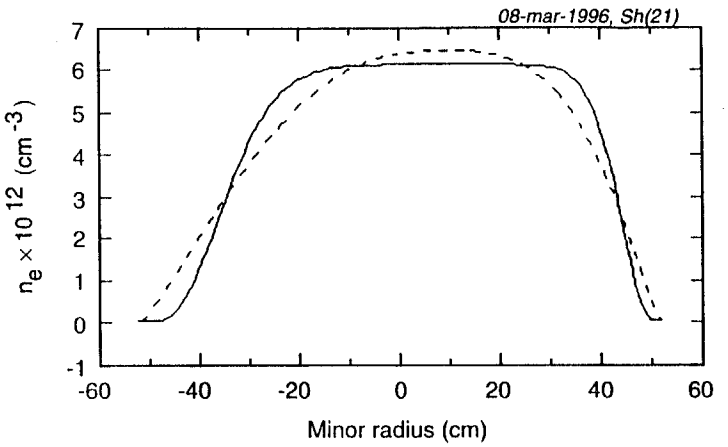

Fig. 5. Electron density profiles in an EC period during an SDE (dashed line) and between SDE's (solid line).

resistivity gradient, which in turn can result in a large gradient in $\mu(r)$. At this point, we are unable to rule out the importance of either gradient.

Magnetic fluctuations are commonly thought to be necessary for the (dynamo) sustainment of the RFP configuration [3]. In the case of sawtooth-crash dynamo, fluctuations in the core are large, resulting in increased core transport. In addition, core magnetic fluctuations increase the plasma resistivity, specifically its anomalous (non-Spitzer) component [3], thereby increasing the Ohmic input power. SDE's, on the other hand, cause only a small increase in the core mode amplitudes, and their usual impact on confinement is not as severe. It has long been a concern that dynamo-related fluctuations may ultimately

prevent the RFP from succeeding as a fusion concept. Disregarding advanced techniques such as radio frequency current drive, which may be able to reduce magnetic fluctuations *and* sustain the RFP magnetic configuration, SDE's provide some hope of sustainment without significant confinement degradation.

5.1 Controlling small dynamo events

As already illustrated in several examples, the amplitude of SDE's varies with toroidal field reversal. The reason for this variation is not yet known, but as the amplitude of SDE's becomes larger, confinement is increasingly degraded. This is obvious in the Ohmic input power (Fig. 4), and it is also obvious in the electron temperature. Figure 6 shows the ratio of two soft x-ray signals, which roughly indicates the central electron temperature, during EC periods of differing reversal and plasma current. The semi-regular drops in this ratio in each discharge are due to SDE's. At the weakest reversal shown [Fig. 6(a)], the drop in temperature is almost imperceptible, but as reversal is strengthened, the SDE-induced drop in temperature becomes substantial. The apparent rapid *increase* in temperature just before each decrease [most evident in Fig. 6(d)] may be real (due, perhaps, to Ohmic heating associated with the SDE current pulse), or it may be spurious (perhaps the result of impurity radiation contaminating the soft x-ray ratio) [4].

The amplitude of the SDE's clearly plays a significant role in MST confinement. Further, it is also clear that the SDE frequency (of occurrence) is also important. The lower the SDE frequency, the better the time-averaged energy confinement. As will be shown next,

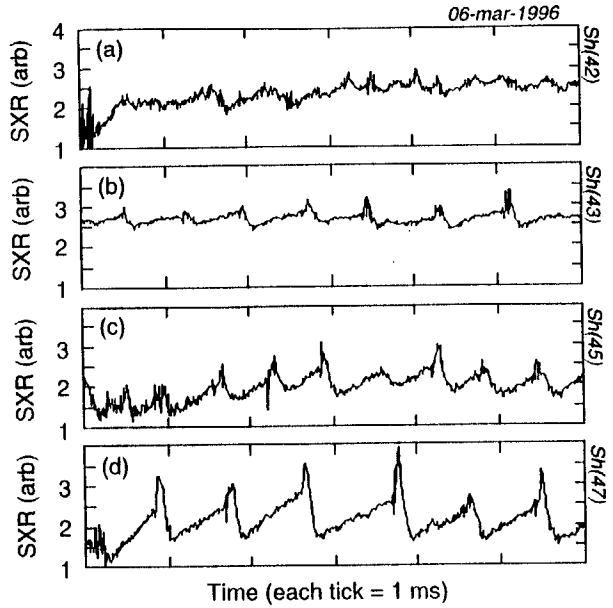

Fig. 6. Ratio of two soft x-ray signals (which roughly indicates the core electron temperature) during EC periods of varying reversal and plasma current: (a) F = -0.6, 290 kA, (b) F = -0.75, 250 kA, (c) F = -0.85, 230 kA, and (d) F = -1.05, 200 kA.

confinement is generally maximized when SDE's are suppressed for several ms.

EC and PPCD discharges were initially characterized by fairly regular SDE's, and this limited the maximum achievable confinement. The SDE frequency was typically 2 - 3 kHz. Now, multi-millisecond "SDE-free periods" are possible in both types of discharge. To achieve these periods, all of the EC/PPCD operational requirements (for fueling,

wall conditioning, etc., as discussed in Chapter 3) must be satisfied. Further, the longest SDE-free periods require an additional ingredient, reversal of the toroidal *electric* field (or toroidal loop voltage). Small dynamo event suppression may be related to favorable changes in the edge pressure and/or current density gradients, and such changes can occur with PPCD and toroidal electric field reversal.

In all RFP discharges, the toroidal magnetic field in the edge is reversed relative to its direction in the core. Thus, the usual inductive toroidal electric field that drives parallel ($\mu > 0$) plasma current in the core, drives antiparallel ($\mu < 0$) current in the edge, thereby contributing to the gradient in $\mu(r)$. This antiparallel inductive edge current is offset by parallel current driven by a fluctuation-based electric field, E_f [1,5]. PPCD adds to the parallel current in the edge [6,7]. Thus, PPCD may reduce the destabilizing $\nabla\mu$. Further, assuming E_f does not change significantly with the application of PPCD, the total edge current will increase, resulting in an increased Ohmic heating rate = ηJ^2 (η is the plasma resistivity) and a possible change in the edge pressure profile.

Reversal of the toroidal electric field can also affect the current and pressure profiles. In normal discharges, the toroidal electric field reduces the edge parallel current, but as the toroidal electric field is decreased and eventually reversed, it begins to work with E_f in driving parallel current in the edge. In this manner, it may reduce the current and pressure gradients, similar to PPCD. The amount of additional parallel current driven by a reversed toroidal electric field increases with toroidal magnetic field reversal. With stronger magnetic field

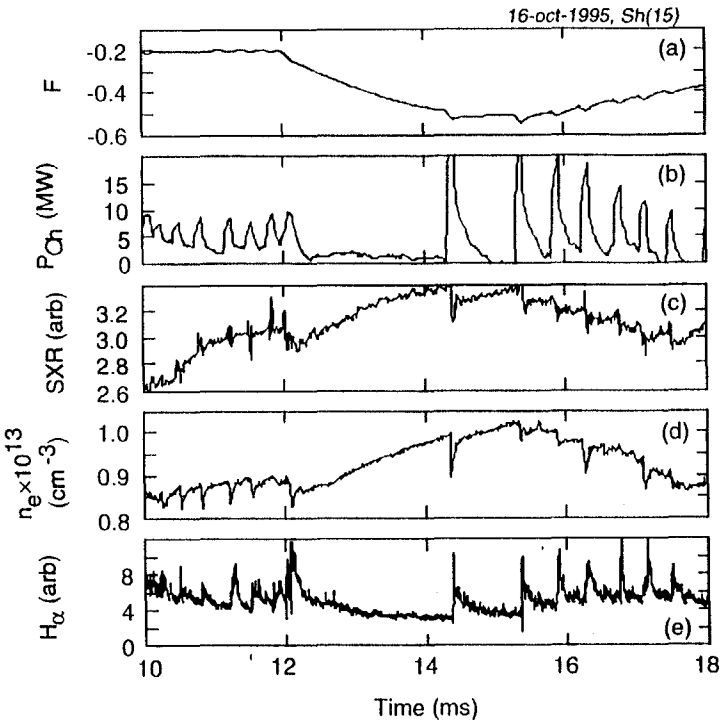

Fig. 7. (a) reversal parameter, (b) Ohmic input power, (c) soft x-ray ratio, (d) central line-averaged density, and (e) neutral hydrogen radiation during a discharge in which PPCD is fired (at 12 ms) into an EC period. The result is a 2 ms SDE-free period.

reversal, the toroidal component of the edge magnetic field is larger, thereby allowing more parallel current from a given toroidal electric field. Thus, EC and PPCD discharges with very strong reversal (e.g., $F \leq -0.5$) take maximum advantage of toroidal electric field reversal.

The first SDE-free periods occurred when PPCD was fired into a

pre-established EC period. Figure 7 shows a discharge in which such an SDE-free period occurred. During this period (~ 12 - 14 ms), the average Ohmic input power is about 1.4 MW (calculated with the polynomial function model, see discussion in Chapter 3), and the electron temperature increases, as indicated by the usual soft x-ray ratio. The density also increases substantially, while the H_α radiation decreases. The drop in H_α indicates that the particle source rate is probably dropping, even though there is a constant level of gas puffing. Thus, along with an increase in energy confinement time, there is an apparent increase in the particle confinement time.

The SDE amplitude changes dramatically before and after the SDE-free period. The SDE's are relatively subdued before PPCD, but they are quite large (evident in the Ohmic power and soft x-ray ratio) just after the SDE-free period. Their amplitude then drops steadily, however, as F becomes less negative following the PPCD pulse.

There are two other cases with PPCD in which clear variations in the SDE frequency have been observed. In its first incarnation, PPCD consisted of a single capacitor bank which drove a single large current pulse [6]. This single-pulse PPCD was accompanied by regular, large-amplitude SDE's. However, modeling indicated that penetration of the PPCD auxiliary current into the edge plasma would be made more efficacious (for current profile control) with multiple PPCD current pulses of smaller amplitude [7]. When multi-pulse PPCD was later implemented, one significant result was a reduced SDE repetition frequency, which helped to set a new RFP record for energy confinement time. This was accomplished with the toroidal electric field

sustained in its normal non-reversed direction. Variations in density have also been observed to affect the SDE frequency. In one set of experiments, PPCD was operated at low plasma current (200 kA) and low density (5×10^{12} cm^{-3}). At this density, SDE-free periods were common, but when the density was increased to 8×10^{12} cm^{-3}, the frequency of the SDE's increased as well.

SDE-free periods have also been observed in EC-only discharges, without PPCD. However, SDE-free periods longer than 1 ms occur only with reversal of the toroidal electric field, which in this case occurs near the end of the discharge. Normally, this electric field is sustained at a low positive value in the equilibrium phase of each discharge. To achieve a reversed electric field, the MST's poloidal field circuit is operated with only two small capacitor banks. Discharges in this mode of operation are only 20 - 25 ms long (compared to the 60 ms norm).

An example of a discharge in which the toroidal electric field reverses is shown in Fig. 8. The electric field is represented here by the surface toroidal voltage in Fig. 8(a). Note the voltage reversal at about 18 ms and the corresponding SDE-free period. The Ohmic power and electron temperature evolve in the same manner as in the SDE-free period of Fig. 7. The density is not shown in Fig. 8, but it remains constant with no gas puffing and a reduced particle source rate. As one can see in the Ohmic power, the SDE spacing before voltage reversal is significant ($\leq$ 1 ms) as well.

Also illustrated in Fig. 8 is that the reversal of the toroidal electric field does not immediately result in a rampdown of the plasma current. The same is true for the average toroidal magnetic field. In standard

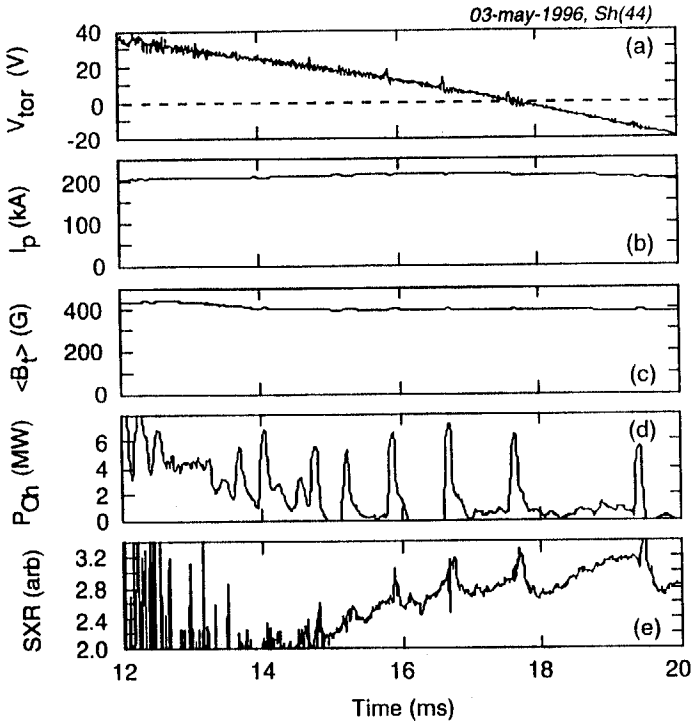

Fig. 8. (a) surface toroidal voltage, (b) toroidal plasma current, (c) cross-section-averaged toroidal magnetic field, (d) Ohmic input power, and (e) soft x-ray ratio during an EC discharge with a 2 ms SDE-free period.

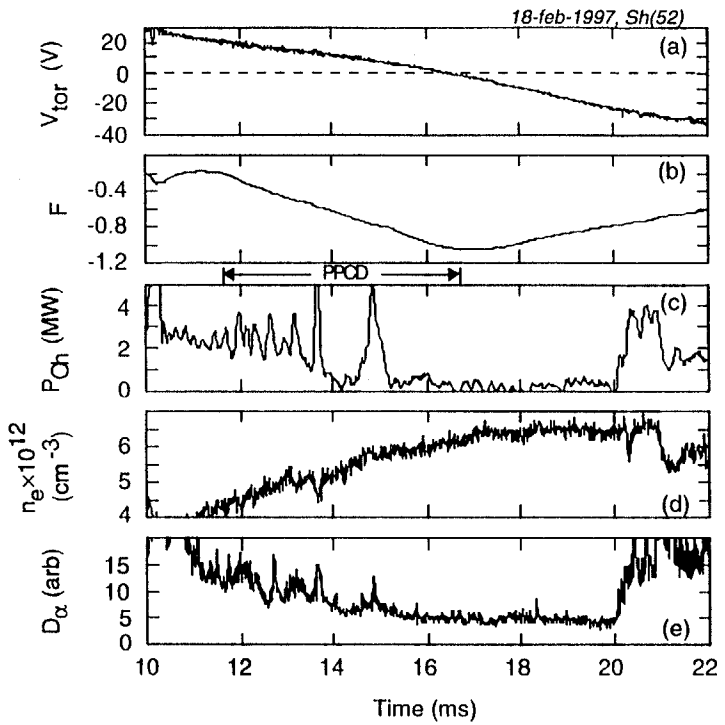

Fig. 9. (a) surface toroidal voltage, (b) reversal parameter, (c) Ohmic input power, (d) line-averaged density, and (e) neutral deuterium radiation during a PPCD discharge with a 5 ms SDE-free period. Soft x-ray data was not available for this shot.

confinement discharges, however, the plasma current and toroidal magnetic field do ramp down fairly quickly, presumably due to the higher plasma resistivity associated with standard confinement.

The longest SDE-free periods observed to date have occurred in discharges with PPCD plus reversal of the toroidal electric field. Such a discharge, with a 5 ms SDE-free period, is shown in Fig. 9. The SDE-free period begins during the PPCD pulse and continues well beyond it. The average Ohmic input power is a very low 0.2 MW (again calculated with the polynomial function model), and the density is sustained without puffing and with a decreased particle source rate (indicated by D_α

radiation).

Reversal of the toroidal electric field by no means guarantees the achievement of SDE-free periods. This was established in two sets of EC discharges in which the only difference, initially, was the condition of the plasma-facing wall. Both sets of discharges were at a plasma current of 200 kA and a line-averaged density of 5×10^{12} cm^{-3}. In the first set of discharges, the wall was well conditioned, and SDE-free periods were achievable at the usual EC toroidal magnetic field reversal of F = -0.5. The second set of discharges were produced several months later, and the condition of the plasma-facing wall had degraded. Attempts to produce SDE-free periods at F = -0.5 failed entirely. Then, keeping all else fixed, F was decreased to about -0.75. This resulted in an increase in the SDE amplitude, but it also brought about SDE-free periods.

This additional dependence of SDE suppression on toroidal magnetic field reversal and wall conditioning can be understood in the context of edge μ and/or pressure gradients. With relatively poor wall conditioning, impurity influx will keep the edge plasma cooler, potentially increasing gradients in the edge pressure and μ profiles. Dropping F to -0.75 increases the parallel current and Ohmic heating rate due to the reversed toroidal electric field. Thus, stronger magnetic field reversal may compensate for poor wall conditions.

5.2 Summary

In this chapter, I have described some of the characteristics of a new type of RFP discrete dynamo event. These small dynamo events,

like sawtooth crashes, correspond to a burst of parallel current and the generation of toroidal flux. However, in contrast to crashes, small dynamo events are relatively benign, and they appear first in edge-resonant modes, such as the (0,1), followed by an appearance in the m = 1 core-resonant modes. Since these events can apparently flatten the μ profile, they can potentially play a role in the reduction of the dominant m = 1 magnetic fluctuations. This possibility is explored in Chapter 6.

Small dynamo events can be controlled to some extent. Their amplitude is directly dependent on toroidal magnetic field reversal, and their frequency of occurrence depends, perhaps, on edge gradients of current density and pressure. Although they are less harmful than sawtooth crashes, small dynamo events still degrade confinement. There are several techniques by which small dynamo events can be suppressed, but it remains to be seen whether their suppression is due to favorable changes in the edge current or edge pressure gradient. Both or neither of these gradients may be important.

References

[1] Y. L. Ho, Nucl. Fusion **31**, 341 (1991).

[2] C. R. Sovinec, Ph.D. thesis, University of Wisconsin, Madison, Wisconsin, 1995.

[3] S. Ortolani and D. D. Schnack, Magnetohydrodynamics of Plasma Relaxation (World Scientific, Singapore, 1993).

[4] G. A. Chartas, Ph.D. thesis, University of Wisconsin, Madison, Wisconsin, 1991.

[5] H. Ji *et al.*, Phys. Rev. Lett. **73**, 668 (1994).

[6] J. S. Sarff *et al.*, Phys. Rev. Lett. **72**, 3670 (1994).

[7] J. S. Sarff *et al.*, Phys. Rev. Lett. **78**, 62 (1997).

6. Reduction of fluctuations

In this chapter, I will describe the reductions of both electrostatic and magnetic fluctuations observed in EC and PPCD discharges [1,2,3]. The m = 1 magnetic fluctuations are resonant in the plasma core but global in extent and have been identified as current-driven tearing modes [4]. The electrostatic fluctuations are located in the edge, but their source is not yet known. These fluctuations exhibit a reduction in the region of strong $\mathbf{E} \times \mathbf{B}$ flow shear and in the edge plasma beyond the shear region. The global magnetic fluctuations are, of course, reduced everywhere. The relative contribution to enhanced confinement from the reduction of each fluctuation is not yet known, but both reductions may be important.

Section 6.0 deals with the impact of electrostatic fluctuations on MST confinement and their reduction during EC and PPCD discharges. Section 6.1 covers the same aspects of magnetic fluctuations. This section also contains a discussion of the so-called single-helicity state, where the innermost resonant tearing mode grows to an enormous amplitude. In Sec. 6.2, I briefly discuss sawtooth crash suppression, and Sec. 6.3 contains the chapter summary.

6.0 Electrostatic fluctuations

Electrostatic fluctuations in the edge of the RFP occur at both low frequency (large scale length) and high frequency (small scale length). Their source has not been established, but there are several possibilities. These fluctuations may be, e.g., pressure-gradient-driven

resistive interchange turbulence or resistivity-gradient-driven rippling modes [4,5,6]. It is also possible that these fluctuations are not driven by local gradients, but by the global current-driven tearing modes, whose eigenfunctions (perturbative effects) extend into the edge. This possibility is suggested by measurements in the Extrap T1 RFP, which revealed a correlation between the core-resonsant tearing modes and the edge electrostatic fluctuations [7]. Data shown below suggests that there may also be such a correlation in the MST. Yet another possibility is based on the propogation of drift waves from the core to the edge. Mattor and Diamond [8] suggest that a drift wave originating in the core could propogate to the edge and be amplified in the process (i.e., the source of edge fluctuations is in the core). Some or all of these mechanisms may play a role in the RFP.

Electrostatic fluctuations can drive transport of particles and energy. In the MST, these fluctuations have been identified as the source of particle transport in the edge, but they do not account for energy transport, at least *directly* [9]. Electrostatic fluctuations can *indirectly* cause energy loss in the plasma edge and in the plasma core, as follows. Since electrostatic fluctuations drive particle transport in the edge, they govern, to some extent, the level of plasma-wall interaction. Plasma-wall interaction causes influx of fuel and impurity particles, which cool the edge plasma through radiation and collisional equilibration. Through radiation, impurities can also cool the plasma core. Thus, while electrostatic fluctuations do not govern energy transport, per se, they do play a role in energy confinement.

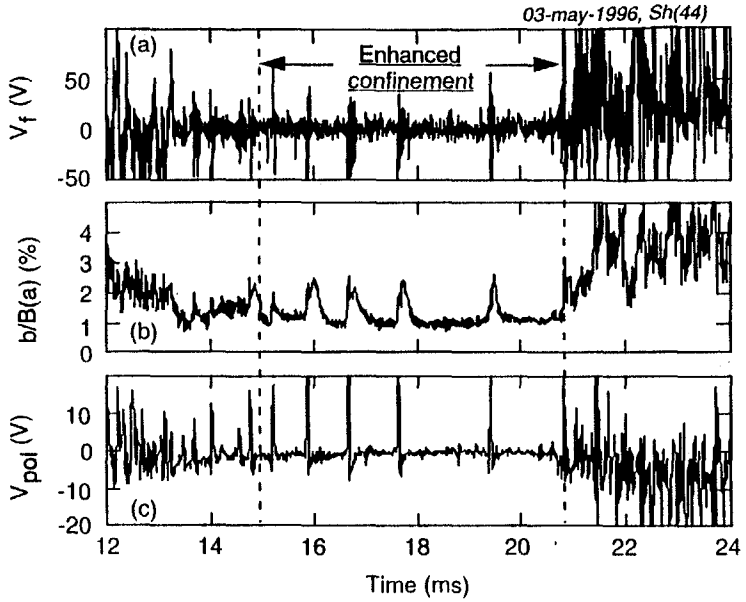

Fig. 1. (a) floating potential 2 cm from the plasma edge, (b) rms fluctuation in the poloidal magnetic field normalized to the total field at the edge, and (c) the surface poloidal voltage during a discharge with an EC period. The EC period is preceded by a transition phase during which fluctuations are gradually reduced. Each burst during the EC period is a small dynamo event.

6.0.0 Electrostatic fluctuations in EC and PPCD discharges

During EC and PPCD discharges, electrostatic fluctuations are reduced in the shear region and over the entire plasma edge. To first illustrate the reduction of electrostatic fluctuations, the time evolution of the floating potential 2 cm from the plasma edge during an EC period is shown in Fig. 1. In anticipation of the discussion in Sec. 6.1, I also

plot the normalized rms fluctuation in the poloidal magnetic field to show its coincident reduction. The fluctuation reduction during the EC period is also apparent in the surface poloidal voltage, which responds to changes in the toroidal magnetic field in the plasma. Note that small dynamo events cause a brief increase in the fluctuation amplitude in all three quantities. The impact of small dynamo events on fluctuations is discussed in more detail below. The phenomonology illustrated in Fig. 1, including the coincident reduction of electrostatic and magnetic fluctuations, is very similar to that in PPCD discharges (see Fig. 2 of Ref. 3).

To illustrate more clearly the reduction of electrostatic fluctuations during EC periods, three fluctuation power spectra measured 2 cm from the plasma edge are shown in Fig. 2. These spectra are calculated from fixed-length (1.024 ms) time windows chosen to avoid sawtooth crashes, and they are ensemble averaged. The non-EC spectrum in Fig. 2 is calculated from periods of standard confinement in strongly reversed discharges (e.g., before and after the EC period shown in Fig. 1). One of the EC spectra in Fig. 2 includes small dynamo events (SDE's), while the other excludes them. The latter spectrum, calculated from SDE-free periods, averages over only four individual spectra and is fairly noisy. The other two spectra in Fig. 2 are an ensemble of between 20 – 30 individual spectra. The small number of spectra comprising the SDE-free spectrum is due to the relative scarcity of SDE-free periods when a probe is inserted into the plasma. When a probe is inserted more than 6 cm from the plasma

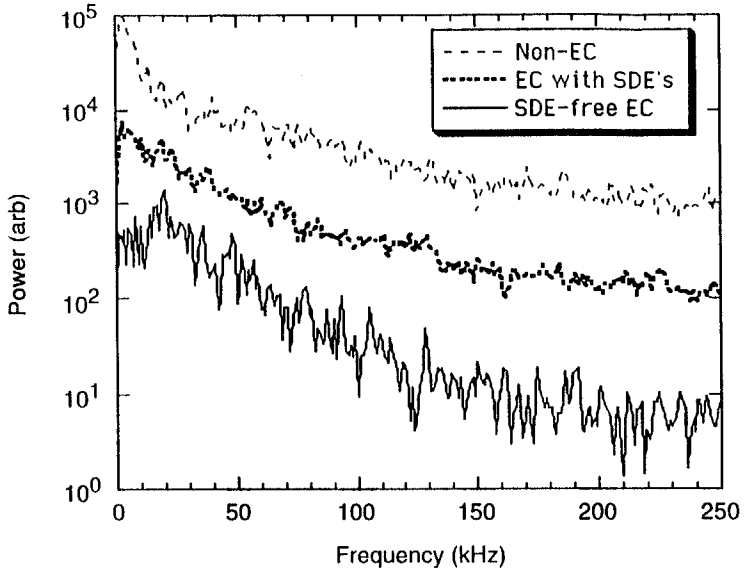

Fig. 2. Fluctuation power spectra calculated from the floating potential measured 2 cm from the plasma edge. The spectra are calculated from different time windows in the same strongly reversed discharges.

edge (just outside the $\mathbf{E} \times \mathbf{B}$ flow shear region in these discharges), no SDE-free periods occur.

The fluctuation power in Fig. 2 varies by about a factor of 10 or more between spectra, with the largest difference occurring at high frequency. In addition, the reduction of fluctuation power from case to case is broadband, encompassing the entire frequency range. The difference between the two EC spectra may be due entirely to SDE's. As

was shown in Fig. 1, each SDE causes a large momentary increase in the fluctuation power, and given the relatively low level of fluctuations between SDE's, each SDE probably dominates any power spectrum in which it is included. This has important implications for future measurements of fluctuation-induced transport in EC and PPCD discharges, e.g., particle and energy transport due to electrostatic fluctuations in the region of strong $\mathbf{E} \times \mathbf{B}$ flow shear.

Note the local maximum in the SDE-free spectrum at 20 kHz, which is the dominant frequency of the global tearing modes. This feature is only observed in SDE-free spectra, when the contribution of SDE's is removed. Deeper inside the plasma, the SDE-free fluctuation power increases at all frequencies, and this 20 kHz feature is washed out. The signature of the dominant tearing modes in the edge electrostatic fluctuations was also observed in the Extrap T1 RFP [7].

By integrating the ensemble power spectra at each radius, one derives the profiles of the EC and standard (or non-EC) total fluctuation power. Such profiles are shown in Fig. 3(a), in addition to the profile of the EC radial electric field from Chapter 4. Immediately obvious from the EC profile (which includes SDE's) is the reduction of fluctuations over the entire edge, along with an extra reduction in the region of strong shear. Reduction of fluctuations in the region of strong shear is, of course, the hallmark of H-mode discharges [10]. Further, there are several observations in H-mode discharges of reduced fluctuations beyond the shear region [11,12].

There are two local reductions in the standard-discharge fluctuation power profile in the shear region. If these dips are not just

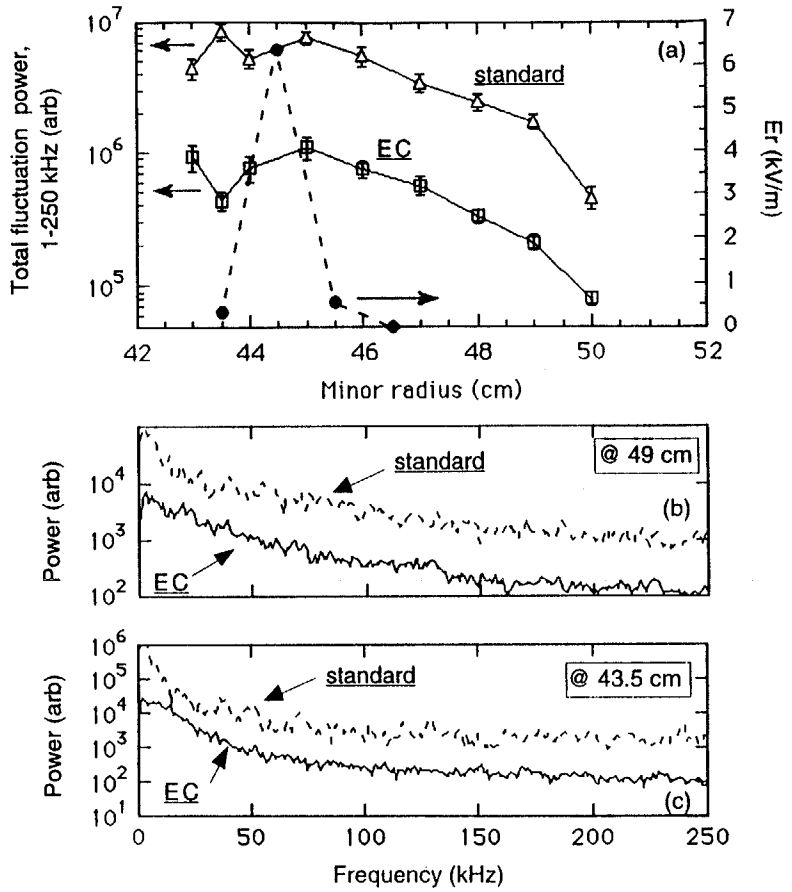

Fig. 3. (a) profiles of the EC radial electric field and total fluctuation power in the floating potential, (b) EC and standard power spectra at 49 cm, and (c) EC and standard power spectra at 43.5 cm. Spectra are frequency-integrated to derive the total fluctuation power in (a). Here, "standard" refers to low confinement periods of strongly reversed discharges. The plasma edge is at 51 cm.

random variations, they may arise from the EC data selection technique. Because the MST lacks the diagnostics to measure the radial electric field profile in a single discharge, only global data, such as the Ohmic input power, is available for selection of EC periods. One can identify high quality EC periods without ambiguity, but choosing non-EC periods is not as simple. It is conceivable for a discharge to have strong $\mathbf{E} \times \mathbf{B}$ flow shear and local fluctuation reduction without an EC-like reduction in the Ohmic input power. This could be due, e.g., to a larger-than-normal level of plasma-wall interaction brought on by a field error. Discharges like this that are included in the non-EC ensemble might produce the profile in Fig. 3.

Four of the ensemble power spectra that comprise the integrated data points in Fig. 3(a) are shown in Figs. 3(b) and 3(c). The spectra in Fig. 3(b) are the same as those in Fig. 2. The spectra in Fig. 3(c) illustrate that, like the case at 49 cm, the EC fluctuation reduction is also broadband at 43.5 cm (the point of minimum fluctuation power in the shear region). Note as well that the two spectra at each radial location differ slightly less at low frequency than at high frequency.

The profile of integrated fluctuation power for PPCD (Fig. 4) is roughly similar to that for EC periods. Fig. 4 also contains the PPCD radial electric field profile from Chapter 4 and the integrated fluctuation power profile for weakly reversed (standard) discharges. The fluctuation power profiles in this figure are from power spectra with a bandwidth of only 40 kHz, so these profiles cannot be compared quantitatively to those of Fig. 3. The standard fluctuation power profile in Fig. 4 does include (statistical) error bars, but they are quite small.

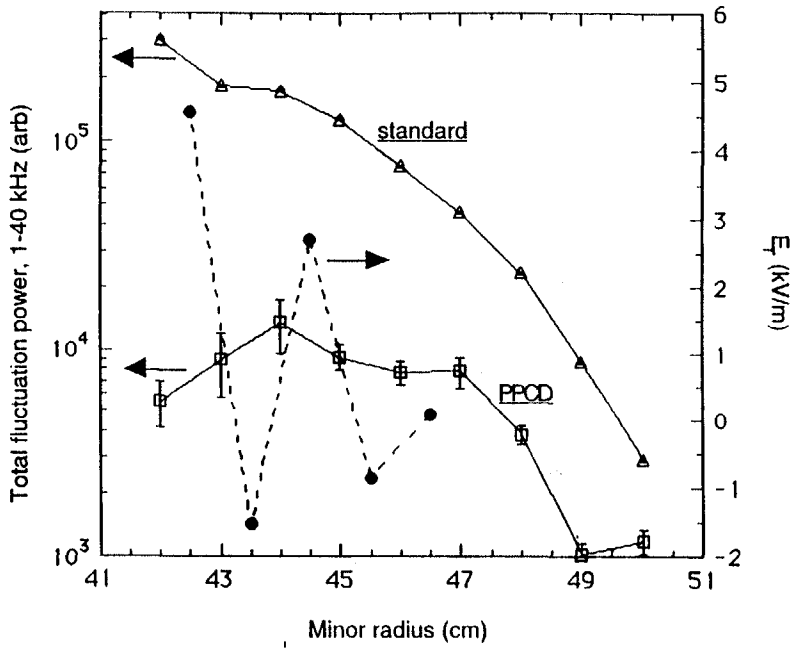

Fig. 4. Profiles of the PPCD radial electric field and total fluctuation power in the floating potential. Here, "standard" refers to low confinement weakly reversed discharges. Note the smaller bandwidth here as compared to that in Fig. 3 for EC discharges.

Note as well that this profile decreases smoothly with radius. With weakly reversed discharges, there is no possibility for ambiguity as there was for Fig. 3(a).

During PPCD, the radial electric field has more structure than it does during EC periods, and while the gradients appears to be largest from roughly 42 – 45 cm, one does not observe a local reduction of

fluctuations like that in EC discharges. Instead, the fluctuation power simply tapers off inside of 44 cm. As with EC periods, however, the power spectra (not shown) during PPCD reveal a broadband fluctuation reduction.

The PPCD fluctuation power profile in Fig. 4 is comprised only of power spectra from SDE-free periods. As illustrated by the two EC spectra in Fig. 2, SDE's have a large impact on the fluctuation power. In the case of PPCD, where SDE's are typically more violent, the effect on the fluctuation power is more dramatic. A PPCD fluctuation power profile was compiled for the same discharges used in Fig. 4, but from power spectra including SDE's. This resulted in an increase in the total fluctuation power at each radial location and a profile shape similar to that in Fig. 4 for weakly reversed discharges (i.e., the fluctuation power continues to increase beyond 44 cm).

The edge reduction of electrostatic fluctuations in EC and PPCD discharges suggests the possibility of an improvement in edge confinement. However, transport of particles and energy by electrostatic fluctuations is governed by correlated pairs of fluctuating quantities, e.g., the density and perpendicular electric field in the case of particle transport [5,9]. The rate of transport depends on the fluctuation amplitudes, but it also depends on the phase angle between the paired fluctuations, which we have not yet measured. Thus, the reduction of electrostatic fluctuation amplitudes presented here does not guarantee reduced transport.

Assuming for the moment that transport is reduced, one wonders if the local fluctuation reduction in the strong shear region actually

matters relative to the reduction over the rest of the plasma edge. Can the entire edge region act as a barrier to transport? Given the steepening in the EC and PPCD profiles of the ion saturation current ($\sim n_e T_e^{1/2}$), presented in Chapter 4, both the regions within and beyond the strong shear may indeed play a role.

6.0.1 Possible causes of electrostatic fluctuation reduction

There are several possible mechanisms by which the electrostatic fluctuations in the edge plasma are reduced during EC and PPCD discharges. These fluctuations include those of low frequency (long wavelength) and high frequency (short wavelength). The local reduction of fluctuations in the region of strong $\mathbf{E} \times \mathbf{B}$ flow shear in EC discharges suggests that the shear may affect both the long and short wavelength fluctuations in that region. A similar explanation may apply to PPCD, but the relationship between the reduced fluctuations and the strong shear is not clear (Fig. 4). In both types of discharge, the shear may affect long wavelength fluctuations beyond the shear region. However, mechanisms other than the $\mathbf{E} \times \mathbf{B}$ flow shear must be invoked to explain the reduction of short wavelength fluctuations beyond the shear region.

The reduction of fluctuations by strong $\mathbf{E} \times \mathbf{B}$ flow shear was first discussed by Biglari *et al.* [13]. Recall that shear in the $\mathbf{E} \times \mathbf{B}$ flow is considered "strong" if the associated shearing rate is larger than the decorrelation rate of the ambient turbulence in the absence of $\mathbf{E} \times \mathbf{B}$ shear. Roughly speaking, when this criterion is satisfied, reduction of fluctuations can occur. The shearing rate for EC discharges, $\sim 7 \times 10^6$/s,

was calculated in Chapter 4. The ambient turbulence decorrelation rate can be estimated from the full width at half maximum of the standard power spectrum at 43.5 cm [Fig. 3(c)]. The width of this spectrum gives a decorrelation rate of about 3×10^5/s. Thus, EC periods are well within the strong shear regime. The PPCD shearing rate is comparable to that of EC periods. Thus, PPCD is also in the strong $\mathbf{E} \times \mathbf{B}$ flow shear regime.

The reduction of high frequency, short-correlation-length fluctuations lying within a localized region of flow shear is predicted analytically in the literature, e.g., Ref. 13. However, to my knowledge, no analytical work has been done regarding low frequency fluctuations, whose correlation lengths extend well beyond the shear region. In standard, weakly reversed discharges in the MST, low frequency (< 30 kHz) floating potential fluctuations have a correlation length of ~ 10 cm [14], substantially larger than the width of the $\mathbf{E} \times \mathbf{B}$ flow shear region.

Despite the lack of analytical theory, the reduction of long wavelength fluctuations by local shear is conceivable and can be understood as follows. To maintain coherence, the various regions of a turbulent eddy (fluctuation) of any size (correlation length) must communicate with each other. If a localized region of $\mathbf{E} \times \mathbf{B}$ flow shear develops at a radius somewhere within this eddy, intra-eddy communication will likely be diminished, and the eddy may even be split into two distinct regions. Thus, the original eddy's correlation length will be reduced, which translates [13] to a reduction of amplitude and potentially the transport it causes (see discussion in Chapter 2).

The preceding discussion applies to any fluctuations or eddies that overlap the region of strong shear. Thus, in EC and PPCD discharges,

long wavelength fluctuations beyond the shear region (at a larger minor radius) can be affected by the shear. However, the explanation falls short of explaining the reduction of short wavelength fluctuations beyond the shear region. These fluctuations do not overlap the shear region and are, therefore, not directly affected by it. Still, there are several nonexclusive mechanisms that can account for the reduction of these fluctuations, and these mechanisms can influence the long wavelength fluctuations as well.

Several explanations are suggested based on observations of fluctuation reduction beyond the shear region in H-mode discharges [11,12]. One of the simplest is that the edge pressure and/or resistivity gradients may be reduced during EC and PPCD discharges. From the ion saturation current profiles in Chapter 4, however, a reduction in the pressure gradient seems unlikely. A similar explanation is that, assuming the $\mathbf{E} \times \mathbf{B}$ flow shear region provides a barrier to transport, it might also reduce the fluctuations in the particle and energy flux passing through it, thereby reducing fluctuations they would normally induce beyond the barrier.

Another explanation rests on the observation [7] in the Extrap T1 RFP that low and high frequency floating potential fluctuations in the edge are nonlinearly coupled [15], meaning that energy can be transferred between them. If the same is true in the MST, then the reduction of the short wavelength fluctuations may be facilitated by the reduction of the long wavelength fluctuations, and this can occur in at least two ways. The long wavelength fluctuations overlapping the $\mathbf{E} \times \mathbf{B}$ flow shear region can be reduced directly by the shear as described

above. Further, if the long wavelength electrostatic fluctuations are driven at all by the global *magnetic* fluctuations (suggested by the SDE-free spectrum in Fig. 2), then magnetic fluctuation reduction (see next section) will allow reduction of the electrostatic fluctuations. If the long wavelength edge fluctuations are reduced, then nonlinear coupling may effect a reduction in the fluctuations at shorter wavelength.

Yet another explanation is based on the idea proposed by Mattor and Diamond [8]. They postulated that edge turbulence could be driven entirely by the outward propogation and amplification of drift waves from the core. They also state the possibility that edge flow shear can prevent propogation of these waves, essentially isolating the edge plasma from core fluctuations. This idea is distinct from the paradigm of local fluctuation reduction by $\mathbf{E} \times \mathbf{B}$ flow shear.

6.1 Magnetic fluctuations

Tearing modes [4] have been identified as the dominant source of magnetic fluctuations in the RFP. Tearing modes are driven primarily by gradients in the $\mu = \mu_0 \mathbf{J}\cdot\mathbf{B}/B^2$ and pressure profiles [16,17]. Between sawtooth crashes, only the core-resonant tearing modes are of significant amplitude, but during each crash, the amplitudes of all modes, including those resonant at the edge, increase dramatically. The edge-resonant modes are driven by nonlinear coupling at the crash [15,18].

Confinement is generally poorest during sawtooth crashes, due in part to the large magnetic fluctuations, but these fluctuations also play an important role between sawtooth crashes. Magnetic fluctuations

have been measured to account for both particle [19] and energy [20] transport in the plasma core. Between and during sawtooth crashes, the relatively large magnetic fluctuation amplitudes cause the formation and overlap of adjacent magnetic islands, thereby stochasticizing the plasma core. Energy transport in this case is governed by stochastic diffusion [21].

6.1.0 Magnetic fluctuations in EC and PPCD discharges

Reduction of magnetic fluctuations continues to be a major goal of the MST program. With the implementation of PPCD, this goal was achieved, although there may still be room for further reduction [2,3]. Figure 5 illustrates the effect of PPCD on the normalized rms fluctuation in the poloidal magnetic field. During the PPCD pulse, and for a few ms following the pulse, the rms fluctuation amplitude reaches about 1%, which is quite low and very close to the record of 0.8% reported earlier for PPCD discharges [3]. Note that this discharge also utilizes reversal of the toroidal electric field, discussed in Chapter 5. The dominant contributors to the poloidal magnetic field fluctuations include the core-resonant modes, with poloidal mode number m = 1 and toroidal mode numbers n = 6 – 10, and the edge-resonant modes, such as the (m,n) = (0,1). The (0,1) is resonant at the reversal radius, across which the toroidal magnetic field reverses direction.

As discussed in Chapter 5, each SDE (in both PPCD and EC discharges), causes a momentary increase in the mode amplitudes. Each SDE first appears in the edge-resonant modes, dominated by the (0,1). It then appears in the core-resonant modes, dominated by the (1,6).

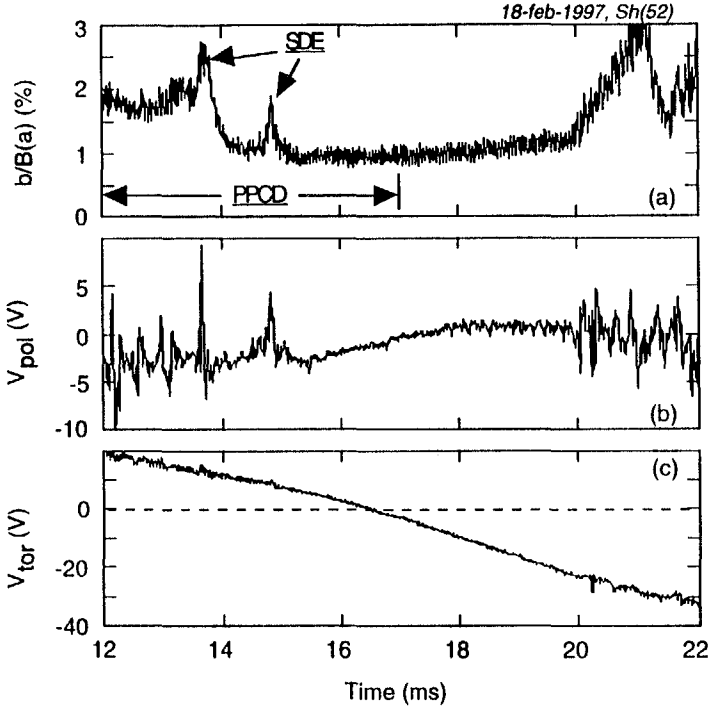

Fig. 5. (a) rms fluctuation in the poloidal magnetic field normalized to the total field at the edge, (b) surface poloidal voltage, and (c) surface toroidal voltage during a discharge with PPCD. The period of reduced magnetic fluctuations lasts 3 ms beyond the end of the PPCD pulse. This is the same discharge as was shown in Fig. 9 of Chapter 5.

There are two SDE's indicated in the discharge in Fig. 5. This discharge is fairly remarkable in that it has a 5 ms SDE-free period. *All periods of reduced magnetic fluctuations are characterized by the absence of SDE's.*

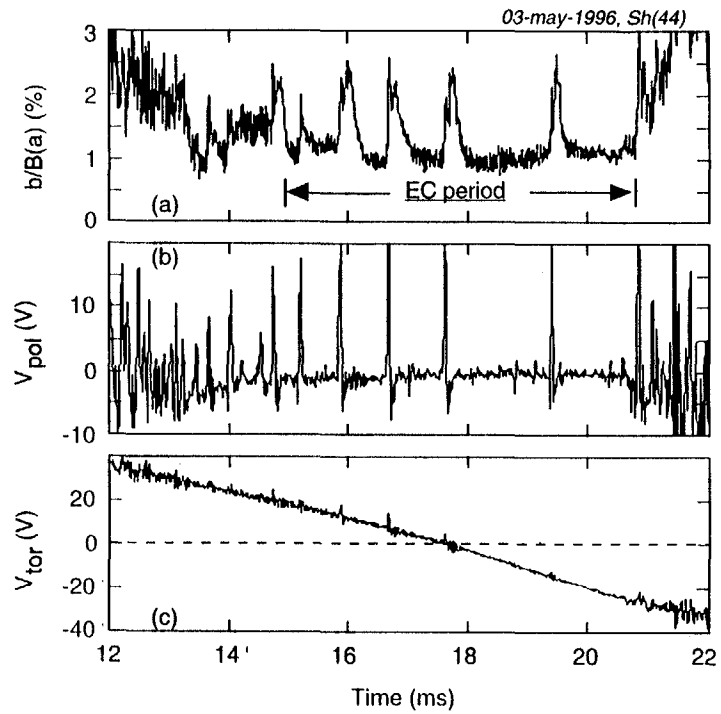

Fig. 6. (a) rms fluctuation in the poloidal magnetic field normalized to the total field at the edge, (b) surface poloidal voltage, and (c) surface toroidal voltage during a discharge with an EC period. This is the same discharge as was shown in Fig. 1 of this chapter and in Fig. 8 of Chapter 5.

However, the absence of SDE's does not guarantee reduced magnetic fluctuations.

Following the achievement of reduced magnetic fluctuations with PPCD, a similar reduction was achieved during EC periods. However, the

reduction in EC periods does not *require* current-profile-flattening auxiliary current, implying that some additional mechanism(s) must be at work (discussed later in this section). An EC discharge with multiple periods of reduced magnetic fluctuations is shown in Fig. 6. Between SDE's, which punctuate the entire EC period, the rms fluctuation in the poloidal field reaches about 1%, similar to the PPCD discharge in Fig. 5. As I illustrated in Chapter 5, the maximum spacing of SDE's during EC periods has thus far been limited to about 2 ms. Therefore, periods of reduced magnetic fluctuations in EC discharges are also limited to 2 ms.

6.1.1 Single helicity mode spectrum

In sharp contrast to the discharges in Figs. 5 and 6, EC and PPCD discharges occasionally enter a state in which the innermost resonant tearing mode, the (1,6), reaches a very large amplitude, while the other resonant modes remain small. This is referred to as "single helicity" as only one mode or one (m,n) combination dominates the mode spectrum.

A single helicity EC discharge is shown in Fig. 7. The EC period lasts from 13 – 18 ms. Based on the rms fluctuation level in the poloidal magnetic field, this EC period starts out at a low fluctuation level (~ 1%), but the rms fluctuation level increases by a factor of three. The n = 6 amplitude reaches ~ 23 G by the end of the EC period, then falls off rapidly. A rough calculation shows that the magnetic island associated with the (1,6) could span up to one half of the plasma cross section at maximum mode amplitude. The only other mode of significant amplitude during this period is the (1,7), reaching ~ 8 G when the (1,6) amplitude peaks. A sawtooth crash (evident in the

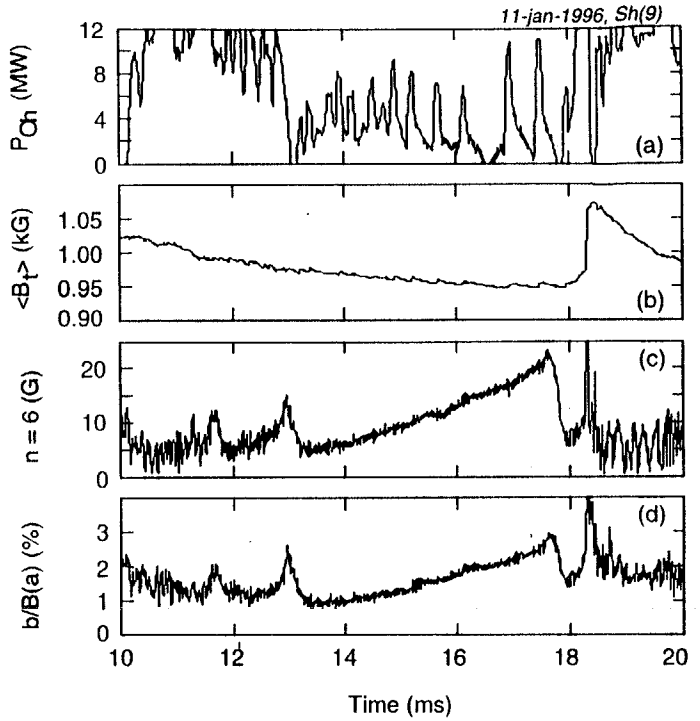

Fig. 7. (a) Ohmic input power, (b) cross-section-averaged toroidal magnetic field, (c) m=1, n=6 mode amplitude, and (d) rms fluctuation in the poloidal magnetic field normalized to the total field at the edge during an EC discharge. The rms fluctuation is comprised of toroidal mode numbers n=1 to n=14.

average toroidal magnetic field) arrives about 0.5 ms *after the fall of the n = 6 amplitude*. This is unexpected, as the crash would normally occur at some point during the growth phase of the (1,6).

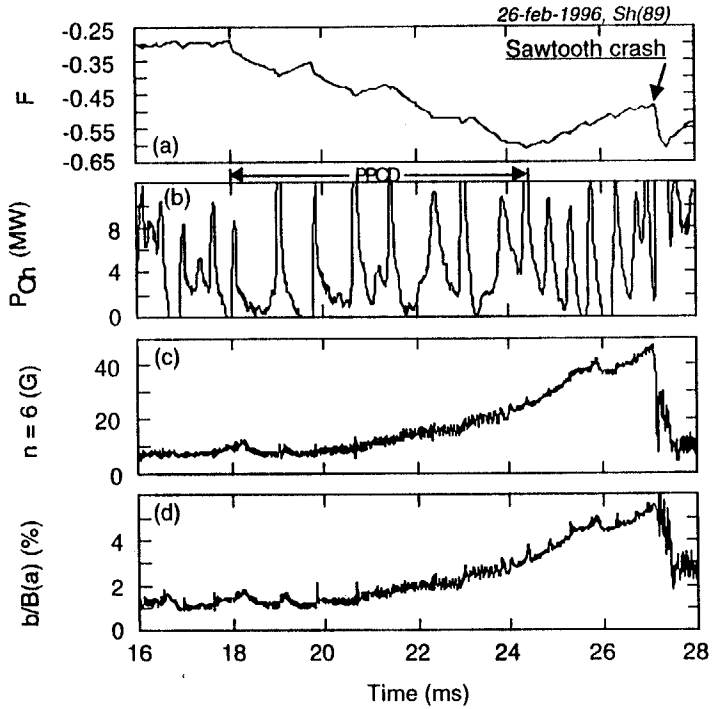

Fig. 8. (a) reversal parameter, (b) Ohmic input power, (c) m=1, n=6 mode amplitude, and (d) rms fluctuation in the poloidal magnetic field normalized to the total field at the edge during a discharge with PPCD. This discharge locks at 24 ms.

This single helicity behavior occurs in a similar fashion with PPCD. An example is shown in Fig. 8. In this discharge, there is a series of PPCD pulses lasting ~ 1 ms each, spanning 18 – 24 ms. The PPCD phase is preceded by a brief EC period. In this example, the (1,6) amplitude

reaches the rather staggering amplitude of > 45 G, while the (1,7), the next largest mode, remains at an amplitude of ≤ 5 G. A sawtooth crash occurs at almost the same time the (1,6) amplitude falls off sharply.

Magnetic fluctuations and energy confinement are usually anti-correlated. Thus, the behavior of the Ohmic power in Figs. 7 and 8 is, perhaps, somewhat surprising (the soft x-ray ratio was not available for these discharges). One important contributor to the Ohmic input power is the anomalous, non-Spitzer component [22], which one expects to increase with magnetic fluctuation amplitude. From 14 – 17 ms in Fig. 7, the Ohmic power decreases while the n = 6 amplitude increases. From 17 – 18 ms, the average Ohmic power is somewhat larger, but apparently only due to the increased SDE amplitudes. Between SDE's, the Ohmic power is quite low. Similarly, the Ohmic input power and magnetic fluctuations in Fig. 8 seem to behave independent of one another. From 25 – 26 ms, just as the rms poloidal field fluctuation reaches about 5%, the average Ohmic power remains fairly constant.

One mode at large amplitude may not cause significant confinement degradation, however. The degree of magnetic stochasticity and transport in a given discharge depends in part on how fluctuation power is distributed among the dominant modes. For example, a single mode containing all of the available fluctuation power (single helicity) will generally cause less transport than a group of modes with the same total fluctuation power. In the latter case, it is assumed that each mode's resonant surface is spatially separated from the others' (i.e., they are distributed across the plasma). Due to this distribution, the radial magnetic perturbation from the group of modes

can cause stochasticity over more of the discharge, thereby leading to larger net transport. In essence, the difference between the two cases is geometric.

There is another possible explanation for the apparent lack of Ohmic power dependence on the single helicity mode amplitude. Simply put, the decrease in the Spitzer component of the Ohmic power may be enough to offset the increase in the anomalous component. If this is not the case, then in the single helicity state at least, global confinement may not be determined by the plasma core. As I described in Chapter 2, a similar result was found in H-mode discharges in DIII-D [23,24]. It was verified that the H-mode confinement improvement was governed by the fluctuation reduction in the edge and was not significantly affected by *increases* in magnetic fluctuations in the core. Determining if this is the case in the MST requires further measurements.

What causes the single helicity state? To my knowledge, it only occurs during EC and PPCD discharges, thus pointing to some unique aspect of these discharges. One possibility is that the SDE's and their effect on the current profile are responsible. In Chapter 5, I demonstrated that the (1,6) amplitude increased with each SDE, then fell off. It might be possible that SDE's in some discharges act only to "pump up" the (1,6). Looking in detail at the discharges in Figs. 7 and 8, this is certainly a possibility.

6.1.2 Possible causes of magnetic fluctuation reduction

In this section, several possible explanations are presented for the

reduction of magnetic fluctuations in EC and PPCD discharges. The explanations fall into two basic categories. In the first category are explanations based on active or passive manipulation of the $\mu = \mu_o \mathbf{J}\cdot\mathbf{B}/B^2$ profile. Gradients in this profile are believed to play a critical role in determining the amplitude of the dominant magnetic fluctuations. Thus, by driving auxiliary current or changing the resistivity profile, for example, one can affect magnetic fluctuations. In the context of gradients affecting magnetic fluctuations, I also briefly mention a possible explanation for the fluctuation reduction based on changes in the core pressure gradient.

In the second category are fluctuation reduction mechanisms based on sheared rotation, including $\mathbf{E} \times \mathbf{B}$ flow shear. There is very little RFP-specific theoretical work describing the interaction of shear flow and global magnetic fluctuations. Thus, I will comment on this second category only briefly. Note that fluctuation reduction mechanisms based on current profile control need not be exclusive of those based on flow shear.

Magnetohydrodynamic (MHD) modeling has suggested that auxiliary parallel (approximately poloidal) current driven in the plasma edge, specifically in the region $0.6 \le r/a \le 0.8$, can flatten the $\mu = \mu_o \mathbf{J}\cdot\mathbf{B}/B^2$ profile and reduce the core-resonant magnetic fluctuations [17,25]. It has also been suggested that the necessary current could be driven inductively [25]. Thus, PPCD (pulsed poloidal current drive) was implemented, resulting in a significant reduction of magnetic fluctuations and a factor of 4 - 5 improvement in the energy confinement time [3].

One might reasonably presume that PPCD is simply working as suggested by the modeling. However, the achievement of magnetic fluctuation reduction in EC discharges [1], without auxiliary current drive, suggests that auxiliary current drive may not be acting alone. As has been demonstrated in several chapters, EC and PPCD discharges are similar in many respects, and the reduction of magnetic fluctuations in each case occurs with the same basic phenomenology. Thus, while the auxiliary current in PPCD may be acting as predicted, there are apparently additional mechanisms at work, and these mechanisms are likely common to both EC and PPCD discharges.

An example of magnetic fluctuation reduction during an EC period was shown in Fig. 6. This EC period is accompanied by reversal of the toroidal electric field at ~ 18 ms. As discussed in Chapter 5, reversal of the toroidal electric field increases the parallel current in the edge, and it may also decrease the parallel current in the core. Thus, toroidal electric field reversal constitutes auxiliary current drive. However, the magnetic fluctuation reduction in this EC period does not depend on this current drive. There are two (< 1 ms) periods of reduced magnetic fluctuations *before* the electric field reverses, and I have observed similar brief periods of reduced fluctuations in "normal" EC discharges where the toroidal electric field is nonreversed throughout.

After the toroidal electric field reverses (Fig. 6), the (reduced) magnetic fluctuation amplitude does not change, but the time between small dynamo events is increased, allowing a ~ 2 ms period of reduced fluctuations. Thus, while reversal of the toroidal electric field may help reduce magnetic fluctuations, I believe that it is also important in its

ability to increase SDE spacing. This allows longer periods of reduced fluctuations. Likewise, I believe that SDE suppression may also be an important component of PPCD. Therefore, instead of, or in addition to, an explanation based on auxiliary current drive, one must search for some common aspect of EC and PPCD discharges to account for magnetic fluctuation reduction. There are several nonexclusive possibilities.

Based on the standard model for magnetic fluctuation reduction, SDE's are the first logical candidate. Chapter 5 illustrates that SDE's, like sawtooth crashes, correspond to bursts of parallel current, thereby allowing them to flatten the μ profile. Thus, although SDE's are absent during periods of reduced fluctuations, they may act as the progenitors of these periods. As shown in Chapter 5, each SDE clearly has an effect on the core-resonant m = 1 modes. The *edge* current driven with each SDE is able to affect the *core*-resonant modes, because these modes are global. In other words, their eigenfunctions span most of the plasma cross section [26,27,28]. These modes can be destabilized by $\mu(r)$ gradients in the edge, and they can be stabilized when these gradients are removed [17,25].

There are two questions that arise in connection with the SDE hypothesis. One must ask why, before dropping to low amplitude, the m = 1 modes increase for a brief time with each SDE. One must also wonder how periods of reduced fluctuations are sustained up to 5 ms following SDE's lasting only a fraction of a millisecond. One would expect the brief SDE current pulse to diffuse away more rapidly than this. I will return to these questions later, but now I discuss other possible mechanisms for magnetic fluctuation reduction.

Another possible fluctuation reduction mechanism in the current profile control category stems from the decreased Spitzer resistivity ($\propto Z_{eff}T_e^{-3/2}$) in the edge plasma during EC and PPCD discharges. The change in edge temperature, if any, is not known, but Z_{eff} almost certainly decreases. Observations in the Extrap T1 RFP [29] revealed a resistivity dependence of the magnetic fluctuation level and anomalous (non-Spitzer) Ohmic input power [22]. As the edge resistivity increased, the magnetic fluctation level, dominated by core-resonant m = 1 and edge-resonant m = 0 modes, also increased. This in turn led to an increase in anomalous input power. It was also observed that reversal of the toroidal magnetic field decreased, and this was interpreted as being due to a decrease in $\mu = \mu_o \mathbf{J}\cdot\mathbf{B}/B^2$ in the edge.

The DEBS 3D MHD code was employed to model this situation [29,30]. The edge resistivity profile was cast as $\eta(r) \sim [1 + 9(r/a)^{\gamma}]^2$, giving a resistivity profile strongly peaked in the edge. Varying γ from 30 to 10 (i.e., increasing the magnitude of and broadening the edge resistivity profile), the magnetic fluctuation energy, δB_r^2, increased by a factor of two, associated with the need for a larger dynamo electric field, $\mathbf{E}_f = -\langle \mathbf{v} \times \mathbf{b} \rangle$, to compensate for the increased edge resistivity ($\mathbf{v}$ and $\mathbf{b}$ represent velocity and magnetic fluctuations). However, instead of remaining constant or becoming more negative, F changed from -0.26 (at γ = 30) to -0.12 (at γ = 10), resulting from a reduction of μ in the edge.

The increased fluctuation level can be interpreted as a reduction in the dynamo efficiency [31]. The dynamo exists primarily because of gradients in $\mu(r)$, and it seeks to reduce these gradients through $\mathbf{E}_f$.

Therefore, in the case of EC and PPCD discharges, the reduced edge resistivity may allow more efficient dynamo current drive, which, for a given current gradient, allows for a reduction in the fluctuations that drive the current. In other words, with reduced resistivity, a lower level of fluctuations can drive the same stabilizing current. In addition to the reduction of magnetic fluctuations, a reduction of velocity fluctuations during PPCD has also been observed [32].

The preceding discussion embodies to some extent the concept of S-scaling of magnetic fluctuations (S is the Lundquist number = τ_r/τ_a. τ_r is the resistive diffusion time $\propto 1/\eta$, and τ_a is the Alfvén time). For a fixed τ_a, S increases with decreasing resistivity. Much experimental and theoretical work has been devoted to the scaling of magnetic fluctuation amplitude with S. Recent work indicates that the amplitude should scale roughly as $S^{-1/4}$ [17,33], meaning that as the plasma resistivity decreases, so should magnetic fluctuations. There is not yet a database of fluctuation amplitude versus S for EC or PPCD discharges, but the scaling is qualitatively consistent with the experimental results.

Often discussed in tandem with the effects of a parallel current gradient are the effects of a pressure gradient. According to linear theory in cylindrical geometry [16], tearing modes are always unstable in the presence of a pressure gradient, dP/dr < 0. In simulations, Sovinec [17] examined the contribution made by a typical pressure gradient to m = 1 instability. While typically less than that of the typical current gradient, the pressure contribution is still significant. Recall Fig. 5 of Chapter 5, which contains the electron density profile between SDE's during an EC period (PPCD exhibits a similar profile

shape). This profile, which may approximate the shape of the pressure profile, is quite flat over much of the cross section, and may account for the fluctuation reduction. However, to within the approximately 8 cm spatial resolution of the measurement, the density profile in standard, weakly reversed discharges is also fairly flat, without magnetic fluctuation reduction [3]. This weakens the pressure gradient hypothesis. Of course, there may be local, undetected density (pressure) gradients in both cases. Validation of this hypothesis awaits detailed measurements of the pressure profile.

The direct interaction of magnetic fluctuations and strong $\mathbf{E} \times \mathbf{B}$ flow shear may be yet another means of explaining the observed fluctuation reduction. The tearing mode has a complicated structure, however. In addition to its global eigenfunction, the tearing mode consists of a small "resistive layer" and a larger island region, both centered on the mode resonant surface [34]. It is the eigenfunction that overlaps the region of strong shear in EC and PPCD discharges. While current gradients far from the resonant surface can affect the mode amplitude, it is not known (to my knowledge) if $\mathbf{E} \times \mathbf{B}$ flow shear can as well. Along this line of thought, I previously discussed the possibility that electrostatic fluctuations in the edge could be reduced by a reduction in global magnetic fluctuations. In turn, can magnetic fluctuations be affected by electrostatic fluctuations?

The effect of flow and flow shear (but not necessarily $\mathbf{E} \times \mathbf{B}$ flow shear) on tearing modes has been studied theoretically for a number of years, starting well before the discovery of the H-mode, but this work has focused on flow and flow shear present within and around the

mode's thin resistive layer and/or the mode's island. Persson [35] summarizes some of the work that has demonstrated numerically and/or analytically that a sheared mass flow can change the linear stability of a tearing mode. A weakly sheared flow parallel to magnetic flux surfaces can destabilize a tearing mode, while a larger flow can have a stabilizing influence. It has also been shown that flow shear can affect the nonlinear dynamics of magnetic islands. I mention this work, because in EC and PPCD discharges, changes in the core flow profiles may occur that have a stabilizing influence on the tearing fluctuations. Detailed flow profile data is not yet available, but changes in core flow may play a significant role.

There were two questions asked earlier in this section that I will now attempt to answer. First, if the SDE's play a role in magnetic fluctuation reduction, then why do the m = 1 mode amplitudes *increase* briefly with each SDE? From Fig. 6 in Chapter 5 we know that when an SDE occurs, the density (and maybe the pressure) profile evolves from flat to peaked in the core. Since any pressure gradient $dP/dr < 0$ provides an additional drive for tearing instability [16,17], this may account for the momentary increase of the m = 1 amplitudes.

Second, if SDE's are responsible for the periods of reduced fluctuations, then how are periods lasting up to 5 ms sustained by an SDE lasting only a fraction of a millisecond? The most likely answer is that the SDE's are not acting alone. For example, since S (the Lundquist number) increases between SDE's, the scaling of magnetic fluctuations with S may provide for their reduction. Effects such as $\mathbf{E} \times \mathbf{B}$ flow shear in the edge and flow shear near the mode resonant surfaces in the core

could also be important. Further, since all extended periods of reduced fluctuations occur with PPCD and/or toroidal electric field reversal, it is quite possible that they also play a role, as expected theoretically.

6.2 Suppression of sawtooth crashes

EC periods were first characterized by the extended absence of sawtooth crashes [36]. Although it is now known that there is more to EC (and PPCD) discharges than a simple suppression of crashes, a brief discussion of sawteeth and some possible mechanisms for crash suppression is warranted.

Sawtooth oscillations [36,37,38] are comprised of a relatively slow rise phase and a more rapid crash phase. During the rise phase, the $\mu = \mu_o \mathbf{J}\cdot\mathbf{B}/B^2$ profile evolves to a peaked state as a result of resistive diffusion and the peaked parallel equilibrium inductive electric field. During this phase, gradients in $\mu(r)$ cause instability in the core-resonant m = 1 modes. At the crash, the m = 1 amplitudes increase dramatically, and through nonlinear coupling, they drive other modes unstable (e.g., those with m = 0). This destabilization results in a redistribution of parallel current and a flattening of $\mu(r)$. Note that each crash also causes a substantial increase in electrostatic fluctuations.

Although there has been a considerable amount of experimental and theoretical work devoted to sawteeth, it is my opinion that we do not yet fully understand this phenomenon. While the paradigm of current profile peaking and flattening is believable, there are some outstanding details of the process that need explanation. Of greatest relevance to this discussion is the triggering mechanism for the crash.

Identifying the trigger should help one understand crash suppression.

The simplest explanation for crash suppression was discussed in Ref. 36. Since the sawtooth cycle involves diffusion and peaking of the μ profile, the sawtooth cycle time must depend in part on the resistive diffusion time, $\tau_r \propto 1/\eta \propto Z_{eff}^{-1} T_e^{3/2}$. Since τ_r increases in EC (and PPCD) discharges, the sawtooth cycle time would be expected to increase as well. In Ref. 36, the rate at which $\mu(r)$ peaks during an EC period was compared to the sawtooth cycle time in a normal discharge, and it was demonstrated that the EC period could be considered simply as an extended sawtooth rise phase.

Although the resistive diffusion time is likely to play a significant role in the sawtooth cycle, the actual trigger for the crash is still not identified. The time at which the crash occurs is the time at which nonlinear energy transfer between the core-resonant m = 1 modes and the m = 0 modes begins. Thus, the mechanism that drives or allows this transfer may be fundamental to the triggering process.

It has been suggested that the onset of nonlinear coupling between the m = 1 and m = 0 modes will occur when the m = 1 modes grow to sufficient amplitude [39]. Thus, since gradients in $\mu(r)$ drive the m = 1 modes, one might guess that the crash occurs at some threshold $\nabla\mu$. However, as $\mu(r)$ evolves to a peaked state and feeds the m = 1 modes, the modes are able to shed some of this energy quasilinearly and nonlinearly, without the involvement of the m = 0 modes [39,40]. Thus, the crash depends on more than $\nabla\mu$. Further, there is at least one case in the MST in which the suggested dependence on the m = 1 amplitude is not apparent. I refer to the single-helicity state sometimes

observed in EC and PPCD discharges.

Nonlinear energy transfer between modes requires (1) that the mode's respective eigenfunctions overlap in space and (2) that the modes be phase locked (i.e., that there be a constant phase relationship between the modes) [15,18]. Overlap of the m = 1 and m = 0 eigenfunctions presumably occurs throughout each discharge, so there must normally be an absence of phase locking (between crashes). Measurements of the average impurity ion flow velocity in the core and the edge show that there is sometimes substantial shear between these two regions [41]. The local plasma flow velocity determines the local mode rotation to a large extent [42]. Therefore, with shear in the plasma flow velocity between the core and edge, there may be substantial shear between the phase velocities of the m = 1 and m = 0 modes, and this could inhibit phase locking and delay the onset of a sawtooth crash. In other words, phase locking may be the (or a) sawtooth crash trigger, and sawtooth crash suppression (delay) could be due in part to rotational shear between the m = 1 and m = 0 modes.

6.3 Summary

In this chapter, I discussed the role played by electrostatic and magnetic fluctuations in the RFP, and I discussed their reduction in EC and PPCD discharges. Electrostatic fluctuations govern particle transport in the plasma edge [9], while magnetic fluctuations govern particle [19] and energy [20] transport in the plasma core. Both EC and PPCD discharges exhibit a region of strong $\mathbf{E} \times \mathbf{B}$ flow shear in the edge. Electrostatic fluctuations are reduced within this region and over the

entire edge plasma. Global magnetic fluctuations are also reduced. Both the low and high frequency electrostatic fluctuations overlapping the region of strong flow shear may be directly affected by it, but other mechanisms, such as favorable changes in edge gradients, must be invoked to account for the reduction of high frequency fluctuations beyond the shear region.

There are many possible explanations for the reduction of the global magnetic fluctuations, and they fall into two general categories. In one category are explanations based on modification of the current profile. These include auxiliary current drive (PPCD and toroidal electric field reversal), the current driven by small dynamo events, and reduction of edge resistivity. It was shown that in EC discharges, magnetic fluctuation reduction can occur, albeit briefly, without auxiliary current drive. In tandem with the discussion of current profile effects was speculation that the flat core pressure profile (inferred from the density profile) might also play a role. The other category entails magnetic fluctuation reduction by flow shear. It is possible that these fluctuations are directly affected by the edge-localized $\mathbf{E} \times \mathbf{B}$ flow shear. It is also possible that as yet unmeasured changes in core rotation are affecting these fluctuations. If these fluctuations, and/or the electrostatic fluctuations, are affected by flow shear, this would represent a new paradigm for fluctuation reduction in the RFP.

References

[1] B. E. Chapman *et al.*, submitted to Phys. Rev. Lett.

[2] J. S. Sarff *et al.*, Phys. Rev. Lett. **72**, 3670 (1994).

[3] J. S. Sarff *et al.*, Phys. Rev. Lett. **78**, 62 (1997).

[4] H. P. Furth, J. Killeen, and M. N. Rosenbluth, Phys. Fluids **6**, 459 (1963).

[5] S. C. Prager, Plasma Phys. Controlled Fusion **32**, 903 (1990).

[6] P. W. Terry *et al.*, in Proceedings of the 13th International Conference on Plasma Physics and Controlled Nuclear Fusion Research, Washington D. C., 1990 (IAEA, Vienna, 1991), Vol. 2, p. 169.

[7] G. Li *et al.*, Phys. Plasmas **2**, 2615 (1995).

[8] N. Mattor and P. H. Diamond, Phys. Rev. Lett. **72**, 486 (1994).

[9] T. D. Rempel *et al.*, Phys. Rev. Lett. **67**, 1438 (1991).

[10] R. J. Groebner, Phys. Fl. B **5**, 2343 (1993).

[11] E. Holzhauer *et al.*, Plasms Phys. Controlled Fusion **36**, A3 (1994).

[12] G. R. Tynan *et al.*, Plasms Phys. Controlled Fusion **36**, A285 (1994).

[13] H. Biglari, P. H. Diamond, and P. W. Terry, Phys. Fl. B **2**, 1 (1990).

[14] D. Craig (private communication).

[15] S. Assadi, S. C. Prager, and K. L. Sidikman, Phys. Rev. Lett. **69**, 281 (1992).

[16] B. Coppi, J. M. Greene, and J. L Johnson, Nucl. Fusion **6**, 101 (1966).

[17] C. R. Sovinec, Ph.D. thesis, University of Wisconsin, Madison, Wisconsin, 1995.

[18] J. S. Sarff *et al.*, Phys. Fl. B **5**, 2540 (1993).

[19] M. R. Stoneking *et al.*, Phys. Rev. Lett. **73**, 549 (1994).

[20] G. Fiksel *et al.*, Phys. Rev. Lett. **72**, 1028 (1994).

[21] A. B. Rechester and M. N. Rosenbluth, Phys. Rev. Lett. **40**, 38 (1978).

[22] S. Ortolani and D. D. Schnack, Magnetohydrodynamics of Plasma Relaxation (World Scientific, Singapore, 1994).

[23] C. L. Rettig *et al.*, Phys. Fl. B **5**, 2428 (1993).

[24] R. J. La Haye *et al.*, Phys. Plasmas **1**, 373 (1994).

[25] Y. L. Ho, Nucl. Fusion **31**, 314 (1991).

[26] R. J. LaHaye *et al.*, Phys. Fluids **27**, 2576 (1984).

[27] D. Brotherton-Ratcliffe, C. G. Gimblett, and I. H. Hutchinson, Plasma Phys. Controlled Fusion **29**, 161 (1987).

[28] Z. G. An *et al.*, in Proceedings of the 11th International Conference on Plasma Physics and Controlled Nuclear Fusion Research, Kyoto, 1986 (IAEA, Vienna, 1987), Vol. 2, p. 663.

[29] P. Nordlund *et al.*, in Proceedings of the 15th International Conference on Plasma Physics and Controlled Nuclear Fusion Research, Seville, 1994 (IAEA, Vienna, 1995), Vol. 2, p. 353.

[30] H. E. Sätherblom, S. Mazur, and P. Nordlund, Plasma Phys. Controlled Fusion **38**, 2205 (1996).

[31] P. Nordlund and S. Mazur, Phys. Plasmas **1**, 3936 (1994).

[32] J. T Chapman (private communication).

[33] N. Mattor, Phys. Plasmas **3**, 1578 (1996).

[34] P. H. Rutherford, Phys. of Fluids **16**, 1903 (1973).

[35] M. Persson, Nucl. Fusion **31**, 382 (1991).

[36] B. E. Chapman *et al.*, Phys. Plasmas **3**, 709 (1996).

[37] J. A. Beckstead, Ph.D. thesis, University of Wisconsin, Madison, Wisconsin, 1990.

[38] S. Hokin *et al.*, Phys. Fl. B **3**, 2241 (1991).

[39] Y. L. Ho and G. G. Craddock, Phys. Fl B **3**, 721 (1991).

[40] J. A. Holmes *et al.*, Phys. Fluids **31**, 1166 (1988).

[41] A. F. Almagri *et al.*, PLP Report No. 1194, University of Wisconsin, Madison, Wisconsin, 1996.

[42] D. J. Den Hartog *et al.*, Phys. Plasmas **2**, 2281 (1995).

7. Summary and concluding discussion

By satisfying operational requirements for toroidal magnetic field reversal, electron density, wall conditioning, field error control, and fueling, enhanced confinement discharges are achievable with energy confinement times of about 3 ms [1] and 5 ms [2], respectively. These discharges share several features in common, including (1) a region of strong $\mathbf{E} \times \mathbf{B}$ flow shear in the edge, (2) reduction of electrostatic fluctuations within and beyond the shear region, (3) reduction of global magnetic fluctuations, and (4) changes to the current profile due, e.g., to a new type of discrete dynamo and reduction of plasma resistivity.

The electrostatic fluctuations that overlap the $\mathbf{E} \times \mathbf{B}$ flow shear region can be directly affected by it. However, for those fluctuations beyond the shear region that do not overlap it, other mechanisms, such as stabilizing changes in edge gradients, must be invoked. Reduction of the global magnetic fluctuations in the presence of auxiliary poloidal and/or toroidal current drive is expected, but other explanations are required for those discharges lacking auxiliary current. The small dynamo events, by momentarily reducing $\nabla\mu$, can play a role, as may the reduced plasma resistivity, the apparently flat core pressure profile, and favorable changes, if any, in the core plasma rotation profile. These global fluctuations may also be directly affected by the strong $\mathbf{E} \times \mathbf{B}$ flow shear. The ability of auxiliary edge current drive to suppress small dynamo events is also important, since extended periods of reduced magnetic fluctuations only occur in the absence of small dynamo events.

The MST may not be the only RFP to have witnessed EC-like

discharges. Hirano *et al.* [3] describe periods of enhanced confinement called "Improved High Theta Mode" (IHTM) achieved in the TPE-1RM20 RFP. In this case, high theta [$\equiv B_\theta(a)/\langle B_\phi \rangle$] is achieved with strong toroidal field reversal, since this reduces $\langle B_\phi \rangle$. IHTM occurs following intensive wall conditioning in 150 kA discharges with $F \equiv B_\phi(a)/\langle B_\phi \rangle = -0.5$, similar to the EC reversal requirement at this plasma current. As with EC periods in the MST, IHTM occurs sporadically and appears (from the data presented) to follow sawtooth crashes. During IHTM, normal sawtooth crashes are suppressed but are replaced by "mild crashes." No discussion of these mild crashes is included, but perhaps they are like the small dynamo events in the MST? The enhanced confinement of IHTM is attributed to a reduction of the dominant magnetic fluctuations, but no measurements of edge electrostatic fluctuations or the radial electric field profile were made, and, unfortunately, TPE-1RM20 was decommissioned in the Fall of 1996.

In the MST, there is much work to be done to better understand and characterize EC and PPCD discharges. First, measurement of the radial electric field profile using different diagnostics would be useful. While the swept Langmuir probe technique is fairly reliable, diagnostics that are not affected by the fast electrons are needed. An emissive Langmuir probe [4] is such a diagnostic, but it is uncertain if such a probe would survive long enough to be useful. One relevant noninvasive diagnostic is the heavy ion beam probe, and one may be installed on the MST in the near future. In lieu of direct measurements of the plasma potential, however, the radial electric field profile can be reconstructed using the radial force balance equation (see Chapters 2

and 4). This requires local measurements of the fuel or impurity ion pressure gradient and the toroidal and poloidal flow velocities, and if these measurements are made with noninvasive diagnostics (e.g., a neutral beam), then the radial electric field profile can be measured at higher plasma current than is now possible.

In Chapter 3, I discussed the inability of the various RFP equilibrium models to accurately calculate the Ohmic input power during small dynamo events. The problem lies in the calculation of the time evolution of the stored magnetic energy. Two diagnostics may help to resolve this problem. First, probe-mounted magnetic sensing coils can be inserted into EC and PPCD discharges to measure the time evolution of $\mathbf{B}(r)$ in the plasma edge. Further, a polarimeter is being implemented which will give some information on $\mathbf{B}(r)$ in the core. If the time evolution of $\mathbf{B}(r)$ over the plasma cross section can be reconstructed with these diagnostics, changes in magnetic stored energy can be calculated directly, or at least the measurements can be applied to modify the model calculations. This should improve the accuracy of the Ohmic input power and more importantly, the resultant energy confinement time.

To determine whether or not the region of strong $\mathbf{E} \times \mathbf{B}$ flow shear is acting as a barrier to transport, detailed profiles of the electron temperature and density are needed. Given our experience with probes in these discharges, accurate measurement of the temperature and density demands noninvasive diagnostics. In the near term, however, probe measurements of fluctuation induced transport in the shear region will have to suffice. These measurements will also help to

determine if the reduction of electrostatic fluctuations beyond the shear region contributes to the improved confinement.

Another significant outstanding issue is whether the relatively simple application of auxiliary heating can trigger EC/PPCD-like discharges. A related issue is whether heating can reduce the frequency of the small dynamo events, perhaps to the point of complete suppression. In order to carefully test the heating hypothesis, no net plasma current should be driven by the heating technique. I have hypothesized, for example, that the Ohmic heating capability of PPCD may be just as or even more important than its capability for current drive, but one is presently unable to separate the two effects of PPCD.

Application of a sinusoidal voltage to the toroidal and/or poloidal gaps is one possible heating technique. In the same manner as PPCD, this will inductively drive current in the edge plasma. However, at a sufficiently large frequency, it will be essentially a skin current. For heating beyond the extreme edge in this case, one must rely on inward heat transport. More advanced techniques include electron cyclotron or lower hybrid heating. These techniques could allow heating of the core and the edge. Except for PPCD, auxiliary heating has never been attempted in an RFP, so its implementation alone would be of interest.

What impact do EC and PPCD discharges have on the RFP as a fusion reactor concept? Prager [5] discusses three of the major RFP issues that must be confronted in the quest for reactor viability: (1) scaling of energy confinement with plasma current, (2) the need for steady state toroidal current drive, and (3) the present need for a conducting shell. Some of the discussion that follows is based on Ref. 5

and references therein.

The reactor promise of the RFP depends largely on how its energy confinement scales with plasma current. Most RFP's to date have operated at a poloidal beta (ratio of the volume-averaged plasma pressure to the edge poloidal magnetic field pressure) of about 10%. Further, the plasma resistance in these devices has scaled classically. Given these results, one can derive a scaling relation for the RFP energy confinement time: $\tau_E \sim a^2 I^3/N^{3/2}$, where a is the device minor radius, I is the toroidal plasma current, and N is the line density. For the RFP to remain a viable reactor concept, present and future RFP's must satisfy this (or even more favorable) scaling.

PPCD discharges [2] with $\tau_E \sim 5$ ms actually exceed the scaling prediction by a small margin, but the energy confinement time of EC discharges, which has only been measured at large plasma current, falls somewhat short. Note that neither the PPCD nor the EC energy confinement time has been measured during the low current discharges with long SDE-free periods (illustrated in Chapters 5 and 6), but initial estimates suggest that in both cases, the scaling prediction may be surpassed.

For a reactor operated in steady state, the usual inductive technique for toroidal current drive is insufficient. A potentially simple means of steady state current drive was proposed and tested on the ZT-40M RFP, namely, driving properly phased oscillating voltages across the poloidal and toroidal gaps. Tests of this technique (called F-θ pumping) were largely unsuccessful, and it was believed that the primary culprit was a large plasma resistivity. In the MST, however,

one could initiate F–θ pumping after triggering an EC/PPCD–like discharge. With the reduced resistivity characteristic of these discharges, F–θ pumping might have a chance for success.

It is well known experimentally and theoretically that, without a conducting boundary, the dominant magnetic fluctuations grow to large amplitude. This boundary condition poses serious technical challenges for a steady state or long pulse RFP reactor. In a long discharge, even a shell that is normally conducting will eventually "appear" to be resistive to the plasma due to the penetration of the shell by internal magnetic field lines. However, it is conceivable that the mechanism(s) responsible for reduction of magnetic fluctuations in EC and PPCD discharges may provide the means to tame these instabilities without the need for a conducting shell.

Strong $\mathbf{E} \times \mathbf{B}$ flow shear accompanies two types of enhanced confinement discharge in the MST. There is a finite probability that the $\mathbf{E} \times \mathbf{B}$ flow shear can be triggered by auxiliary heating. If this is the case, and if the flow shear plays a role in the improved confinement, then the prospects for the RFP as a fusion reactor will have improved substantially.

References

[1] B. E. Chapman *et al.*, submitted to Phys. Rev. Lett.

[2] J. S. Sarff *et al.*, Phys. Rev. Lett. **78**, 62 (1997).

[3] Y. Hirano *et al.*, Nucl Fusion **36**, 721 (1996).

[4] N. Hershkowitz, in Plasma Diagnostics: Discharge Parameters and Chemistry, Vol. 1, edited by O. Anciello and D. L. Flamm (Academic, New York, 1991).

[5] S. C. Prager, Plasma Phys. Controlled Fusion **32**, 903 (1990).

EXTERNAL DISTRIBUTION IN ADDITION TO UC-20

S.N. Rasband, Brigham Young University
R.A. Moyer, General Atomics
J.B. Taylor, Institute for Fusion Studies, The University of Texas at Austin
E. Uchimoto, University of Montana
F.W. Perkins, PPPL
O. Ishihara, Texas Technical University
M.A. Abdou, University of California, Los Angeles
R.W. Conn, University of California, Los Angeles
P.E. Vandenplas, Association Euratom-Etat Belge, Belgium
Centro Brasileiro de Pesquisas Firicas, Brazil
P. Sakanaka, Institute de Fisica-Unicamp, Brazil
Mme. Monique Bex, GANIL, France
J. Radet, CEN/CADARACHE, France
University of Ioannina, Greece
R. Andreani, Associazione EURATOM-ENEA sulla Fusione, Italy
Biblioteca, Istituto Gas Ionizzati, EURATON-ENEA-CNR Association, Italy
Plasma section, Energy Fundamentals Division Electrotechnical Laboratory, Japan
Y. Kondoh, Gunma University, Kiryu, Gunma, Japan
H. Toyama, University of Tokyo, Japan
Z. Yoshida. University of Tokyo, Japan
FOM-Instituut voor Plasmafysica "Rijnhuizen," The Netherlands
Z. Ning, Academia Sinica, Peoples Republic of China
P. Yang, Shandong University, Peoples Republic of China
S. Zhu, University of Science & Technology of China, People's Republic of China
I.N. Bogatu, Institute of Atomic Physics, Romania
M.J. Alport, University of Natal, Durban, South Africa
R. Storer, The Flinders University of South Australia, South Australia
B. Lehnert, Royal Institute of Technology, Sweden
Librarian, CRPP, Ecole Polytechnique Federale de Lausanne, Switzerland
B. Alper, Culham Laboratory, UK
A. Newton, UK

2 for Chicago Operations Office
5 for individuals in Washington Offices

INTERNAL DISTRIBUTION IN ADDITION TO UC-20
80 for local group and file